



저작자표시-비영리-변경금지 2.0 대한민국

이용자는 아래의 조건을 따르는 경우에 한하여 자유롭게

- 이 저작물을 복제, 배포, 전송, 전시, 공연 및 방송할 수 있습니다.

다음과 같은 조건을 따라야 합니다:



저작자표시. 귀하는 원저작자를 표시하여야 합니다.



비영리. 귀하는 이 저작물을 영리 목적으로 이용할 수 없습니다.



변경금지. 귀하는 이 저작물을 개작, 변형 또는 가공할 수 없습니다.

- 귀하는, 이 저작물의 재이용이나 배포의 경우, 이 저작물에 적용된 이용허락조건을 명확하게 나타내어야 합니다.
- 저작권자로부터 별도의 허가를 받으면 이러한 조건들은 적용되지 않습니다.

저작권법에 따른 이용자의 권리는 위의 내용에 의하여 영향을 받지 않습니다.

이것은 [이용허락규약\(Legal Code\)](#)을 이해하기 쉽게 요약한 것입니다.

[Disclaimer](#)

공학박사 학위논문

**Mechanical Design of Heterogeneous
Thin-films for Flexible Electronic Devices**

이종 박막의 기계적 설계를 통한
유연 전자 소자 제작 연구

2019 년 2 월

서울대학교 대학원

기계항공공학부

이 건 희

이종 박막의 기계적 설계를 통한 유연 전자 소자 제작 연구

Mechanical Design of Heterogeneous Thin-films
for Flexible Electronic Devices

지도교수 최 만 수

이 논문을 공학박사 학위논문으로 제출함

2018년 10월


서울대학교 대학원


기계항공공학부


이 건 희


이건희의 공학박사 학위논문을 인준함


2018년 12월

위원장 : 이윤서 (인) 

부위원장 : 최만수 (인) 

위원 : 남기태 (인) 

위원 : 정현석 (인) 

위원 : 김상문 (인) 

Mechanical Design of Heterogeneous Thin-films for Flexible Electronic Devices

Gunhee Lee

School of Mechanical and Aerospace Engineering

The Graduate School

Seoul National University

Abstract

Flexible electronic devices have been actively studied because of their broad range of potential uses, over the past several years. Since flexible electronic devices have been required to maintain their functions even under the conditions where mechanical deformation easily occurs, researches have been concentrated on improving mechanical durability against deformation. However, it is possible to develop flexible electronic devices that implement new functions if the deformation characteristics are appropriately utilized. This dissertation aims to develop a flexible electronic device that implements new functions along with the development of the device with high durability by using the phenomenon that the response characteristics of the flexible devices are varied in accordance with the mechanical design of heterogeneous thin-films.

First, the sensor and the switch device have been fabricated by using the generated cracks when deforming two different bonded layers with large

difference in elastic modulus. The sensor and the switch device using cracks mainly consists of conductive metal thin film and an elastic polymer substrate, and operates by measuring the minute crack change depending on the tensile force as an electric resistance signal. In the crack based sensor system, the shape and depth of the cracks generated depending on the materials of the layers constituting the device change, and the sensitivity and characteristics thereof are also changed. Therefore, the depth, width and response characteristics of the cracks formed by the strain could be modified through the introduction of a silicone rubber substrate which has lower elastic modulus than that of a PUA. The device with silicone rubber formed deeper cracks than the devices using PUA, which enabled the device to operate as a switch. The crack width of the switch system exhibits a super-exponential dependence on the applied strain, instead of a linear dependence of regular widening because the depth of the crack also deepens together with the degree of applied strain. Such super-exponential behavior of widening of the crack leads to an almost infinite resistance ($> 10^{12} \Omega$) of the metal film when the applied strain approaches 2%. The resistance of the switch increases approximately by 5 orders of magnitude when 1.6% strain is applied, resulting in an overall gauge factor that exceeds 6×10^6 , which shows that our device can perform as a switch. By combination of metal-elastomer bilayer strain-gated switches, we demonstrated logic elements such as AND, OR, NAND, and NOR gates by expressing the gestures of fingers as numbers on a seven-segment display.

Secondly, a rollable platform and electronic devices have been fabricated using the residual stress which was formed through the bonding of two layers

having different degree of elongation. The rollable platform can roll and unroll to a great extent on demand, inspired by the rolling mechanism of the proboscis of a butterfly. Unlike traditional implantable devices, our system can integrate various electronic devices into a small volume, allowing passage through a narrow area, and making contact with thin, round and curved surfaces such as blood vessels completely in contact with each other. Based on structural analysis, we have made thin film electronics including a heater, strain sensor, temperature sensor and OLED on the rollable platform and confirmed that all the electronics operate normally in the rolled and unrolled states without a breakdown. Furthermore, we have successfully demonstrated a cell sheet transfer to a damaged hind limb muscle of a mouse with the rollable platform, and measure pulse wave of swine by winding the superficial femoral artery of swine with the rollable platform.

Thirdly, the mechanical durability of a perovskite films has been investigated by varying the substrate thickness in cyclic bending tests. Perovskite materials have a great potential to be flexible solar cells due to their mechanical flexibility and high performance. Nevertheless, it is still required to be developed further in terms of flexibility and efficiency to prove their practical viability. In this work, we have successfully demonstrated ultra-flexible solar cells with high efficiency (17.03%) along with the unprecedented flexibility sustained after 10,000 cycles of bending at 0.5 mm radius or through harsh conditions such as rolling and crumpling. We achieved such a superior performance by fabricating crack-free perovskite film on the ultra-thin substrate ($\sim 2.5 \mu\text{m}$). We confirmed that the substrate thickness is the most effective factors of mechanical durability of whole

device through the morphological observation after cyclic bending test by varying the substrate thickness. We suggest the fracture point of the perovskite thin films by evaluating the relationship between crack formation and applied strains. Furthermore, we have accomplished the best efficiency of 13.6% for a large-area flexible perovskite solar cells (1.2 cm²) by applying the hybrid transparent electrode composed of metal mesh grid and conducting polymer.

Keywords: deformation, heterogeneous thin-film design, crack system, rollable platform, flexible electronics, flexible perovskite solar cell

Student Number: 2013-22494

Contents

Abstract	i
Contents	v
List of Tables	viii
Nomenclature	ix
List of Figures	x
Chapter 1. Introduction	1
1.1. Research Background and Objectives	1
1.2. Thesis outline	6
1.3. References	7
Chapter 2. Strain Gated Switch by Utilizing a Crack Based System	14
2.1. Introduction	14
2.2. Experimental Methods	17
2.2.1. Fabrication of strain gated switch	17
2.2.2. Characterization	18
2.3. Results and Discussion	19
2.3.1. Structure of crack based strain gated switch	19
2.3.2. Performance of crack based strain gated switch	21
2.3.3. Theoretical modeling of crack based strain gated switch .	26
2.3.4. Applications of crack based strain gated switch	30
2.4. Conclusion	38

2.5. References.....	39
Chapter 3. Rollable Platform for Integrated System with Gripper and Flexible Electronics	43
3.1. Introduction.....	43
3.2. Experimental Methods.....	46
3.2.1. Fabrication of rollable platforms and electronics	46
3.2.2. FEM and physical analysis	50
3.2.3. Swine preparation and pulse wave detecting procedure using rollable platform.....	51
3.2.4. Fabrication of cell sheet implanted platform and Cell sheet transfer procedure.....	52
3.3. Results and Discussion	55
3.3.1. Device structure and characteristics of rollable platform .	55
3.3.2. Rollability analysis of rollable platform	58
3.3.3. Operation of various electronics on rollable platform	62
3.3.4. Theoretical modeling of material fracture	66
3.3.5. Actuating and detecting with rollable platform	69
3.3.6. Cell sheet transfer using rollable platform.....	75
3.4. Conclusion	78
3.5. References.....	79
Chapter 4. Ultra-Flexible Perovskite Solar Cells by Studying the Mechanical Fracture Behavior	85
4.1. Introduction.....	85
4.2. Experimental Methods.....	88
4.2.1. Fabrication of flexible perovskite solar cells	88

4.2.2.	FEM simulation method	89
4.2.3.	Characterization	90
4.3.	Results and Discussion	91
4.3.1.	Device structure and uniformity issue of perovskite film coating.....	91
4.3.2.	Analysis on mechanical fracture behavior	94
4.3.3.	Device characteristics	100
4.3.4.	Large area device characteristics	106
4.4.	Conclusion	111
4.5.	References	112
Acknowledgement.....		117
Abstract (in Korean).....		118
List of Publications		123

List of Tables

Table 3.1 Material properties and film thickness of rollable platform	68
Table 4.1 Photovoltaic parameters of flexible perovskite solar cells corresponding to the active area.....	105
Table 4.2 Sheet resistances of PEDOT:PSS/PET and PEDOT:PSS/gold mesh/PET substrate	109

Nomenclature

I	Electrical current	[A]
ε	Strain	[a.u]
ΔR	Resistance change	[Ω]
R_0	Initial resistance	[Ω]
W	Crack width	[μm]
$D(\varepsilon)$	Crack depth	[μm]
D_0	Maximum depth of crack	[μm]
d	Broadness of the slab	[mm]
L	Characteristic length	[mm]
d_1, d_2	Thin film thickness	[μm]
σ	Stress	[N/m ²]
E	Elastic modulus	[MPa]
ν	Poisson's ratio	[a.u]
J_{SC}	Short-circuit current density	[mA cm ⁻²]
V_{OC}	Open-circuit voltage	[V]
FF	Fill factor	[%]
PCE	Power conversion efficiency	[%]
EQE	External quantum efficiency	[%]
R	Bending radius	[mm]

List of Figures

Figure 2.1 Comparison of on/off ratio with variation of strains between our work and the previous studies.....	16
Figure 2.2 Fabrication process for the strain gated switch. (a) Deposition of platinum (Pt) onto the silicone rubber substrate. (b) Pt crack generation by stretching out the metal deposited silicone rubber substrate.....	18
Figure 2.3 (a) Schematic illustration of operating strain-gated switches. (b, c) Photos for operating strain-gated switches and the corresponding SEM images of opened and closed cracks. (d) Schematic illustration of the super-exponential behavior of crack widening with variation of strain. (e) Comparison of normalized resistance variance between the crack sensor and the crack switch when strain is applied to the devices.	20
Figure 2.4 (a) The variation of depth and width with the variation of applied strain. (b) The graph of normalized resistance variance versus a strain of 1.6% in 15 cyclic tests. (Inset: 2.0% in 5 cyclic tests). (c) The standard deviation and the average over 5 different samples in the hysteresis test of the strain gated switch. Red and black dots show unloading and loading states, respectively. (d) The response time of the strain gated switch. The red and black lines indicate the input signal (strain of 0.4%), and the response time of the input strain, respectively.....	23
Figure 2.5 Optical microscope camera images of the Pt layer. The orange arrows indicate the tensile direction.....	24

Figure 2.6 Strain-dependent gauge factor by taking the derivative of R/R_0 with respect to strains from 0 % to 1.6 %24

Figure 2.7 A marathon test of the strain gated switch by repeating about 5,000 cycles of loading/unloading process at strain from 0 % to 1.6 %. (a) A final normalized resistance of the marathon test at a certain period (about 500 cycles). (b) Loading/unloading test after 5,000 cyclic tests. The depth profile of crack measured by AFM at 1.6 % strain. After 1 cycle (c) and 5000 cycles (d) of loading/unloading process at strain from 0 % to 1.6 %25

Figure 2.8 (a) Definition of parameters in the strain gated switch. (b) The variation of depth with the variation of applied strain, (c) The width of crack lip opening with respect to applied strain. Black dots were measured by AFM, red dots were plotted based on our theoretical modeling, and blue dots were plotted based on theoretical modeling by using measured resistance variation. (d) The plot of $\varepsilon/(W(\varepsilon))$ with respect to the crack depth (e) The $100 \ln(R/R_0)$ with respect to the crack width.29

Figure 2.9 Four logic gates with strain gated switches. (a, c, e and g) Schematic illustrations of AND (a), OR (c), NAND (e), and NOR (g) logic gates. Depending on the motion of the joint, the combination of the switch states led to logical output of either “1” or “0”. (b, d, f and h) Demonstrations of LED “on/off” with respect to the corresponding logical output. The measured electrical output resistances of AND, OR, NAND, and NOR gates versus the mechanical input strains by the motion of the joint.31

Figure 2.10 Operating principle of a motion induced logic gate. (a,b) open collector crack switch circuits, (c,d) totem pole crack switch circuit..32

Figure 2.11 (a) Schematic illustration of fabrication of a curved switch. (b) Shift of the threshold strain of the curved switch due to the predefined shape. (c) Resistance variance of the combination of the curved switch (upper side) and flat switch (lower side). Three output levels were created by mounting two switches with varied motions of the joints on fingers. (d and e) Photographs of output logic signals, “7” (d) and “2” (e), that appeared on the seven segment display in accordance with varied motions of the five fingers.35

Figure 2.12 (a) Composition of seven-segment connected with the strain gated switches, (b) Logical table showing the relation of the expressing number and the motion of fingers, (c) Demonstration of expressing numbers from “0” to “9” with the varied motion of fingers.....36

Figure 2.13. A graph of resistance with varied strains, which shows the controllable threshold strain with variation of applied pre-strain of lower substrate from 0% to 15 %.....37

Figure 3.1 Illustration images of the fabrication process of rollable platform.....48

Figure 3.2 Illustration images of fabrication process of organic light emitted diode (OLED), heater, strain and temperature sensor..49

Figure 3.3 (a) A schematic illustration of how a butterfly gets fed from a flower. It unrolls its proboscis, which is normally kept coiled, in order to go through the flower. (b) The composition of the rollable electronic device. On the silicone rubber, the PDMS layers and PI films are

stacked alternately as shown (up). When air is injected into the space between the polyimide films, the device is swollen and unrolled. (c) The composition of the electronic devices on the top PI film. They are constructed in the order of: heater, strain sensor, OLED and electrode from left to right. Photos of rolled state from the top (left inset) and side views (right inset).....57

Figure 3.4 (a) An illustration of the rollable device that shows the extent of its rollability, which is determined by the inner diameter. (b) Photographic images of the devices in the side view with variations of applied strains (30%, 40% and 50%) and thickness (40 μ m, 70 μ m and 100 μ m) of the silicone rubber. (c) The measurements of the inner diameter of the rollable device with variations of applied strains and thickness of the silicone rubber. (d) Captured images of FEM simulation of the rolling process with time dependent at 30 % applied strain and 70 μ m thickness silicone rubber. (e) FEM results of the applied stresses on the 70 μ m silicone rubber at variation of applied strains..60

Figure 3.5 FEM results of the residual stresses of the silicone rubber with variations of applied strains (30%, 40% and 50%) and thickness (40 μ m, 70 μ m and 100 μ m) of silicone rubber.61

Figure 3.6 (a) Photographic images and thermal images of the heater in its unrolled and rolled states. Thermal images of the heater show the temperature distribution when currents are applied. (b) Photographic images of the OLED in its unrolled and rolled states with currents applied. (c) Photographic images of the temperature and strain sensor

in its unrolled and rolled states.....	64
Figure 3.7 (a, b) Measurements of resistance change of the temperature sensor with variation of temperature in its rolled and unrolled states. (c) The graph of normalized resistance variance versus strain of 2%. (d) Measurements of resistance change of the strain sensor in its rolled and unrolled states.....	65
Figure 3.8 Illustrations of simplified model for analyzing rollable system.	68
Figure 3.9 (a) Measurements of resistance change of the strain sensor with and without an ant (b) Measurements of resistance change of the strain sensor with variation of the diameter of 6.1 mm to 5.7 mm... ..	72
Figure 3.10 (a) Schematic Illustration of two types of systems for the pulse wave detecting. (b) Photographic images of the implanted sensors on swine's blood vessels and monitoring systems. (c) Schematic Illustration images and (d) photographic images of the rollable device, which wraps and unwraps around a blood vessel.....	73
Figure 3.11 Pulse waves of swine's blood vessels using conventional IBP sensor and our device in its (a) unrolled and (b) rolled states at normal condition. Pulse waves of swine's blood vessels at abnormal condition (c) after epinephrine injection and (d) after KCl injection.....	74
Figure 3.12 The movements of the rollable device through the narrow, curved acrylic tube.....	76
Figure 3.13 (a) Illustration images of the rollable platform with the cell sheet attached, in its unrolled and rolled states. (b) The cross section fluorescence microscope images of stained cell sheet by 4',6-diamidino-2-phenylindole (DAPI), F-actin and merged on the rolled platform. (c)	

The confocal microscope images of live & dead assay for stained cell sheet on the rollable platform before rolling and after 5 times of rolling. (d) Illustration images of cell sheet transplantation method operated to a mouse. The rollable platform with a cell sheet is inserted into the mouse with minimal damage and spread out after insertion. (e) Fluorescence microscope image of sectioned hind limbs muscle with transplanted cell sheet (left) and its optical microscope image stained by haematoxylin and eosin (H&E) (right).....77

Figure 4.1 (a) Graphical illustration of the difference of the perovskite film quality depending on the existence of PDMS. (b) Schematic illustration and cross-sectional SEM images of device structure of the flexible perovskite solar cell. (c) Box chart of PCEs of three devices with different substrate thicknesses (2.5 μm , 30 μm , and 100 μm).....93

Figure 4.2 (a) $J-V$ curves of the perovskite solar cells before and after cyclic bending tests ($R = 0.5$ mm, 1,000 cycles) with different substrate thicknesses. (b) Schematic illustrations of the substrate thickness in the perovskite film upon sustainable bending.....96

Figure 4.3 Normalized PCEs as a function of bending cycles for the substrates with the thickness of (a) 2.5 μm , (d) 30 μm and (g) 100 μm at 0.5 mm and 1 mm bending radii. SEM Images of the perovskite film after bending cyclic tests for the substrates with the thickness of (b, c) 2.5 μm , (e, f) 30 μm and (h,i) 100 μm at 0.5 mm and 1mm bending radii..97

Figure 4.4 SEM Images of PEDOT:PSS surface after cyclic bending test for 30 μm substrate thickness at different bending radius ($R = 1$ and 0.5

mm).	98
Figure 4.5 Relationship of crack formation and applied strain on perovskite film based on FEM results and SEM images..	98
Figure 4.6 FEM simulation results of applied stress on perovskite film with different substrate thickness at fixed bending radius of (a) 0.5mm and (b) 1 mm.....	99
Figure 4.7 (a) Reverse and forward bias J-V curves of the perovskite solar cell used a 2.5 μm thick substrate. (b) Normalized PCEs as a function of bending cycles depending on bending radius ($R = 2, 1, \text{ and } 0.5 \text{ mm}$) at the 2.5 μm thick substrate. The inset photograph shows the device bent at various bending radii. The J-V curves of the devices before and after (c) rolling and (d) crumpling tests. The inset photograph shows the rolling and crumpling process.....	102
Figure 4.8 Histograms of PCE of 45 devices using 2.5 μm substrate.	103
Figure 4.9 (a) Steady-state photocurrent density (black) and power conversion efficiency (blue) measured at the maximum power voltage of 0.81 V for 200 sec. (b) EQE spectra (blue) and the integrated JSC (red) of perovskite solar cell.....	103
Figure 4.10 Normalized PCEs of perovskite devices as a function of (a) rolling and (b) crumpling cycles at 2.5 μm thickness substrate.	104
Figure 4.11 (a) Schematic illustration of the structure of large area flexible perovskite solar cell using a gold mesh grid. (b) The transmittance of ITO/glass, PEDOT:PSS/PET and PEDOT:PSS/PET substrates. (c) J-V curves of the large area device (1.2 cm^2) with and without the gold mesh grid. (d) Normalized PCEs of large area devices as a function of bending	

cycles depending on bending radius ($R = 1$, and 0.5 mm) at the 2.5 μm thick substrate. (e) SEM images of hybrid electrode (gold mesh and PEDOT:PSS) and perovskite film after bending tests.....	108
Figure 4.12 Histograms of PCE of 20 devices of large area (1.2 cm^2) flexible perovskite solar cells.....	109
Figure 4.13 Normalized PCEs of large area perovskite devices as a function of (a) rolling and (b) crumpling cycles at 2.5 μm thickness substrate.....	110

Chapter 1. Introduction

1.1. Research Background and Objectives

Flexible electronic devices have a wide range of potential uses, from devices for energy generation [1,2], storage [3,4], displays [5-7] and bio-robotics [8,9] to biomedical devices [10-12] that make conformal contact with a skin and organs. Due to its versatile use, flexible electronic devices have been actively studied and developed for past several years. Unlike conventional rigid electronic devices, flexible electronic devices are generally used for the purpose of attaching to the skin and internal organs of a soft and curved surface, maximizing space utilization, and portability of the device. [13,14] So, flexible electronic devices require durability that is not comprised by mechanical deformation. [15-17] To fabricate unbreakable devices which have flexibility and stretchability, a lot of research has been conducted through various engineering approaches such as introduction of intrinsic flexible material, [18,19] and structure design of devices. [20]

One of the intrinsic flexible materials using for flexible electronics is based on organic conductors and semiconductors. [21,22] Moreover, organics can be more flexible with the production of fibers to form elastic mats and the synthesis of materials whose solid-state packing structure or molecular structure. [23] However, the conductivity and transport properties of organic materials are inferior to those of inorganics. Furthermore,

generally, flexible electronic devices are composed of multi-layer structures using not only organic materials but also inorganic materials for conducting complex functions. In order to maintain flexibility despite introduction of inorganic materials, flexible devices composed of multi-layers can be rendered flexibility in many of the ways such as using relief features [24,25], kirigami [26], serpentine [27-29], or wavy [30,31] that direct strain away from the sensitive components. In the flexible electrical device with multi-layer structure, material selection and structural design studies have been carried out mainly in the direction of durability against deformation. However, deviating from the study of simply increasing the durability against deformation, if the response characteristic of the deformation due to the multi-layered design is appropriately utilized, various system development of new functions is possible.

This dissertation aims to develop flexible electronic devices that realizes new functions and excellent durability by utilizing the response characteristics of flexible devices are varied depending on the deformation according to the hetero structure layer design.

First, cracks that occur when a strain is applied to a hetero structure layer having a large difference in elastic modulus can be used. Generally, research has been focused on suppressing the generation of cracks so far, as cracks could cause device failure. However, several studies have been reported that look at cracks in a new perspective. Prof. Ko reported a method that could create cracks with various patterns including straight lines and curves, and the controlled initiation, propagation and termination of various channeled crack patterns. [32] Such a patterning technique of cracks is meaningful in

that it can be applied to ultra-small-sized semiconductor chips and micro-bio-chips capable of accurate diagnosis in the future. After that, recently, Prof. Kang reported the crack based ultra-sensitive strain sensor inspired by the geometry of a spider's slit organ. [33] Such a crack based sensor system could be useful in various applications requiring high sensitivity.

In this study, we developed sensor and strain gated switch with very high sensitivity using nanoscale crack. When a metal thin film having a relatively high elastic modulus is deposited on a polymer layer having a relatively low elastic modulus and a strain is applied, cracks are generated by a difference in elastic modulus of two bonded layer. The fine tips of the cracks in the metal thin layer can stick or fall off depending on the applied strain, and the electrical conductivity of metal thin film changes accordingly. The crack system can be used as a sensitive sensor by measuring the change in electrical conductivity depending on the applied strain. Therefore, when the crack geometry depending on the physical properties of the polymer substrate and metal layer constituting the system changes, the response characteristic of the sensor also changes. The purpose of this study is to fabricate ultra - sensitive strain sensors and strain gating switches by forming cracks with varying not only width but also depth according to the strain applied.

Second, bending deformation caused by the residual stress of the thin films constituting the device can be utilized. Bending deformation has been studied to be avoided by optimizing the material and the process because clogging of the automated production line during the substrate manufacturing process or cracking and destruction can occur when the deformation is severe. [34] However, it is possible to fabricate new

functional platforms such as transistors and drug delivery applications by appropriately using the bending characteristics. However, as in the case of cracks, it is possible to fabricate new functional platforms such as soft robotics, conductors and drug delivery applications by appropriately using the bending characteristics.

In this study, we developed a rollable platform which can perform the rolling and spreading operation repeatedly using the bending deformation of the hetero structure layer design, and implemented various electronic devices such as temperature sensor, strain sensor, OLED, and heater on the rollable platform. When the pre-stretched stretchable substrate is bonded to the rigid film and then is released, it shrinks and generates a bending moment on the entire film. The generated moment causes the entire film to be rolled to a specific radius, depending on the degree of the pre-strain. Additionally, the rollable platform can be unfolded by pneumatic pressure through air channel which formed between the double layers. The purpose of this study is to develop multi-functional systems by using the transformability of the rollable platform combined with various electronic devices.

Lastly, we used the deformation response characteristics of the substrate thickness variation of the flexible electronic device. In order to fabricate a flexible device with mechanical durability against harsh deformation, it is important to analyze the mechanical properties of the materials of thin films composed of the device. The mechanical properties of thin films were mainly obtained by experimental method [35,36] such as nano-indentation test, and theoretical methods [37,38] using the density functional theory (DFT), the molecular dynamics (MD) or the molecular mechanics (MM) simulation.

However, these methods have limitations in accurate characterization due to problems such as thickness, purity and crystallinity of the thin film material. Therefore, by controlling the thickness of the substrate on which the thin film is formed, it is possible to control the magnitude of the applied strain to the materials by deformation, so that the mechanical properties such as the actual fracture point of thin film can be analyzed.

In this study, the mechanical durability of the perovskite thin film was evaluated through the cyclic bending test of the perovskite solar cell fabricated with different substrate thickness. Based on mechanical durability analysis of perovskite thin film, we have fabricated ultra-flexible perovskite solar cells with high efficiency and high durability. Until now, there have been lots of studies on bendable conducting electrodes to replace brittle TCOs for flexible perovskite solar cells for improve mechanical durability, such as graphene, carbon nanotubes, metal grids, and conductive polymers. [39-42] Nonetheless, perovskite solar cells using alternative electrodes have required to increase mechanical durability in harsh conditions as well as efficiency. The purpose of this study is to evaluate the bending durability of perovskite materials according to the thickness of the substrate and to implement a highly efficient and high flexible perovskite solar cells.

1.2. Thesis Outline

This thesis is organized into five chapters. Following this Chapter 1 on Introduction, Chapter 2 deals with the crack based sensory system could be helpful in various applications requiring high sensitivity. This chapter examines crack formation and behavior of crack widening, and presents potential uses of crack based sensor and switch for wearable devices.

Chapter 3 proposes a rollable platform could be useful in wearable electronic devices. This chapter focused on fabricating the rollable platform and the various electronic devices on rollable platform, and demonstration of rollable platform *in vivo* operation.

Finally, Chapter 4 is devoted to fabricate the ultra-flexible and high efficiency perovskite solar cells. In this chapter, fracture behavior of polycrystalline perovskite films were investigated by cyclic bending test depend on the substrate thickness, and demonstrates the large area perovskite solar cells sub-equal performance compared to small area devices by adopting hybrid transparent electrode.

1.3. References

- [1] T. Park, Y. S. Kang, S. Jang, S. W. Cha, M. Choi, S. J. Yoo, "A rollable ultra-light polymer electrolyte membrane fuel cell". *NPG Asia Materials* **9**, e384 (2017).
- [2] J. Yoon, H. Sung, G. Lee, W. Cho, N. Ahn, H. S. Jung, M. Choi, "Superflexible, high-efficiency perovskite solar cells utilizing graphene electrodes: towards future foldable power sources". *Energy & Environmental Science* **10**, 337-345 (2017).
- [3] W. Liu, M. S. Song, B. Kong, Y. Cui, "Flexible and stretchable energy storage: recent advances and future perspectives". *Advanced Materials* **29**, 1603436 (2017).
- [4] J. Bae, M. K. Song, Y. J. Park, J. M. Kim, M. Liu, Z. L. Wang, "Fiber supercapacitors made of nanowire-fiber hybrid structures for wearable/flexible energy storage". *Angewandte Chemie International Edition* **50**, 1683-1687 (2011).
- [5] J. H. Koo, S. Jeong, H. J. Shim, D. Son, J. Kim, D. C. Kim, S. Choi, J.-I. Hong, D.-H. Kim, "Wearable electrocardiogram monitor using carbon nanotube electronics and color-tunable organic light-emitting diodes". *ACS nano* **11**, 10032-10041 (2017).
- [6] J. Kim, H. J. Shim, J. Yang, M. K. Choi, D. C. Kim, J. Kim, T. Hyeon, D. H. Kim, "Ultrathin quantum dot display integrated with wearable electronics". *Advanced Materials* **29**, 1700217 (2017).
- [7] J. H. Koo, D. C. Kim, H. J. Shim, T. H. Kim, D. H. Kim, "Flexible

- and Stretchable Smart Display: Materials, Fabrication, Device Design, and System Integration". *Advanced Functional Materials* **28**, 1801834 (2018).
- [8] R. S. Dahiya, M. Valle, in *Robotic Tactile Sensing*. (Springer, 2013), pp. 177-194.
- [9] J. Kim, M. Lee, H. J. Shim, R. Ghaffari, H. R. Cho, D. Son, Y. H. Jung, M. Soh, C. Choi, S. Jung, "Stretchable silicon nanoribbon electronics for skin prosthesis". *Nature communications* **5**, 5747 (2014).
- [10] Y. Hattori, L. Falgout, W. Lee, S. Y. Jung, E. Poon, J. W. Lee, I. Na, A. Geisler, D. Sadhwani, Y. Zhang, "Multifunctional skin-like electronics for quantitative, clinical monitoring of cutaneous wound healing". *Advanced healthcare materials* **3**, 1597-1607 (2014).
- [11] H. Lee, T. K. Choi, Y. B. Lee, H. R. Cho, R. Ghaffari, L. Wang, H. J. Choi, T. D. Chung, N. Lu, T. Hyeon, "A graphene-based electrochemical device with thermoresponsive microneedles for diabetes monitoring and therapy". *Nature nanotechnology* **11**, 566 (2016).
- [12] S. Choi, S. I. Han, D. Jung, H. J. Hwang, C. Lim, S. Bae, O. K. Park, C. M. Tschabrunn, M. Lee, S. Y. Bae, "Highly conductive, stretchable and biocompatible Ag–Au core–sheath nanowire composite for wearable and implantable bioelectronics". *Nature nanotechnology*, 1 (2018).
- [13] W. H. Yeo, Y. S. Kim, J. Lee, A. Ameen, L. Shi, M. Li, S. Wang, R. Ma, S. H. Jin, Z. Kang, "Multifunctional epidermal electronics

- printed directly onto the skin". *Advanced Materials* **25**, 2773-2778 (2013).
- [14] D.-H. Kim, N. Lu, R. Ma, Y.-S. Kim, R.-H. Kim, S. Wang, J. Wu, S. M. Won, H. Tao, A. Islam, "Epidermal electronics". *science* **333**, 838-843 (2011).
- [15] J. T. Muth, D. M. Vogt, R. L. Truby, Y. Mengüç, D. B. Kolesky, R. J. Wood, J. A. Lewis, "Embedded 3D printing of strain sensors within highly stretchable elastomers". *Advanced Materials* **26**, 6307-6312 (2014).
- [16] C. L. Choong, M. B. Shim, B. S. Lee, S. Jeon, D. S. Ko, T. H. Kang, J. Bae, S. H. Lee, K. E. Byun, J. Im, "Highly stretchable resistive pressure sensors using a conductive elastomeric composite on a micropylramid array". *Advanced materials* **26**, 3451-3458 (2014).
- [17] X. Wang, Y. Gu, Z. Xiong, Z. Cui, T. Zhang, "Silk-molded flexible, ultrasensitive, and highly stable electronic skin for monitoring human physiological signals". *Advanced materials* **26**, 1336-1342 (2014).
- [18] D. J. Lipomi, Z. Bao, "Stretchable and ultraflexible organic electronics". *MRS Bulletin* **42**, 93-97 (2017).
- [19] A. J. Heeger, "Semiconducting and metallic polymers: the fourth generation of polymeric materials (Nobel lecture)". *Angewandte Chemie International Edition* **40**, 2591-2611 (2001).
- [20] J. A. Fan, W.-H. Yeo, Y. Su, Y. Hattori, W. Lee, S.-Y. Jung, Y. Zhang, Z. Liu, H. Cheng, L. Falgout, "Fractal design concepts for stretchable electronics". *Nature communications* **5**, 3266 (2014).

- [21] T. Q. Trung, S. Ramasundaram, B. U. Hwang, N. E. Lee, "An all-elastomeric transparent and stretchable temperature sensor for body-attachable wearable electronics". *Advanced Materials* **28**, 502-509 (2016).
- [22] S. Savagatrup, A. D. Printz, T. F. O'Connor, A. V. Zaretski, D. J. Lipomi, "Molecularly stretchable electronics". *Chemistry of Materials* **26**, 3028-3041 (2014).
- [23] Y. Lee, M. Shin, K. Thiyagarajan, U. Jeong, "Approaches to stretchable polymer active channels for deformable transistors". *Macromolecules* **49**, 433-444 (2015).
- [24] D. Kim, D. Kim, H. Lee, Y. R. Jeong, S. J. Lee, G. Yang, H. Kim, G. Lee, S. Jeon, G. Zi, "Body-Attachable and Stretchable Multisensors Integrated with Wirelessly Rechargeable Energy Storage Devices". *Advanced Materials* **28**, 748-756 (2016).
- [25] C. Dagdeviren, Y. Su, P. Joe, R. Yona, Y. Liu, Y.-S. Kim, Y. Huang, A. R. Damadoran, J. Xia, L. W. Martin, "Conformable amplified lead zirconate titanate sensors with enhanced piezoelectric response for cutaneous pressure monitoring". *Nature communications* **5**, 4496 (2014).
- [26] H. Guo, M.-H. Yeh, Y.-C. Lai, Y. Zi, C. Wu, Z. Wen, C. Hu, Z. L. Wang, "All-in-one shape-adaptive self-charging power package for wearable electronics". *ACS nano* **10**, 10580-10588 (2016).
- [27] C. Yan, J. Wang, P. S. Lee, "Stretchable graphene thermistor with tunable thermal index". *ACS nano* **9**, 2130-2137 (2015).
- [28] L. Gao, Y. Zhang, V. Malyarchuk, L. Jia, K.-I. Jang, R. C. Webb, H.

- Fu, Y. Shi, G. Zhou, L. Shi, "Epidermal photonic devices for quantitative imaging of temperature and thermal transport characteristics of the skin". *Nature communications* **5**, 4938 (2014).
- [29] R. C. Webb, A. P. Bonifas, A. Behnaz, Y. Zhang, K. J. Yu, H. Cheng, M. Shi, Z. Bian, Z. Liu, Y.-S. Kim, "Ultrathin conformal devices for precise and continuous thermal characterization of human skin". *Nature materials* **12**, 938 (2013).
- [30] N. Münzenrieder, G. Cantarella, C. Vogt, L. Petti, L. Büthe, G. A. Salvatore, Y. Fang, R. Andri, Y. Lam, R. Libanori, "Stretchable and conformable oxide thin-film electronics". *Advanced Electronic Materials* **1**, 1400038 (2015).
- [31] G. Schwartz, B. C.-K. Tee, J. Mei, A. L. Appleton, D. H. Kim, H. Wang, Z. Bao, "Flexible polymer transistors with high pressure sensitivity for application in electronic skin and health monitoring". *Nature communications* **4**, 1859 (2013).
- [32] K. H. Nam, I. H. Park, S. H. Ko, "Patterning by controlled cracking". *Nature* **485**, 221 (2012).
- [33] D. Kang, P. V. Pikhitsa, Y. W. Choi, C. Lee, S. S. Shin, L. Piao, B. Park, K.-Y. Suh, T.-i. Kim, M. Choi, "Ultrasensitive mechanical crack-based sensor inspired by the spider sensory system". *Nature* **516**, 222 (2014).
- [34] G. Webster, A. Ezeilo, "Residual stress distributions and their influence on fatigue lifetimes". *International Journal of Fatigue* **23**, 375-383 (2001).
- [35] S. Sun, Y. Fang, G. Kieslich, T. J. White, A. K. Cheetham,

- "Mechanical properties of organic–inorganic halide perovskites, $\text{CH}_3\text{NH}_3\text{PbX}_3$ (X= I, Br and Cl), by nanoindentation". *Journal of Materials Chemistry A* **3**, 18450-18455 (2015).
- [36] Y. Rakita, S. R. Cohen, N. K. Kedem, G. Hodes, D. Cahen, "Mechanical properties of APbX_3 (A= Cs or CH_3NH_3 ; X= I or Br) perovskite single crystals". *MRS Communications* **5**, 623-629 (2015).
- [37] J. Yu, M. Wang, S. Lin, "Probing the soft and nanoductile mechanical nature of single and polycrystalline organic–inorganic hybrid perovskites for flexible functional devices". *ACS nano* **10**, 11044-11057 (2016).
- [38] J. Feng, "Mechanical properties of hybrid organic-inorganic $\text{CH}_3\text{NH}_3\text{BX}_3$ (B= Sn, Pb; X= Br, I) perovskites for solar cell absorbers". *Appl Materials* **2**, 081801 (2014).
- [39] M. Park, H. J. Kim, I. Jeong, J. Lee, H. Lee, H. J. Son, D. E. Kim, M. J. Ko, "Mechanically recoverable and highly efficient perovskite solar cells: investigation of intrinsic flexibility of organic–inorganic perovskite". *Advanced Energy Materials* **5**, 1501406 (2015).
- [40] W. Zhang, J. Xiong, S. Wang, W.-e. Liu, J. Li, D. Wang, H. Gu, X. Wang, J. Li, "Highly conductive and transparent silver grid/metal oxide hybrid electrodes for low-temperature planar perovskite solar cells". *Journal of Power Sources* **337**, 118-124 (2017).
- [41] Q. Luo, H. Ma, F. Hao, Q. Hou, J. Ren, L. Wu, Z. Yao, Y. Zhou, N. Wang, K. Jiang, "Carbon Nanotube Based Inverted Flexible Perovskite Solar Cells with All-Inorganic Charge Contacts".

Advanced Functional Materials **27**, 1703068 (2017).

- [42] J. H. Heo, D. H. Shin, D. H. Song, D. H. Kim, S. J. Lee, S. H. Im, "Super-flexible bis (trifluoromethanesulfonyl)-amide doped graphene transparent conductive electrodes for photo-stable perovskite solar cells". *Journal of Materials Chemistry A* **6**, 8251-8258 (2018).

Chapter 2.

Strain Gated Switch by Utilizing a Crack Based System

2.1. Introduction

Wearable electronics is a rapidly emerging research field because it integrates technology into human daily lives, and has potential applications in various areas such as human-machine interfacing [1-4], ubiquitous computing [5, 6], and healthcare [7-10]. In order to operate these devices, signal acquisition and processing are essential, and among various mechanical stimuli that can be sensed, stretching of the skin is one of the most readily available information. This strain may arise from voluntary movements of joints and muscles, or autonomic functions such as heartbeats and respiration, which then can be converted into electrical signals for processing. To date, various flexible strain sensors have been developed, including those based on nanowires [11-13], graphene [14-16], carbon nanotubes [17-19], and other materials [20-22]. However, these sensors require a signal processing circuit which would introduce complexities in device design. Instead of producing an analog signal then processing it, a simple strain-gated digital signal would be more appropriate for certain wearable applications such as motion capturing devices.[22] Strain gated

logic devices such as switches or transistors have been developed by using piezotronic nanowires [23-26], and metal/elastomer bilayer films.[27] Of these, piezotronic nanowire switches have been designed to have a low threshold strain ($\sim 1\%$), but their on-off ratios are low ($I_{\text{on}}/I_{\text{off}} \leq 95.7$).[24] Metal-elastomer bilayer switches have a high on-off ratio, but operate in the compressive strain regime and their threshold strain was relatively large ($\epsilon \geq 20\%$).[25] A switch that combines a high on-off ratio with low energy consumption and small threshold strain for detecting a tiny movement of the skin has yet to be demonstrated (**Figure. 2.1**).

Previously, Kang et al.[28] have reported a fractured metal thin film/elastomer bilayer strain sensor with a platinum/polyurethane acrylate (PUA) stack. In the present work, we found that by changing the crack widening behavior on the elastomer substrate, the resistance change becomes more sensitive to the applied strain, and hence we have used the device as a strain gated switch instead of a strain sensor. To achieve this purpose, we have replaced PUA with a highly stretchable ($\sim 200\%$ strain) and soft (elastic modulus ~ 5 MPa) silicone rubber as a substrate. Unlike a platinum/PUA stack, conduction pathway of the platinum/silicone rubber stack is completely broken at only over 2% strain. Using this strain-gated switch, we have fabricated logic elements such as AND, OR, NAND, and NOR gates and demonstrated a simple figure gesture induced complex electrical signaling.

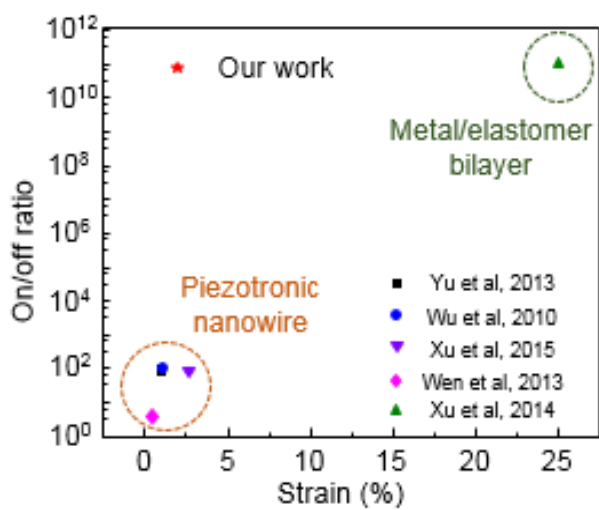


Figure 2.1. Comparison of on/off ratio with variation of strains between our work and the previous studies.

2.2. Experimental Methods

2.2.1. Fabrication of strain gated switch

Polydimethylsiloxane (PDMS) (Dow Corning, Sylgard 184) is bonded on glass by oxygen plasma treatment (CUTE-1MPR, Femto Science Inc.). Silicone rubber compounds (KEG-2000-60A/B, ShinEtus) were poured into a PDMS/glass mold. Then a glass cover was placed on the mixture, and 2 MPa pressure was applied at 140 °C on a hot plate. The silicone rubber is cured for 10 minutes, and subsequently the film is demolded. For curved switches, a silicone rubber film (250 μm thick) is stretched to 8% strain and another silicone rubber (250 μm thick) film is bonded to it by an oxygen plasma treatment for 40 second. For flat switches, a flat 500 μm thick silicone rubber film (5 x 15 mm) is used. For threshold strain-controllable switches, a silicone rubber film (250 μm thick) underlying substrate is stretched (0, 5, 10, 15 % strain) by a custom-built stretcher, then bonded to another silicone rubber film (250 μm thick) layer in an area of 5 x 3 mm by an oxygen plasma treatment. A 20 nm thick platinum layer is deposited on the elastomeric substrate by a sputter (sputter; Ultech Inc.). Then the stack is stretched by a custom-built stretcher in order to generate cracks (**Figure. 2.2, 2.11, and 2.13**).

2.2.2. Characterization

The switch is clamped in an all-electric test instrument (3342 UTM, Instron Co.) and stretched by using specified maximum strain and force at 1 mm/min. The resistance change is measured by a Lab View based PXI-4071 system (NI instrument).

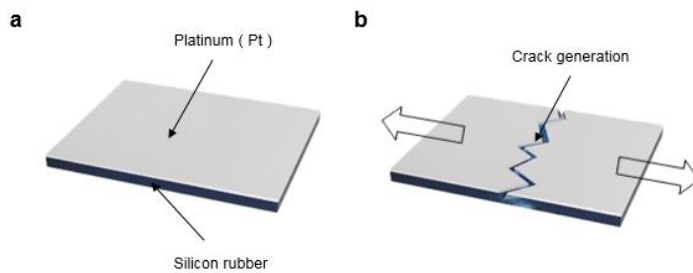


Figure 2.2. Fabrication process for the strain gated switch. (a) Deposition of platinum (Pt) onto the silicone rubber substrate. (b) Pt crack generation by stretching out the metal deposited silicone rubber substrate.

2.3. Result and Discussion

2.3.1. Structure of crack based strain gated switch

Figure. 2.3a illustrates the operating principle of the strain-gated switch. Cracks are formed on the metal-elastomer bilayer due to the difference of elastic modulus between the two layers, when the switch is stretched to 2% strain. When the device is stretched above a threshold, the crack opens up (**Figure. 2.3a**, top right), turning the switch ‘off’. And when the device is compressed, the crack closes (**Figure. 2.3a**, bottom right), turning the switch ‘on’. To confirm the operation of the switch, a simple circuit with a light emitting diode (LED) was used. When the switch stretched to over 2% strain, it is ‘off’, and the microscale cracks open up, which results in the LED turning off (**Figure. 2.3b**). When the switch is released, it is ‘on’, the microscale cracks close, and the LED turns on (**Figure. 2.3c**). The difference between the previously reported crack-based sensor [28] and the current switch is as follows. By changing the substrate from PUA film to the soft elastomeric material, the crack opening behavior is changed, and the use of silicone rubber results in a non-linear widening of the crack opening (**Figure. 2.3d**), as opposed to the linear opening that was seen in the previous sensors with PUA substrate.[28] This then translates into totally different behavior in resistance increase. As the strain applied to the devices increases, the resistance of switch increases dramatically, whereas the previous sensor showed linear increase (**Figure. 2.3e**).

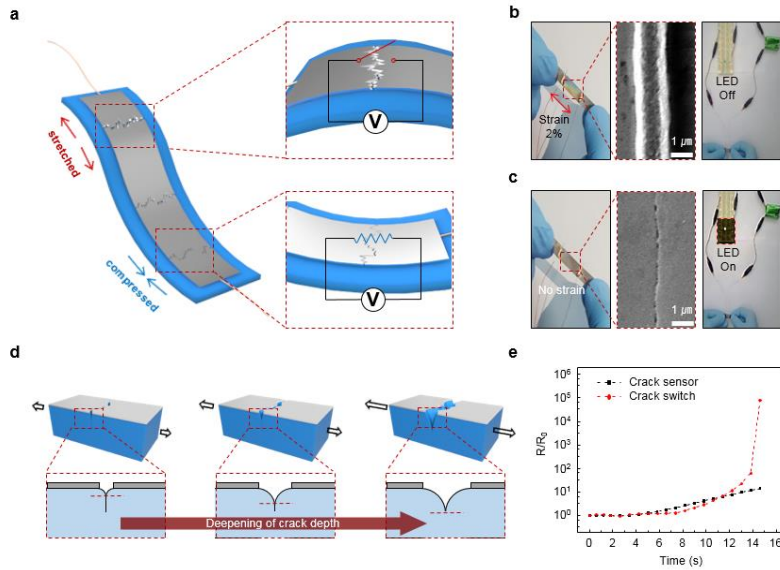


Figure 2.3. (a) Schematic illustration of operating strain-gated switches. (b, c) Photos for operating strain-gated switches and the corresponding SEM images of opened and closed cracks. (d) Schematic illustration of the super-exponential behavior of crack widening with variation of strain. (e) Comparison of normalized resistance variance between the crack sensor and the crack switch when strain is applied to the devices

2.3.2. Performance of crack based strain gated switch

To study the switching mechanism, we have measured the electrical resistance change of the metal film and the variation of geometrical features, such as crack depth and width, with the variation of applied strains. **Figure. 2.4a** shows the crack depth and width on the platinum/silicone rubber stack measured by atomic force microscopy (AFM) with the variation of strains. The results indicate that the crack depth increases as the applied strain increases, which leads to the super exponential behavior of widening of the crack.

The resistance change during repeated stretching and relaxation of the switch is shown in **Figure. 2.4b**. When 1.6% strain is applied, the device resistance increases approximately by 5 orders of magnitude, and when relaxed, the resistance decreases to the nominal value of ~30 ohms. The resistance is proportionally related to the crack width, and thus shows super exponential dependence on the applied strain. The resistance change is strongly affected by the distance between crack lips because a wider crack gap means the less electric contact point left. At 2% strain, the resistance of the device rises to infinite (at least $10^{12} \Omega$, **Figure. 2.4b**, inset) and the on-off ratio becomes $\sim 3 \times 10^{10}$, which value is the limit of the measurement equipment. This probably means that the cracks are so widened that the conduction path through the islands of the crack metal layer is broken, and it is not contributing to conduction anymore. An optical microscope image has been taken to confirm that the conduction path through the metal islands is completely broken and the islands are indeed not touching each other

(**Figure. 2.5**). Additionally, the crack switch can be used as a strain sensor as well, and the overall gauge factor determined from the definition $(\Delta R/R_0)/\varepsilon$ exceeds 6×10^6 at the strain range of 0 to 1.6% as shown in **Figure. 2.4b**. It is noted that resistance variation to the applied strain is non-linear (strain dependent gauge factor defined by $[\text{Gauge Factor} = (dR/R_0)/d\varepsilon]$ is shown in **Figure. 2.6**). The loading and unloading resistance changes are measured while subjecting the device to 1.6% strain in order to evaluate its hysteresis (**Figure. 2.4c**). The switch exhibits 0.1% hysteresis when measured by criteria used by Park and Yoon et al, [29, 30] which can be considered negligible. The response time to rapid stretching up to 0.4% strain is approximately 100 ms (**Figure. 2.4d**). This delay is presumably related to the viscoelasticity of the soft polymeric substrate, which opens up further tuning opportunity of the substrate mechanics, and the device characteristics. The delay in response is on par with the previous wearable devices such as wearable strain sensors and pressure sensors. [31, 32] Furthermore, the durability of the switch has been tested by cyclic loading and unloading, and showed repeatable performance up to 5000 cycles (**Figure. 2.7**).

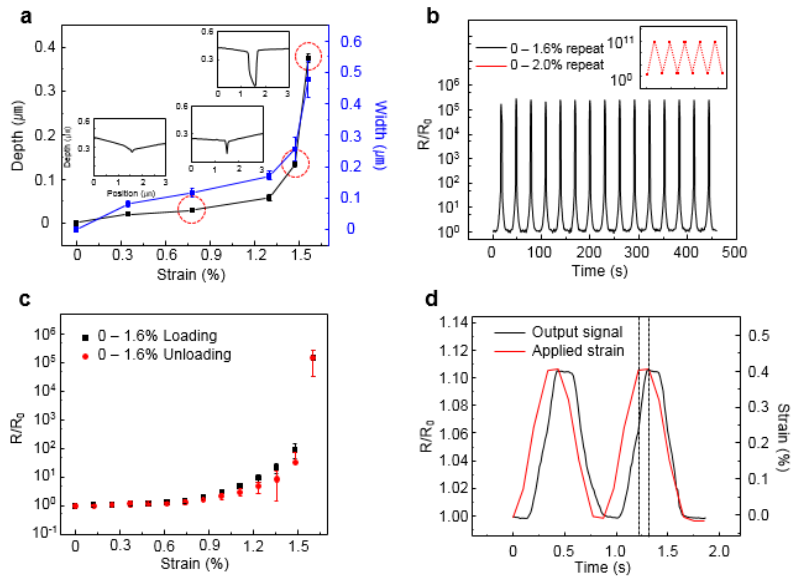


Figure 2.4. (a) The variation of depth and width with the variation of applied strain. (b) The graph of normalized resistance variance versus a strain of 1.6% in 15 cyclic tests. (Inset: 2.0% in 5 cyclic tests). (c) The standard deviation and the average over 5 different samples in the hysteresis test of the strain gated switch. Red and black dots show unloading and loading states, respectively. (d) The response time of the strain gated switch. The red and black lines indicate the input signal (strain of 0.4%), and the response time of the input strain, respectively

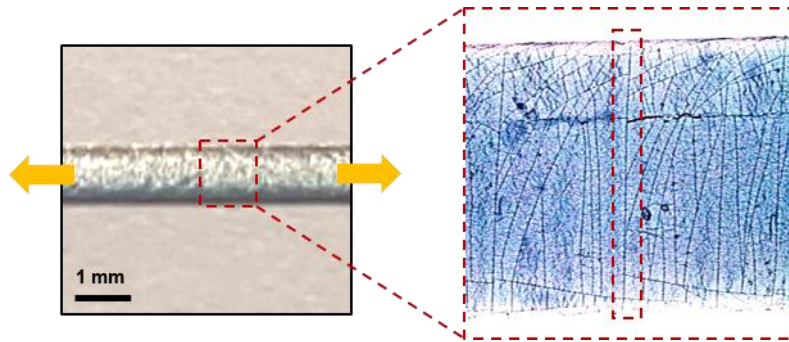


Figure 2.5. Optical microscope camera images of the Pt layer. The orange arrows indicate the tensile direction

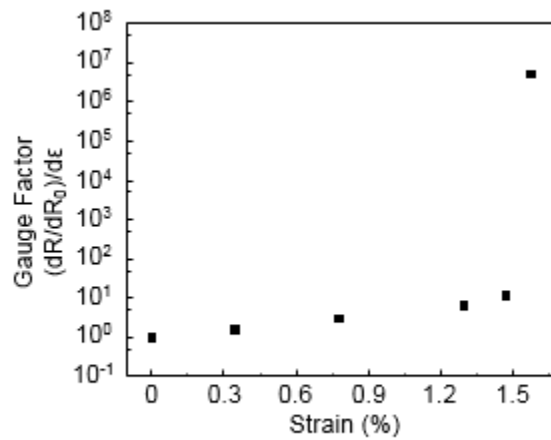


Figure 2.6. Strain-dependent gauge factor by taking the derivative of R/R_0 with respect to strains from 0 % to 1.6 %

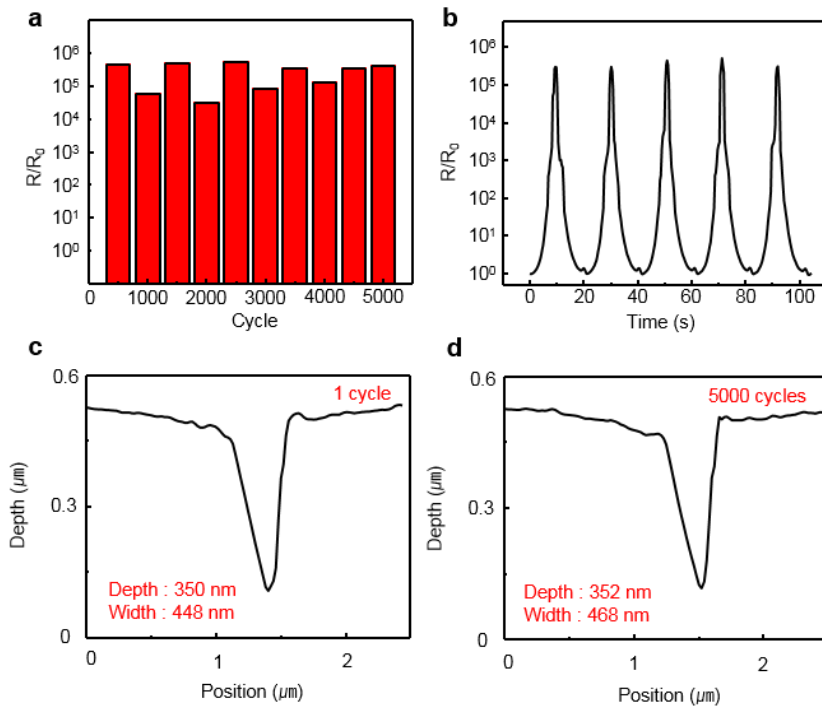


Figure 2.7. A marathon test of the strain gated switch by repeating about 5,000 cycles of loading/unloading process at strain from 0 % to 1.6 %. (a) A final normalized resistance of the marathon test at a certain period (about 500 cycles). (b) Loading/unloading test after 5,000 cyclic tests. The depth profile of crack measured by AFM at 1.6 % strain. After 1 cycle (c) and 5000 cycles (d) of loading/unloading process at strain from 0 % to 1.6 %

2.3.3. Theoretical modeling of crack based strain gated switch

Let us give a brief theoretical description of the super-exponential behavior based on the direct measurements of the crack geometry. The depth of crack changes according to the strain applied to the substrate, which results in a non-linear change of the gap between crack lips as measured by AFM (Atomic Force Microscopy) (**Figure. 2.4a**). While the crack switch is stretched below 1.3% strain, the crack opening slowly increases. Above 1.3%, the crack starts to open dramatically and it leads to a dramatic increase of the resistance. We analyze the relevant AFM data which are the crack depth and width (**Figure. 2.8**). The sample slab can be divided to the bulk and the near surface regions (**Figure. 2.8a**). The latter is cut by the crack to the maximum depth D_0 (**Figure. 2.8a**), which weakens the surface spring constant when the cut opens. When the strain is 0%, the cut is tightly closed by the surface self-adhesion forces. At non-zero strains, the cut starts to open (**Figure. 2.8a**) to the depth D and therefore the cross-section of the surface slab $(D_0 - D)d$ is reduced (d is the broadness of the slab). The reduced effective surface spring constant for the slab of the characteristic length L takes the form $E \frac{(D_0 - D)d}{L}$ where E is the elastic modulus. Meantime, the sample slab without cuts is stretched proportionally to the strain ε and intercrack space is stretched accordingly. The parallel crack system can be modelled by the series of alternating cut and uncut slabs.

The force within the surface layer is phenomenologically described by the Hooke's equation for the "springs in series" where the force is the same for each of "springs":

$$E \frac{(D_0 - D)d}{L} W = E \frac{D_0 d}{L} \frac{W_0}{\varepsilon_0} \varepsilon \quad (\text{S1})$$

(parameters are shown in **Figure. 2.8a**). Physically, Equation S1 roughly describes the softening of the surface layer and the following super-linear expansion of the crack width W to keep the surface force balance compared to the proportionality law that follows Equation S1 if D were zero:

$$W = \frac{W_0}{\varepsilon_0} \varepsilon \quad (\text{S2})$$

where W_0/ε_0 is a proportionality constant. From Equation S1, it follows:

$$W(\varepsilon) = \frac{E \frac{d}{L} D_0 W_0 \varepsilon / \varepsilon_0}{E \frac{d}{L} (D_0 - D(\varepsilon))} = \frac{W_0 \varepsilon / \varepsilon_0}{1 - D(\varepsilon) / D_0} \quad (\text{S3})$$

and then

$$\frac{\varepsilon_0}{W_0} \left(1 - \frac{D(\varepsilon)}{D_0} \right) = \frac{\varepsilon}{W(\varepsilon)} \quad (\text{S4})$$

Rewriting Equation S4, we get

$$\frac{\varepsilon_0}{W_0} \left(1 - \frac{X}{D_0} \right) = Y \quad (\text{S5})$$

Here, we denoted $Y = \frac{\varepsilon}{W(\varepsilon)}$ and $X = D$. **Figure. 2.8d** shows the plot of the crack depth vs $\frac{\varepsilon}{W(\varepsilon)}$ according to Equation S5. To estimate X and Y - intercepts, the data are linearly fitted and these values are calculated to be 660 nm and 130 nm/%, respectively. The values represent D_0 and W_0/ε_0 , respectively. With the fitting values, the width of crack lip opening with

respect to the input strain is plotted in **Figure. 2.8c** (red dots) from Equation S1 to compare with the AFM data (black dots) and find a reasonable agreement. To additionally prove that the sensor resistance corresponds to the system of parallel cracks, we plot here (blue triangles) the function $W_0 \ln(R/R_0) = W$ which follows the theory of straightened parallel cracks with the fitting parameter $W_0 = 100 \text{ nm}$. From **Figure. 2.8e** one can see that the proportionality of $100 \ln(R/R_0)$ to experimental super-linear W reasonably holds for all strains as well.

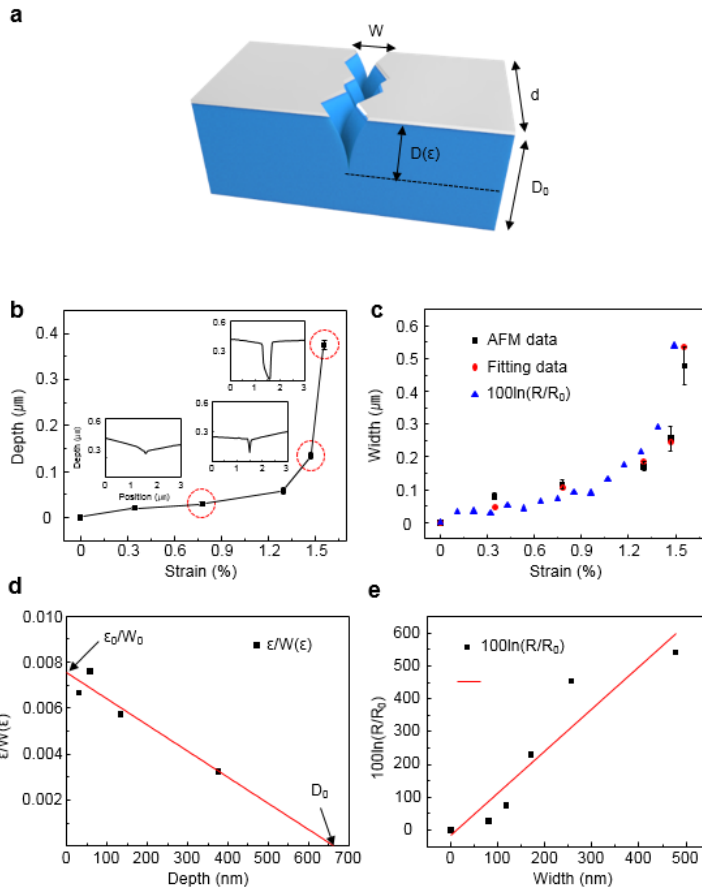


Figure 2.8. (a) Definition of parameters in the strain gated switch. (b) The variation of depth with the variation of applied strain, (c) The width of crack lip opening with respect to applied strain. Black dots were measured by AFM, red dots were plotted based on our theoretical modeling, and blue dots were plotted based on theoretical modeling by using measured resistance variation. (d) The plot of $\epsilon/W(\epsilon)$ with respect to the crack depth (e) The $100 \ln(R/R_0)$ with respect to the crack width

2.3.4. Applications of crack based strain gated switch

For a simple demonstration of how the strain-gated switches can be used in wearable devices, we have constructed AND, OR, NAND and NOR gates by combinations of the switches. In the case of an AND gate, two switches are linearly connected, and the circuit is electrically connected only when the two switches are “on” (**Figure. 2.9a**). If the switches are mounted on different fingers which then are stretched, the input becomes “1,1”, the circuit is electrically connected, and the LED turns on (**Figure. 2.9b**). In the case of an OR gate, two switches are connected in parallel as shown in **Figure. 2.9c**. In this case, only when the two fingers bent and the logic input becomes “0,0”, the circuit is electrically disconnected and LED turns off (**Figure. 2.9d**). AND and OR gates are built by using two open collector circuits shown in **Figure. 2.10a and b**. When the switch is compressed, the device resistance ($\sim 30 \Omega$) is much lower than that of the pull-down resistor ($\sim 10 \text{ M}\Omega$), hence the logic output is “1”. When the switch is stretched and turns “off”, the logic output becomes “0” as V_{out} is directly connected to ground (GND). Circuit diagrams for NAND and NOR gates are shown in **Figure. 2.9e and g**. In the case of a NAND gate, the LED is off when the two fingers are straight and input is “1,1” as shown in **Figure. 2.9f**. In the case of a NOR gate, the LED turns on while the two fingers are bent and the input becomes “0,0” (**Figure. 2.9h**). NAND and NOR gates are demonstrated with a totem pole crack switch circuit. By appropriate placement, the states of the switches can be designed to be opposite at all times by mounting them together with the metal layer on the opposing sides

(Figure. 2.10c and d). Depending on the motion of the joint, the combination of the switch states can lead to the logical output of either “1” or “0”. Such strain gated logic devices can be used to provide more advanced responses from human skin movements.

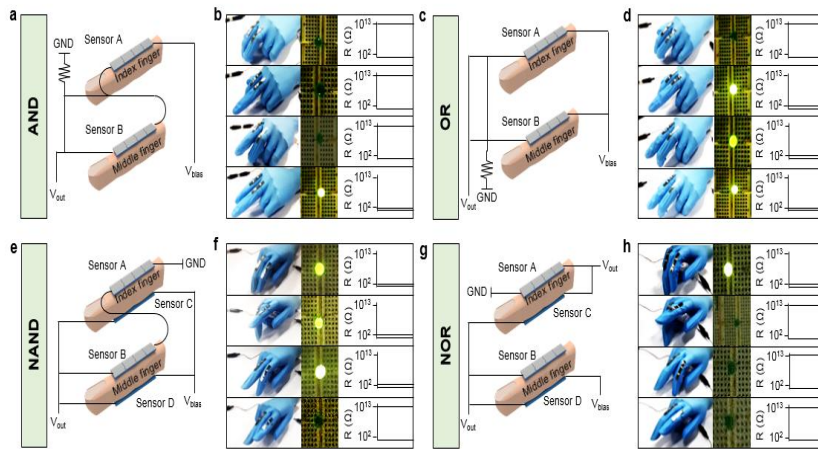


Figure 2.9. Four logic gates with strain gated switches. (a, c, e and g) Schematic illustrations of AND (a), OR (c), NAND (e), and NOR (g) logic gates. Depending on the motion of the joint, the combination of the switch states led to logical output of either “1” or “0”. (b, d, f and h) Demonstrations of LED “on/off” with respect to the corresponding logical output. The measured electrical output resistances of AND, OR, NAND, and NOR gates versus the mechanical input strains by the motion of the joint.

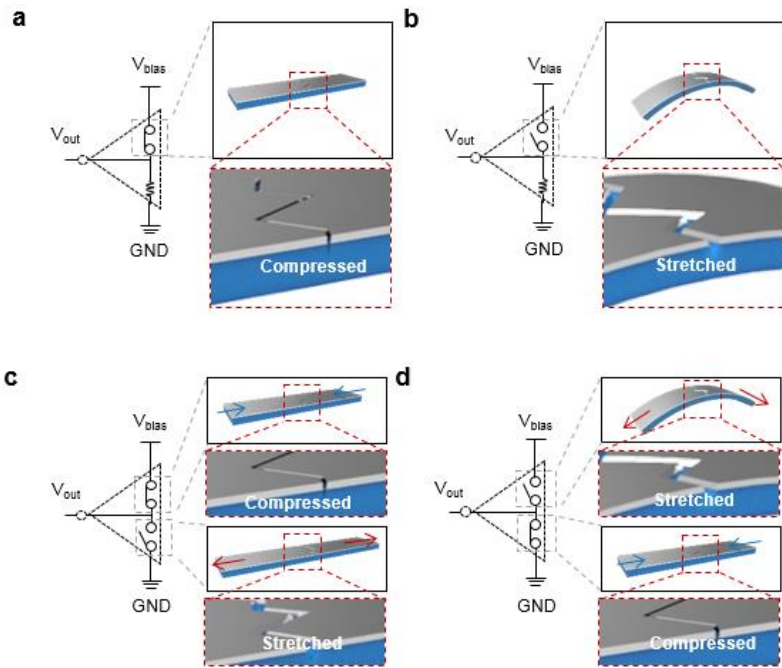


Figure 2.10. Operating principle of a motion induced logic gate. (a,b) open collector crack switch circuits, (c,d) totem pole crack switch circuit

As human skin can be stretched to various degrees according to movements of joints and muscles, the ability to manipulate the threshold strain of the switches is necessary for their integration in wearable devices. **Figure. 2.11a** illustrates the fabrication process of a curved switch which critical radius of curvature is shifted. Silicone rubber (250 μm thickness) substrate is stretched to strain 8% and another silicone rubber (250 μm thickness) substrate is bonded by treating O_2 plasma for 40 seconds. Releasing the two layered substrates is followed and thin Pt layer (20 nm) is deposited. Bending the metal deposited substrate into 12.5 mm radii is for crack generation on epilayer. **Figure. 2.11b** illustrates a conceptual depiction of a curved switch which needs to unfold before the cracks can start widening. Therefore, curved switches would have shifted threshold strains, depending on their radius of curvature. By mounting two switches with different threshold strains on a single finger, the output level controlled by the degree of finger joint flexion can become “0,1”, “1,1” or “1,0”, at fully flexed, semi-flexed, and fully extended conditions, respectively (**Figure. 2.11c**). The switches and their combinations can be further integrated into a hand-worn device where finger-gestures can be translated into single decimal numerals on a seven-segment display, without requiring additional signal processing circuits. In order to create 7 distinct input signals with 5 fingers, 2 additional switches with shifted threshold strain were fabricated and attached to two fingers. Photographs of the seven-segment display that indicates the movement of five fingers are shown in **Figure. 2.11d and e**. The thumb and the ring finger bend and the output logic signal becomes “0”, the middle finger is fully stretched and the output logic signal becomes “1,0”, the index

finger is semi-flex and the output logic signal becomes “1,1” and the little finger is fully stretched and the output logic signal becomes “1”. Integrating each switch with each segment, number “7” is presented on the panel as shown in **Figure. 2.11d**. Meanwhile, the fully stretching thumb, the index finger, the ring finger and the little finger, and the fully flexing middle finger present number “2” (**Figure. 2.11e**). Details of signals expressed by fingers with the switch system and all the numbers (0~9) presented by using the seven-segment are shown in **Figure. 2.12**.

In addition to shifting critical radii of curvature, changing the threshold strain is shown in **Figure. 2.13**. For utilization of these switches in wearable devices on various body parts with applicable strain ranges such as neck (< 0.5%), face (< 2%) and hand (< 20%), the ability to manipulate the threshold strain of flat devices is required. [33] The range of threshold strains that can be achieved is 2 to 20%.

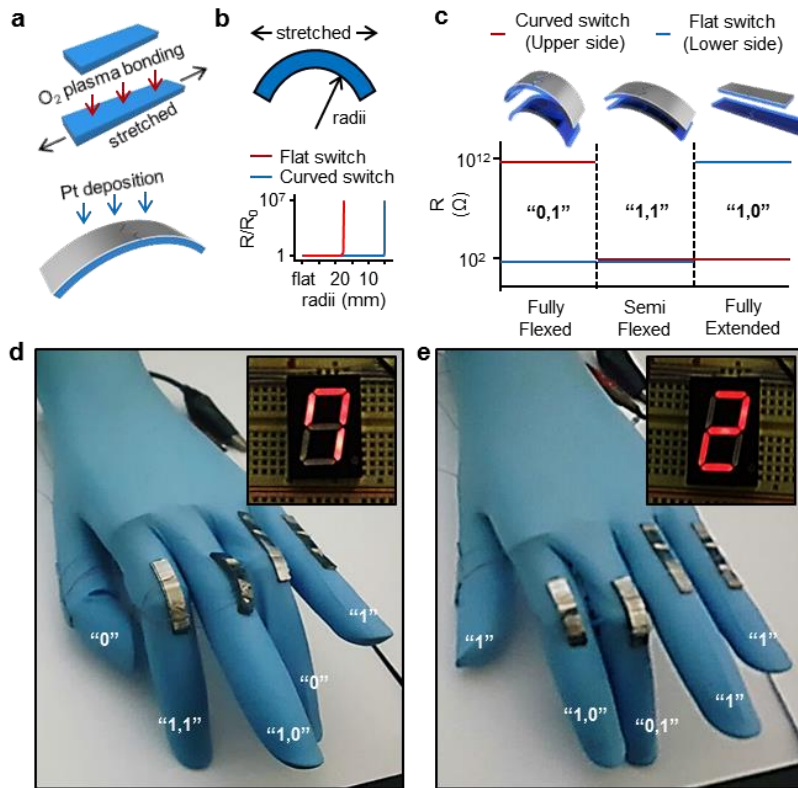


Figure 2.11. (a) Schematic illustration of fabrication of a curved switch. (b) Shift of the threshold strain of the curved switch due to the predefined shape. (c) Resistance variance of the combination of the curved switch (upper side) and flat switch (lower side). Three output levels were created by mounting two switches with varied motions of the joints on fingers. (d and e) Photographs of output logic signals, “7” (d) and “2” (e), that appeared on the seven segment display in accordance with varied motions of the five fingers.

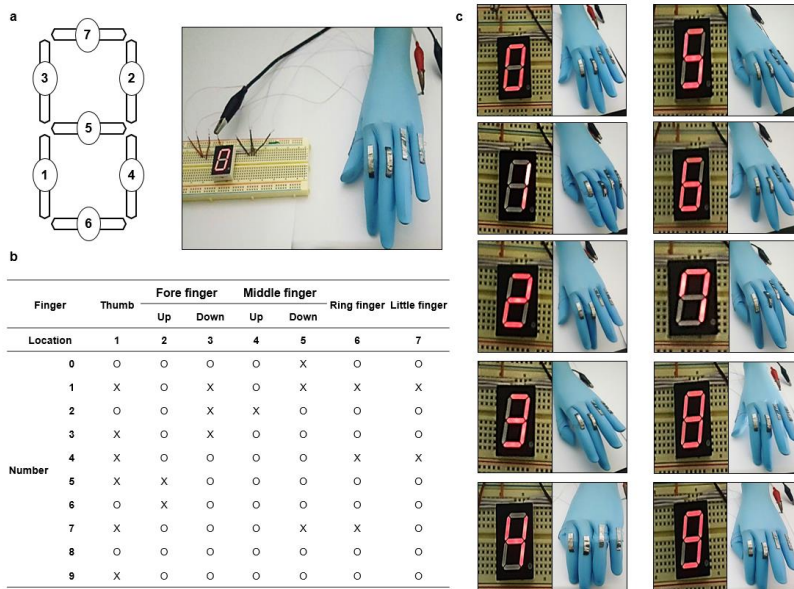


Figure 2.12. (a) Composition of seven-segment connected with the strain gated switches, (b) Logical table showing the relation of the expressing number and the motion of fingers, (c) Demonstration of expressing numbers from “0” to “9” with the varied motion of fingers.

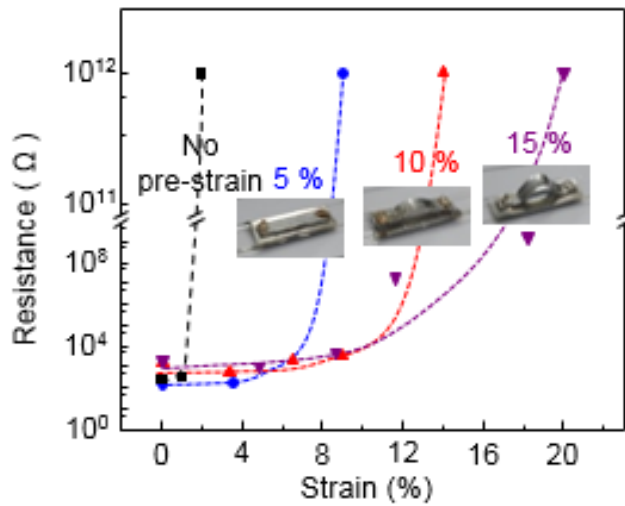


Figure 2.13. A graph of resistance with varied strains, which shows the controllable threshold strain with variation of applied pre-strain of lower substrate from 0% to 15 %

2.4. Conclusion

We have demonstrated a strain-gated, crack-based switch that takes advantage of super exponential of crack widening under tensile strain. The switch exhibits ultrahigh on-off ratio and low threshold strain that are required for low energy consumption and detection of small strains. We have developed a theoretical model to predict the resistance change of the device depending on the crack widening, and showed that the predictions are consistent with the experiments. Logic gates (AND, OR, NAND, NOR) have been constructed by using multiple switches and appropriate circuit design, and finger-gesture translation into individual numbers on a seven-segment display has been demonstrated. The switch presented in this paper exhibits excellent reliability, low energy consumption, and tunable threshold strain, which makes it an attractive candidate for integration into various wearable devices.

2.5. References

- [1] W. Wu, X. Wen, Z. L. Wang, "Taxel-addressable matrix of vertical-nanowire piezotronic transistors for active and adaptive tactile imaging". *Science* 340, 952-957 (2013).
- [2] E. Roh, B.-U. Hwang, D. Kim, B.-Y. Kim, N.-E. Lee, "Stretchable, transparent, ultrasensitive, and patchable strain sensor for human-machine interfaces comprising a nanohybrid of carbon nanotubes and conductive elastomers". *ACS nano* 9, 6252-6261 (2015).
- [3] S. Lim, D. Son, J. Kim, Y. B. Lee, J. K. Song, S. Choi, D. J. Lee, J. H. Kim, M. Lee, T. Hyeon, "Transparent and stretchable interactive human machine interface based on patterned graphene heterostructures". *Advanced Functional Materials* 25, 375-383 (2015).
- [4] J. Lee, H. Kwon, J. Seo, S. Shin, J. H. Koo, C. Pang, S. Son, J. H. Kim, Y. H. Jang, D. E. Kim, "Conductive Fiber-Based Ultrasensitive Textile Pressure Sensor for Wearable Electronics". *Advanced materials* 27, 2433-2439 (2015).
- [5] P. Bonato, "Wearable sensors and systems". *IEEE Engineering in Medicine and Biology Magazine* 29, 25-36 (2010).
- [6] K. Jost, D. Stenger, C. R. Perez, J. K. McDonough, K. Lian, Y. Gogotsi, G. Dion, "Knitted and screen printed carbon-fiber supercapacitors for applications in wearable electronics". *Energy & Environmental Science* 6, 2698-2705 (2013).
- [7] D.-H. Kim, R. Ghaffari, N. Lu, J. A. Rogers, "Flexible and stretchable electronics for biointegrated devices". *Annual review of biomedical engineering* 14, 113-128 (2012).
- [8] C. Wang, D. Hwang, Z. Yu, K. Takei, J. Park, T. Chen, B. Ma, A.

- Javey, "User-interactive electronic skin for instantaneous pressure visualization". *Nature materials* 12, 899-904 (2013).
- [9] S. Lee, A. Reuveny, J. Reeder, S. Lee, H. Jin, Q. Liu, T. Yokota, T. Sekitani, T. Isoyama, Y. Abe, "A transparent bending-insensitive pressure sensor". *Nature nanotechnology*, (2016).
- [10] A. Chortos, J. Liu, Z. Bao, "Pursuing prosthetic electronic skin". *Nature Materials* 15, 937-950 (2016).
- [11] Q. Liao, M. Mohr, X. Zhang, Z. Zhang, Y. Zhang, H.-J. Fecht, "Carbon fiber-ZnO nanowire hybrid structures for flexible and adaptable strain sensors". *Nanoscale* 5, 12350-12355 (2013).
- [12] W. Zhang, R. Zhu, V. Nguyen, R. Yang, "Highly sensitive and flexible strain sensors based on vertical zinc oxide nanowire arrays". *Sensors and Actuators A: Physical* 205, 164-169 (2014).
- [13] K. K. Kim, S. Hong, H. M. Cho, J. Lee, Y. D. Suh, J. Ham, S. H. Ko, "Highly sensitive and stretchable multidimensional strain sensor with prestrained anisotropic metal nanowire percolation networks". *Nano letters* 15, 5240-5247 (2015).
- [14] H. Tian, Y. Shu, Y.-L. Cui, W.-T. Mi, Y. Yang, D. Xie, T.-L. Ren, "Scalable fabrication of high-performance and flexible graphene strain sensors". *Nanoscale* 6, 699-705 (2014).
- [15] Y. Wang, L. Wang, T. Yang, X. Li, X. Zang, M. Zhu, K. Wang, D. Wu, H. Zhu, "Wearable and highly sensitive graphene strain sensors for human motion monitoring". *Advanced Functional Materials* 24, 4666-4670 (2014).
- [16] Y. Qin, Q. Peng, Y. Ding, Z. Lin, C. Wang, Y. Li, F. Xu, J. Li, Y. Yuan, X. He, "Lightweight, superelastic, and mechanically flexible graphene/polyimide nanocomposite foam for strain sensor application". *ACS nano* 9, 8933-8941 (2015).
- [17] K. Kanao, S. Harada, Y. Yamamoto, W. Honda, T. Aric, S. Akita, K.

- Takei, "Highly selective flexible tactile strain and temperature sensors against substrate bending for an artificial skin". *RSC Advances* 5, 30170-30174 (2015).
- [18] S. Ryu, P. Lee, J. B. Chou, R. Xu, R. Zhao, A. J. Hart, S.-G. Kim, "Extremely elastic wearable carbon nanotube fiber strain sensor for monitoring of human motion". *ACS nano* 9, 5929-5936 (2015).
- [19] S. J. Park, J. Kim, M. Chu, M. Khine, "Highly Flexible Wrinkled Carbon Nanotube Thin Film Strain Sensor to Monitor Human Movement". *Advanced Materials Technologies* 1, (2016).
- [20] T. Lee, Y. W. Choi, G. Lee, P. V. Pikhitsa, D. Kang, S. M. Kim, M. Choi, "Transparent ITO mechanical crack-based pressure and strain sensor". *Journal of Materials Chemistry C* 4, 9947-9953 (2016).
- [21] G.-H. Lim, N.-E. Lee, B. Lim, "Highly sensitive, tunable, and durable gold nanosheet strain sensors for human motion detection". *Journal of Materials Chemistry C* 4, 5642-5647 (2016).
- [22] S. Chen, Z. Lou, D. Chen, K. Jiang, G. Shen, "Polymer-Enhanced Highly Stretchable Conductive Fiber Strain Sensor Used for Electronic Data Gloves". *Advanced Materials Technologies* 1, (2016).
- [23] W. Wu, Y. Wei, Z. L. Wang, "Strain-Gated Piezotronic Logic Nanodevices". *Advanced Materials* 22, 4711-4715 (2010).
- [24] R. Yu, W. Wu, Y. Ding, Z. L. Wang, "GaN nanobelt-based strain-gated piezotronic logic devices and computation". *ACS nano* 7, 6403-6409 (2013).
- [25] M. Peng, Y. Liu, A. Yu, Y. Zhang, C. Liu, J. Liu, W. Wu, K. Zhang, X. Shi, J. Kou, "Flexible self-powered GaN ultraviolet photoswitch with piezo-phototronic effect enhanced on/off ratio". *ACS nano* 10, 1572-1579 (2015).
- [26] R. Yu, W. Wu, C. Pan, Z. Wang, Y. Ding, Z. L. Wang, "Piezo-

- phototronic Boolean Logic and Computation Using Photon and Strain Dual-Gated Nanowire Transistors". *Advanced Materials* 27, 940-947 (2015).
- [27] B. Xu, D. Chen, R. C. Hayward, "Mechanically gated electrical switches by creasing of patterned metal/elastomer bilayer films". *Advanced Materials* 26, 4381-4385 (2014).
- [28] D. Kang, P. V. Pikhitsa, Y. W. Choi, C. Lee, S. S. Shin, L. Piao, B. Park, K.-Y. Suh, T.-i. Kim, M. Choi, "Ultrasensitive mechanical crack-based sensor inspired by the spider sensory system". *Nature* 516, 222-226 (2014).
- [29] S. G. Yoon, H.-J. Koo, S. T. Chang, "Highly stretchable and transparent microfluidic strain sensors for monitoring human body motions". *ACS applied materials & interfaces* 7, 27562-27570 (2015).
- [30] B. Park, J. Kim, D. Kang, C. Jeong, K. S. Kim, J. U. Kim, P. J. Yoo, T. i. Kim, "Dramatically Enhanced Mechanosensitivity and Signal-to-Noise Ratio of Nanoscale Crack-Based Sensors: Effect of Crack Depth". *Advanced Materials* 28, 8130-8137 (2016).
- [31] Y. Tai, M. Mülle, I. A. Ventura, G. Lubineau, "A highly sensitive, low-cost, wearable pressure sensor based on conductive hydrogel spheres". *Nanoscale* 7, 14766-14773 (2015).
- [32] Y. W. Choi, D. Kang, P. V. Pikhitsa, T. Lee, S. M. Kim, G. Lee, D. Tahk, M. Choi, "Ultra-sensitive Pressure sensor based on guided straight mechanical cracks". *Scientific Reports* 7, (2017).
- [33] T. Q. Trung, N. E. Lee, "Flexible and Stretchable Physical Sensor Integrated Platforms for Wearable Human-Activity Monitoring and Personal Healthcare". *Advanced materials*, (2016).

Chapter 3.

Rollable Platforms for Integrated System with Gripper and Flexible Electronics

3.1. Introduction

Electronic devices for diagnosis and therapy [1-3] including mapping brain activity [4,5], cardiac mapping and therapy [6-7], and microsurgery [8,9] have been extensively studied with the development of IoT. Since electronic devices have been installed in curved surfaces such as skin and organs of living body, these approaches necessarily require mechanical flexibility. Furthermore, it is important to have a conformal contact to the target for information acquisition and drug delivery and treatment. In order to conformal contact to target surface, various adhesion methods such as mechanical fixturing hardware, adhesive tapes, and van der Waals forces have been used. [2] However, these methods have limitations in application to organs such as blood vessels in the body where the bending is very severe and the contact area is small. Moreover, these methods limit the precise measurement of elements that detect the degree of deformation in certain standards such as pressure, since it merely serves to attach the device to the target surface. Therefore, developing a device that can be held at a constant force without destroying a target instead of just attaching to surface have

been required. [10] In the field of bio-robotics, various types of soft gripper research have been actively carried out to catch soft objects that have a curved surface. [11-14] However, since the gripper manufacturing process focuses on gripper fabrication that does not destroy the object, it is difficult to simultaneously manufacture and combine with electronic devices that acquires the information of the objects.

Herein, we have developed a rollable platform that can simultaneously fabricate and implement flexible electronics, but also act as a gripper to hold a soft object at a constant force without deforming. To fabricate the rollable platform, we have focused on dynamic control system in nature. In nature, many animals actively control parts of their body in specific shapes with their unique mechanisms for various purpose. For example, some flying bugs utilize their unique folding system to fold their wings at rest and unfold them when flying. [15,16] Elephants and octopus using their nose or legs to grab the objects by rolling. Moreover, butterflies normally have their very long but narrow proboscis rolled, but unroll them when they need to suck nutrients. [17] Inspired by the rolling mechanism of the butterflies' proboscis and rolling functions of the elephants' nose or octopus's legs, we have fabricated the rollable platform which can extremely be rolled and actively unrolled on demand. The rollable platform is composed of several layers of thin and flexible films, which can be applied to existing flexible electronics processes and has excellent durability against bending. On the rollable platform, we have constructed and demonstrated thin film electronics including a heater, strain sensor, temperature sensor and organic light-emitting diodes (OLED), which effectively distribute overall stress on the substrate. Furthermore, we

have demonstrated the rollable platform as a sensor integrated gripper system by using the rolling force as the gripping force to grip micro-objects and to detect tiny motions of an ant. The rollable platform also measure the expansion and compression of an imitated the blood vessel made by circular rubber tube. Finally, we have conducted in vivo pulse wave measurement of swine's blood vessel with the rollable platform by using its advantage of pressure wrapping and detection simultaneously.

3.2. Experimental Methods

3.2.1. Fabrication of rollable platforms and electronics

The rollable electronics were built by stacking two thin Polyimide (PI) films with a Polydimethylsiloxane (PDMS) air channel. Chromium (Cr) layer and Silicon dioxide (SiO_2) layer with thickness of 2 nm respectively were deposited on both sides of the 12.5 μm PI film by a thermal evaporator (Selcos Co., LTD.). The deposition of Cr and SiO_2 enhances the adhesion of the PI film. We fabricated two types of PI film deposited with Cr and SiO_2 layers; First one is the PI film with radius of a 2 mm hole where air can be injected and the other one is the PI film without a hole. The size of the two films is 10 mm in width and 70 mm in length. A spin coater was used to form a 1 μm PDMS film. After curing the PDMS film, we made a rectangular hole of 4 mm in width and 44 mm in length on the film. The prepared PI film without a hole and the PDMS film with the rectangular hole are O_2 plasma treated for plasma bonding (CUTE MPR; Femto Science). After the bonding, the PI film with the hole is plasma bonded on the other side of the PDMS film. To roll the thin film with the air channel, we bonded the thin film on the stretched elastomer and then released the elastomer. We used a silicone rubber (KEG-2000, Shin-Etsu) as the elastomer. The liquid type rubber was hardened at 120 °C of heating and 10 MPa pressing. The thicknesses of the silicone rubber were 40 μm , 70 μm or 100 μm . Before bonding, the silicone rubber was stretched up to 30%, 40% or 50%. The stretched silicone rubber

and the thin PI film with the air channel are plasma bonded. After bonding, we release the silicone rubber to roll the constructed thin film. **(Figure. 3.1)** All the fabrication process of OLED was conducted by a vacuum thermal evaporator. A 100 nm thick Au layer was deposited on a PI film to form an anode. Next, a 50 nm thick hole transport layer of N,N0-Bis(naphtanlen-1-yl)-N,N0-bis(phenyl)-benzidine (NPB), a 50 nm-thick emission layer of tris(8-hydroxy-quinolinato) aluminum (Alq_3) and a 0.5 nm LiF were evaporated sequentially. Finally, a 15 nm thick aluminum layer was deposited to form a semitransparent cathode. **(Figure. 3.2a)** The heater was manufactured through a lift-off process. **(Figure. 3.2b)** The PI film was spin coated with AZ 5124 and then treated at 95 ° C for 1 minute. Thereafter, exposure was performed with aligner for 120 sec and developed for 3 minutes. Then, Cr 3 nm and gold (Au) 100 nm were deposited using a thermal evaporator. The strain / temperature sensor was fabricated with a three-step lift-off process. **(Figure. 3.2c)** The electrode for connecting the sensor was fabricated by using the same method for the heater. To fabricate the strain sensor, lift-off was performed once again and the sensor was connected to the electrode through alignment. The strain sensor was fabricated by depositing Cr 30 nm and Pt 30 nm. Finally, the lift off process was performed to fabricate the temperature sensor, and the alignment was performed as in the case of fabricating the strain sensor. Deposition was carried out with thickness of Cr 3 nm and Pt 30 nm.

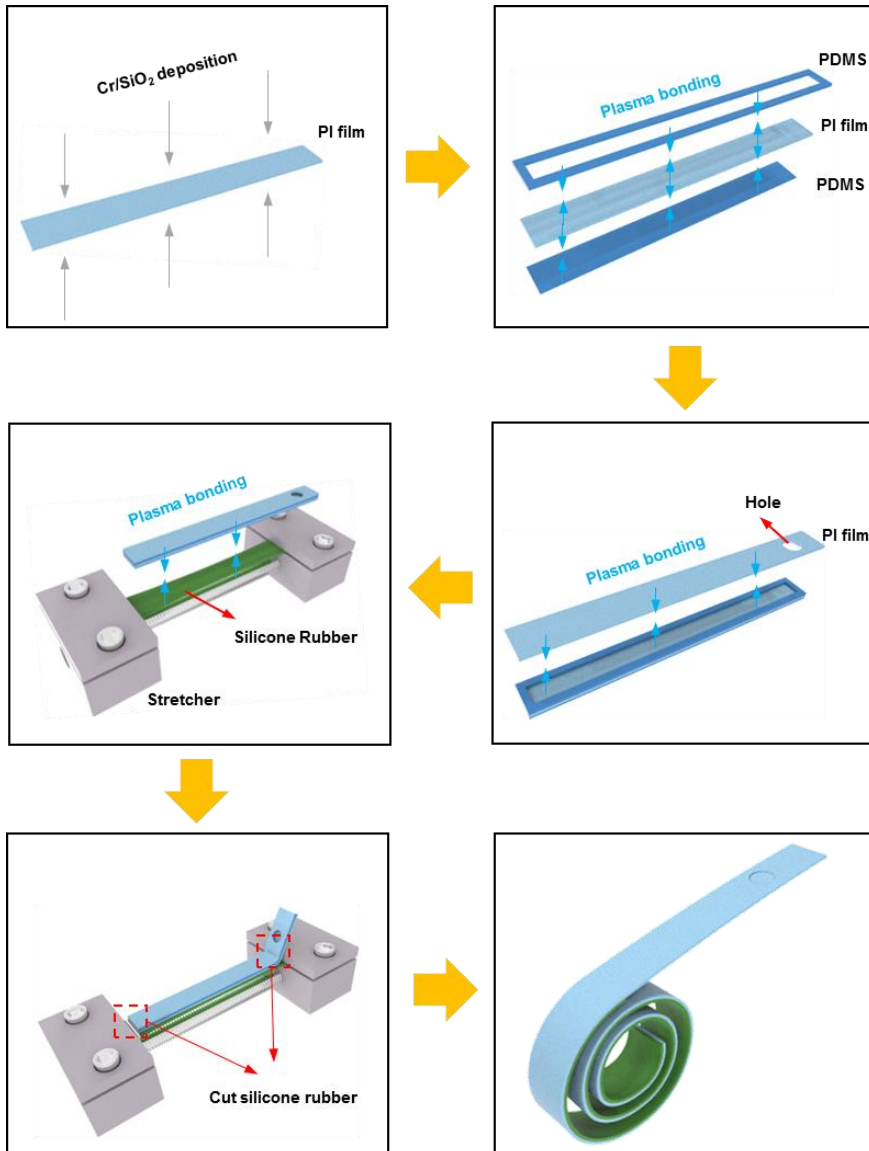


Figure 2.1. Illustration images of the fabrication process of rollable platform.

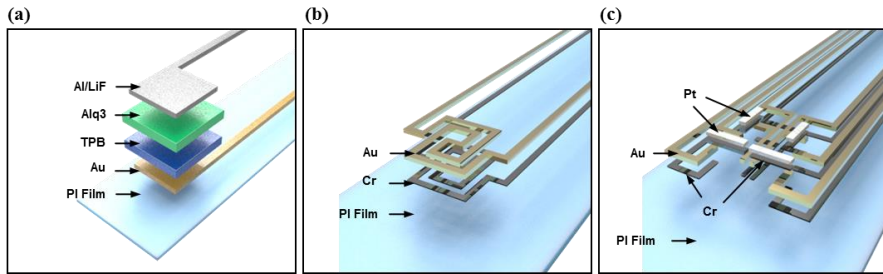


Figure 2.1. Illustration images of fabrication process of organic light emitted diode (OLED), heater, strain and temperature sensor.

3.2.2. FEM and physical analysis

In order for verification, experimental results are compared with the analytical result which is obtained by FE analysis. FE analysis is performed by commercial FE analysis program (ABAQUS). In this analysis, a 4-node doubly curved general-purpose shell (S4) was used, and the total number of elements was 12000. As aforementioned, the rollable sheet consists of PI film, PDMS, and silicone rubber; and each film material is layer-by-layer stacked, as illustrated in **Figure. 3.1**. The rollability of the rollable sheet was achieved through the relaxation process after attaching the uniaxial pre-stretched silicone rubber layer. Thus the rollability is affected by the pre-stretched ratio of the rubber layer. In FE analysis, the mechanical pre-strain was implemented and expressed by the product of artificial thermal coefficient and artificial temperature. In this analysis, it is noted that the implemented pre-strain was logarithm strain corresponding to the pre-strain ratio of the silicone rubber sheet. Additionally, the self-contact condition of the rollable sheet has not been considered for simplification of FE analysis. Magnified optical images were obtained using an optical microscope (Olympus IX70, Japan). Scanning electron microscopy (SEM) images were obtained by using a field emission scanning electron microscope (Carl Zeiss) at an acceleration voltage of 10.0 kV to observe the morphologies of surfaces of the samples.

3.2.3. Swine preparation and pulse wave detecting procedure using rollable platform

The present animal study was approved by the Ethics Committee of Chonnam National University Medical School and Chonnam National University Hospital (CNU IACUC-H-2018-52), and conformed to the Guide for the Care and Use of Laboratory Animals published by the United States National Institutes of Health. (NIH Publication No. 85-23, revised 1996). The study animals were two Yorkshire X Landrace F crossbred castrated male swines weighing 20–25 kg. On procedure day, the swine were anesthetized with zolazepam and tiletamine (2.5 mg/kg; Zoletil50® , Virbac, Caros, France), xylazine (3 mg/kg; Rompun® , Bayer AG, Leverkusen, Germany), and azaperone (6 mg/kg; Stresnil® , Janssen-Cilag, Neuss, Germany). Because zolazepam and tiletamine are weak muscle relaxants, xylazine was added. Azaperone was used to extend anesthesia. The animals received supplemental oxygen via endotracheal intubation throughout the procedure by isoflurane inhalation (2%). Anesthetic depth was clinically monitored by cessation of movement, eye position, loss of muscular tone, and absence of palpebral and pedal reflexes. [18,19]

The right and left superficial femoral arteries exposed surgically after a subcutaneous injection of 2% lidocaine. A 4 Fr sheath was inserted in the right superficial femoral artery, and the aortic pressure and wave were continuously recorded with RadiAnalyzer TM (Abbott Vascular, Santa Clara, CA, USA). Continuous hemodynamic and surface electrocardiographic monitoring was performed throughout the procedure. [20] Simultaneously,

rollable sensor was attached in the left superficial femoral artery for recording pulse wave. To evaluate pulse wave consistency in variable situations, recordings also done after epinephrine injection for elevating cardiac output and potassium chloride injection via artery sheath for euthanize.

3.2.4. Fabrication of cell sheet implanted platform and Cell sheet transfer procedure

The C2C12 myoblasts were cultured with a seeding density of 5.0×10^6 cells cm^{-2} using general culture medium (Dulbecco's modified Eagles media, 10% fetal bovine serum and 1% penicillin-streptomycin) for 3 days under 5% CO_2 and 37 °C conditions. The cultured C2C12 myoblasts were gently detached using trypsin/EDTA (Gibco, NY, USA) for 5 min, and then centrifuged at 2000 rpm during 3 min. The supernatant were suctioned and re-suspended with culture medium supplemented with 25 mg/mL fibrinogen (Sigma-Aldrich) in HBSS solution (Hank's Balanced Salt Solution, Gibco, NY, USA) of 100 μL . After then, the re-suspended cells with fibrinogen were cultured with a seeding density 2.0×10^5 cells/ cm^2 on 12 well culture plate for 1 day. The cell sheets were detached from culture plate by gently shaking and transferred on rollable platform that were coated with 2% gelatin solution. To confirm the cell sheet on rollable platform, cell sheets were stained F-actin. The cell sheet on rollable platform was fixed with 4%

paraformaldehyde (PFA) for 15 min at room temperature and gently washed 3 times with phosphate buffered saline (PBS). Fixed cell sheets of implanted rollable platform were embedded on optimal cutting temperature (OCT) compound (SAKURA Finetek USA Inc, CA, USA) and sectioned at thickness of 100 μm by a cryocut microtome (CM3050 S, Leica, Nussloch, Germany). The sectioned samples were washed with PBS and immersed in 0.2% Triton X-100 solution for 10 min. The immersed samples were then treated with 5% bovine serum albumin solution (Sigma-Aldrich) to block the non-specific binding of antibodies at room temperature for 1 hr. The blocked samples were incubated with primary mouse specific antibodies, which were diluted for F-actin (1:40, Alexa 488-conjugated phalloidin, Invitrogen) at room temperature for 40 min. After then, the samples were washed gently 3 times with PBS and counter-stained with 4',6-diamidino-2-phenylindole (DAPI). Stained samples were observed using a fluorescence microscope (Eclipse Ts2R, Nikon, Tokyo, Japan). For confirming cell damage between rollable platform and rolling, cell sheet on rollable platform was carried out live & dead assay. Cell sheets of implanted rollable platforms with folding and spreading 0 or 5 time were incubated with PBS supplemented with 2 μM calcein acetoxymethyl ester (calcein AM, Invitrogen, USA) and 4 μM ethidium homodimer (EthM-1) working solution for 30 min under 5% CO_2 and 37 $^\circ\text{C}$ conditions. Stained samples were observed under a confocal microscope (Carl Zeiss LSM 700, Oberkochen, Germany). To tracking the implanted cell sheet, the cytoplasmic membranes of cells were pre-labeled

with a fluorescent cell tracker, 3,3'-diiodo-4',4'-diiodo-5,6-dimethyl-1,2-dioxetane perchlorate (DiO; Invitrogen, Carlsbad, CA, USA). DiO dye (6.25 mg/mL) was incubated with cells for 1 hr before preparation of cell sheet. Female ICR mice (6 weeks old, Dayun, Gyeonggi-do, Korea) were anesthetized with ketamine and rompun (100 μ L; rompun:ketamine, 1:4). Skin of hind limb was incised and cell sheet of implanted rollable platform was attached at the surface of hind limb muscle. After 1 min, gelatin was melted by mouse body temperature and rollable platform was gently removed. After 1 day, all mice were sacrificed and their whole hind limb muscle tissues were retrieved for histological analysis. This animal study protocol (DKU-17-027) was approved by the Institutional Animal Care and Use Committee of Dankook University. Extracted hind limbs were removed bone and fixed with 4% paraformaldehyde in 4 °C for overnight. The fixed samples were embedded in OCT compound, sectioned at 16 μ m by a cryocut microtome. Sectioned samples were washed OCT compound with PBS and observed under fluorescence microscope. The other sectioned specimens were stained with haematoxylin and eosin (H&E) and observed under optical microscope (Eclipse Ts2R, Nikon, Tokyo, Japan).

3.3. Results and Discussion

3.3.1. Device structure and characteristics of rollable platform

Figure. 3.3a shows the schematic illustration of how Lepidoptera gets fed from flowers in nature. They normally have their very long but narrow proboscis rolled, but unroll them to take nutrients [21]. Even though the opening of a flower is narrow and the target nutrients are located deep inside of the flower, Lepidoptera can make their proboscis easily reach food sources. The rolling and unrolling movements of a Lepidoptera's proboscis are conducted through a hydraulic drive system that uses elastic parts and musculature [17, 22, 23]. The rolling of the proboscis is driven by its elasticity and the pressure that is decreased inside its channel. On the other hand, the proboscis gets unrolled as the pressure increases inside and the muscle contracts. Inspired by the Lepidoptera's rolling and unrolling behavior, we have developed a rollable platform that consist of two main parts: a channel system and an elastomeric substrate. The former is composed of multi-layers including polydimethylsiloxane (PDMS) and polyimide (PI) films. These films have been stacked and bonded via plasma bonding alternately as shown in **Figure. 3.3b**. The PDMS layer with thickness of approximately 1 μm is located between the PI films. Therefore, there is a small void space into which air can be injected, which part is for unrolling the device from its rolling state. The latter part is a silicone rubber substrate, which is initially stretched and bonded to the surface of the PI film. This

layer is responsible for rolling the platform as illustrated in the inset of **Figure. 3.3b**. If the pre-stretched silicone rubber is bonded to the PI film and then is released, it shrinks and generates a bending moment on the entire film. The generated moment causes the entire film to be rolled to a specific radius, depending on the degree of the pre-strain. Thus, the rollable platform basically maintains the rolled state. The mechanism of unrolling behavior of the rollable platform is driven from pneumatic pressure. The detailed manufacturing process of the rollable platform is described in the Experimental and method section, and **Figure. 3.1**. The platform is capable of being stretched by injecting air through the air channels between the PI films. This is because the pressure of the injected air keeps the channels in a swollen form (**Figure. 3.3b**). By using this mechanism, the device can be rolled and unrolled repeatedly and actively, according to the circumstances.

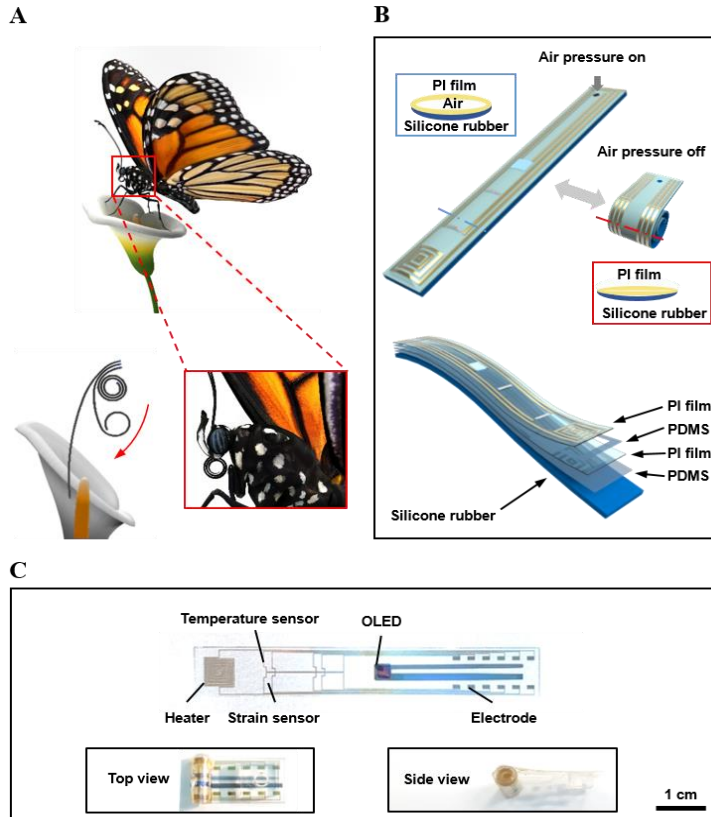


Figure 3.3. (a) A schematic illustration of how a butterfly gets fed from a flower. It unrolls its proboscis, which is normally kept coiled, in order to go through the flower. (b) The composition of the rollable electronic device. On the silicone rubber, the PDMS layers and PI films are stacked alternately as shown (up). When air is injected into the space between the polyimide films, the device is swollen and unrolled. (c) The composition of the electronic devices on the top PI film. They are constructed in the order of: heater, strain sensor, OLED and electrode from left to right. Photos of rolled state from the top (left inset) and side views (right inset)

3.3.2. Rollability analysis of rollable platform

As the rollability of the platform is physically affected by the stress of the silicone rubber, its strain and thickness are varied in order to investigate the effect of the stress. The strain is defined as the change in length after stretching divided by the original length ($\varepsilon = \Delta L/L$). The inner diameter of the rollable platform is used as the index of its rollability as shown in **Figure. 3.4a**. **Figure. 3.4b** shows the photographic images of the device in side view with variations of applied strains (30%, 40% and 50%) and thickness (40 μm , 70 μm and 100 μm) of the silicone rubber. As expected, the inner diameter of the film almost linearly decreases as the applied strain increases due to the elevated recovery force of the elastic film. As the film thickness increases, the curvature increases due to the increased contraction force of the layer. Especially, in the case of applied strain of 50% and thickness of 100 μm , the inner diameter of the device was ~ 2 mm. In this case as observed from above, the area of the film in the rolled state is reduced to 1/25 compared to that of the unrolled state. To verify the tendency of rollability with variation of strain and thickness of the silicone rubber layer, we have conducted Finite Element Method (FEM) simulation study via ABACUS program. The results acquired through the relaxation process after attaching the uniaxial pre-stretched silicone rubber layer. A detailed method of the simulation is shown in the Materials and Methods section in this paper. The experimental and simulation data are in good agreement as shown in **Figure. 3.4c**. **Figure. 3.4d** shows that the platform is rolled to a very small size in time order. The platform starts to be rolled from one end of the film and turns round at 500

ms, showing a gradual decrease while the final shape appears at 2 s. The rolling process progress until the restoring stress of the silicone rubber and flexural strength of the PI film reach equilibrium. Movie clips in the Materials and Methods show the whole rolling process. In **Figure. 3.4e**, the captured images of FEM with variations of applied strains for the 70 μm -thick silicone rubber show that the inner diameter of the rolled film decreases as the strain of the silicone rubber film increases. And as shown in **Figure. 3.5**, which presents the von-mises stress of the silicone rubber in all cases, the inner diameter of the rollable platform decreases as the pre-strain increases.

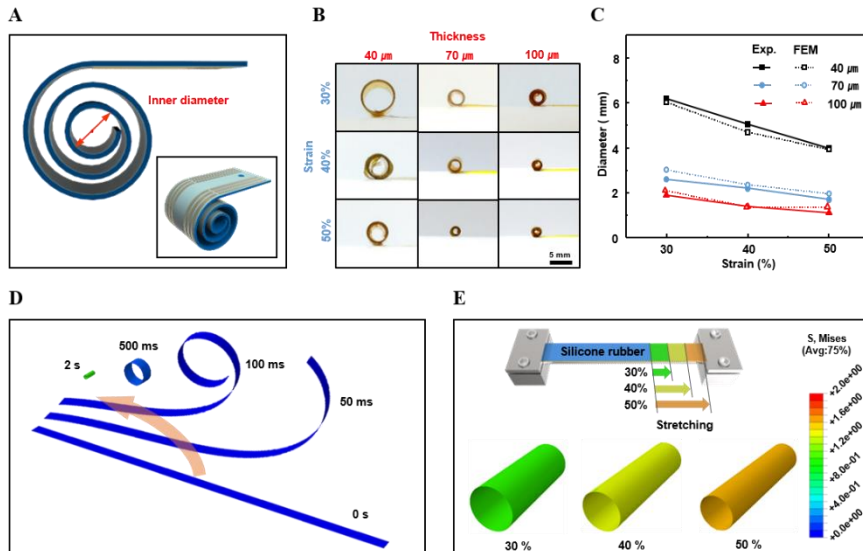


Figure 3.4. (a) An illustration of the rollable device that shows the extent of its rollability, which is determined by the inner diameter. (b) Photographic images of the devices in the side view with variations of applied strains (30%, 40% and 50%) and thickness (40 μm , 70 μm and 100 μm) of the silicone rubber. (c) The measurements of the inner diameter of the rollable device with variations of applied strains and thickness of the silicone rubber. (d) Captured images of FEM simulation of the rolling process with time dependent at 30 % applied strain and 70 μm thickness silicone rubber. (e) FEM results of the applied stresses on the 70 μm silicone rubber at variation of applied strains

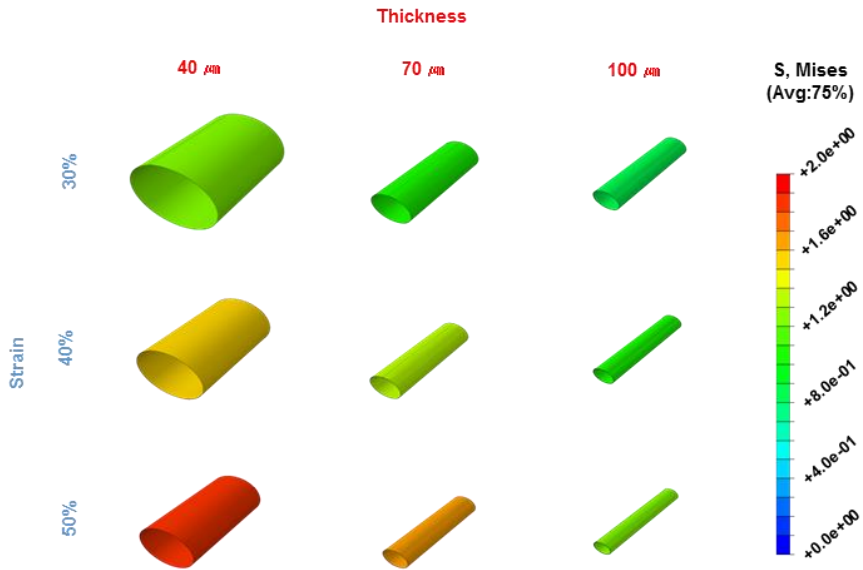


Figure 3.5. FEM results of the residual stresses of the silicone rubber with variations of applied strains (30%, 40% and 50%) and thickness (40 μm, 70 μm and 100 μm) of silicone rubber

3.3.3. Operation of various electronics on rollable platform

Based on the fundamental study of the mechanism, we have constructed a rollable electronic system that can be actively controlled. The rollable platform is rolled into a confined space when not in use (inset of **Figure. 3.3c**), while it is unrolled when necessary. **Figure. 3.3c** presents a photographic image of several electronic devices on the rollable platform in its unrolled state. The devices shown here consist of five independent functional components: heater, temperature sensor, crack-based strain sensor, OLED [24], and electrode in order from left to right. A detailed description of the operation of each constructed electronics is given in **Figure. 3.6**. We have investigated the feasibility of the each electronic part when it is rolled and unrolled. The detailed manufacturing process of electronics is described in the Experimental method section, and **Figure. 3.2**. **Figure. 3.6a** shows photographic images of the heater, with 5 V applied by voltage source. The heater was designed in the shape of a maze pathway with thin and narrow electrode. The applied current induced heat and then the temperature of the heater was ~ 35 °C. As shown **Figure. 3.6a**, the heater was normally operated even in the rolled state, showing comparable temperature distribution in the unrolled state. **Figure. 3.6b** shows that the OLED on the PI film was also normally operated. Generally, operating the OLED is difficult in the folded state of extremely high curvature due to delamination between the metal layers which induces failure of junction or electrode. In our platform which distributes residual stress uniformly based on the result of the simulation study, the OLED was normally operated without the failures even in the

rolled state [25]. The temperature sensor, in **Figure. 3.6c**, composed of a platinum resistor exhibits linear response with a variation of temperature from 25 °C to 45 °C in both of rolled and unrolled states (**Figure. 3.7a**). The response times in both states were analogous with those of the unrolled state (**Figure. 3.7b**). **Figure. 3.6c** shows the change of resistance of a crack-based sensor between the applied strain of 0-2 % repeatedly [26, 27]. The resistance of the sensor in the rolled state increases compared to that in the unrolled state due to the gradual disconnection of nano-scale crack junctions (**Figure. 3.7d**). As the rolling progress, the curvature of the device increases, which increases the resistance of the sensor. Based on the results, the strain crack sensor on the rollable platform can be applied to the measurement of the curvature of circular target structures.

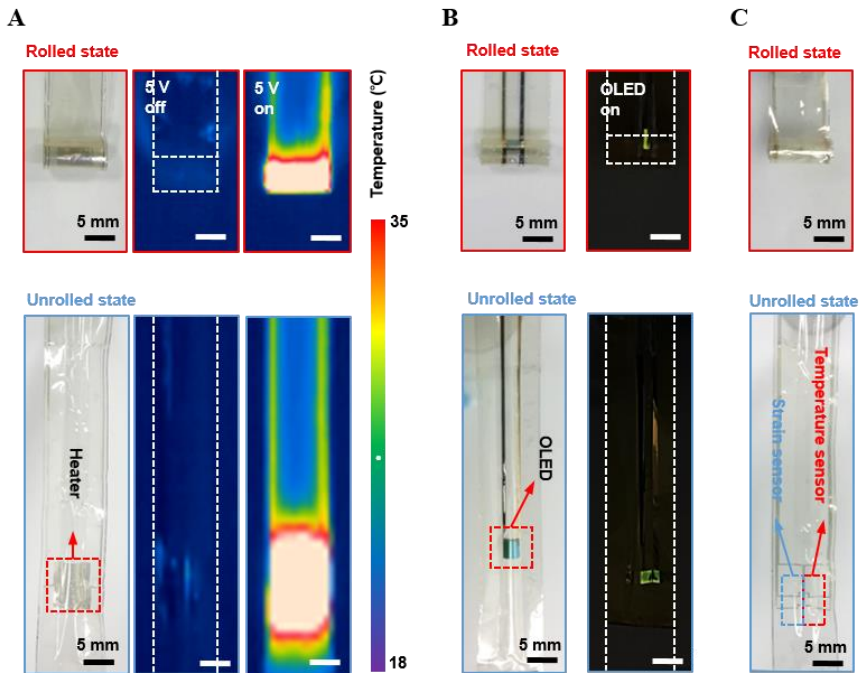


Figure 3.6. (a) Photographic images and thermal images of the heater in its unrolled and rolled states. Thermal images of the heater show the temperature distribution when currents are applied. (b) Photographic images of the OLED in its unrolled and rolled states with currents applied. (c) Photographic images of the temperature and strain sensor in its unrolled and rolled states.

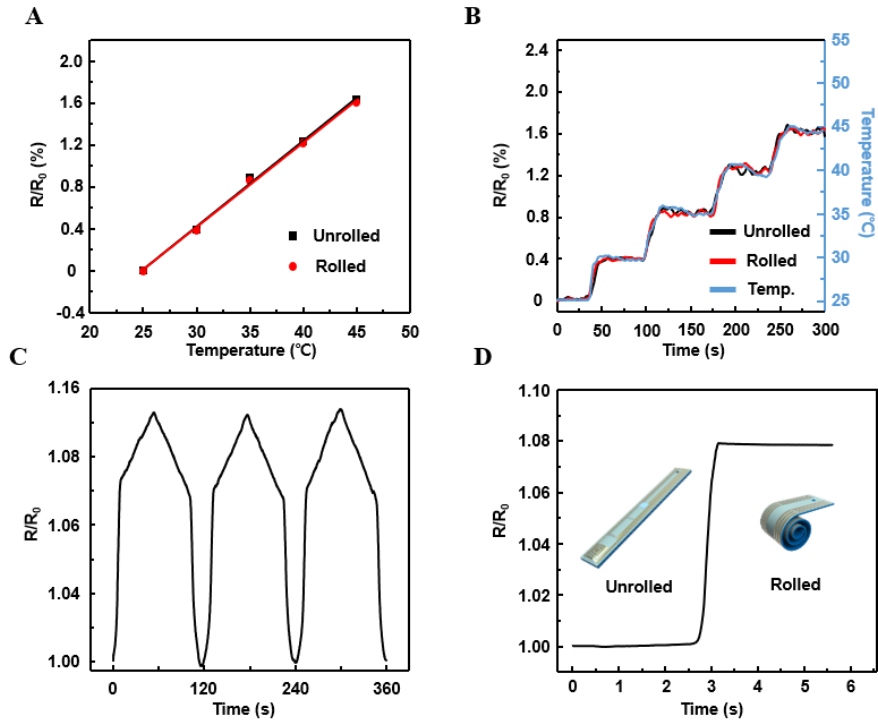


Figure 3.7. (a, b) Measurements of resistance change of the temperature sensor with variation of temperature in its rolled and unrolled states. (c) The graph of normalized resistance variance versus strain of 2%. (d) Measurements of resistance change of the strain sensor in its rolled and unrolled states

3.3.4. Theoretical modeling of material fracture

To elucidate operability of an electronic device on the rollable platform, we have analyzed theoretically why the device is operated without destruction even in the curved and rolled states as shown in **Figure. 3.8** [28, 29]. The dimension of the thickness (z) of the piled films is small enough compared to in-plane (x - y) and the curvature of bending. Hence, it is assumed that the magnitude of the strain is proportional to the thickness of the piled films. The bending strain ε_x according to the thickness direction (z) are given as follows at any arbitrary height.

$$\varepsilon_x = \varepsilon_{bottom} + \frac{z}{h} (\varepsilon_{top} - \varepsilon_{bottom}), \quad h = d_1 + d_2 \quad (S1)$$

where ε_{bottom} and ε_{top} indicate the bending strain at the bottom and top surfaces, respectively. d_1 and d_2 represent the thickness of the PI film and the silicone rubber film, and h indicates the total thickness of the film. In this analysis, the volume of the PDMS film and the air channel is not considered because the thickness is small enough to be ignored. The stress at each layer is written as follows:

$$\sigma_1 = \overline{E}_1 \left[\varepsilon_{bottom} + \frac{z}{h} (\varepsilon_{top} - \varepsilon_{bottom}) \right], (d_2 \leq z \leq h) \quad (S2)$$

$$\sigma_2 = \overline{E}_2 \left[\varepsilon_{bottom} + \frac{z}{h} (\varepsilon_{top} - \varepsilon_{bottom}) \right], (0 \leq z \leq d_2) \quad (S3)$$

$$\overline{E}_1 = \frac{E_1}{1-\nu_1^2}, \quad \overline{E}_2 = \frac{E_2}{1-\nu_2^2} \quad (S4)$$

where E indicates elasticity modulus and ν poisson's ratio. The strain

at the bottom and top surfaces of the piled films at a bending moment can be expressed as follows:

$$\varepsilon_{top} = \frac{d_2^2 \bar{E}_2 + d_1^2 \bar{E}_1 + 2d_1 d_2 \bar{E}_2}{2R(d_2 \bar{E}_2 + d_1 \bar{E}_1)} \quad (S5)$$

$$\varepsilon_{bottom} = -\frac{d_2^2 \bar{E}_2 + d_1^2 \bar{E}_1 + 2d_1 d_2 \bar{E}_1}{2R(d_2 \bar{E}_2 + d_1 \bar{E}_1)} \quad (S6)$$

where R indicates the radius of curvature. The corresponding mechanical properties of the rollable platform are as shown in **Table 3.1**. The rollable platform with various electronics was manufactured by applying 30 % pre-strain to the silicone rubber film. By substituting the above values into the (S5), ε_{top} is obtained. Therefore, the tensile strain on electronics for the rollable platform with a bending radius of 1.3 mm is 0.99%, which is less than the material's facture point [30, 31]. This study indicates that the electronics on the rollable platform operate normally without destruction even in the rolled state in our experiments.

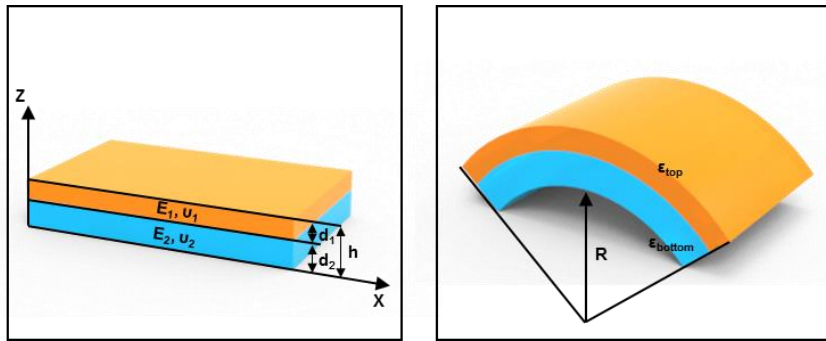


Figure 3.8. Illustrations of simplified model for analyzing rollable system.

Material	Elasticity modulus (MPa)	Poisson's ratio	Thickness (μm)
PI film	2500	0.3	12.5
Silicone rubber film	6.34	0.5	70

Table 3.1 Material properties and film thickness of rollable platform

3.3.5. Actuating and detecting with rollable platform

In the rollable electronic device, specific rolling force of the substrate work as gripping force for target objects, which means that the device can be integrated into soft grippers for micro-objects. On the basis, we have demonstrated the rollable soft-gripper mounted with crack sensors that can recognize minute movements or vibration of an insect. Generally, when a rigid gripper grasps micro bio-objects such as insects with its strong force, it may cause some serious damage to the objects [32-34]. With the rollable platform with its soft polymeric materials, we can achieve non-damaging manipulations of the micro bio-objects. **Figure. 3.9a** shows that an ant is well grabbed with the rollable soft-gripper. To grab the ant, we unroll the platform by applying air pressure and then remove the pressure to wrap and hold the ant. After grabbing the ant with the gripper, we have successfully measured the resistance variation of the crack sensor, which is induced by the tiny movement of the grabbed ant. The results imply that our rollable electronic device can be successfully applied not only to a soft gripper for manipulating micro bio-objects but also to a device that detects their tiny motions and vibration. And we have also measured the extent of expansion of a phantom blood vessel with the crack sensor mounted on the rollable platform. The platform can make conformal contact onto the phantom blood vessel, and contraction and expansion of the vessel was well measured, as shown in **Figure. 3.9b**. The diameter of the phantom blood vessel was 5.7 mm before deformation and 6.1 mm after deformation induced by air pressure into the vessel. The resistance of the sensor changed stably and

repeatedly when we apply and remove the air pressure for five times. This result implies that our device could be extensively applied to the bio-medical research especially on precise measurement of blood pressure and pulse wave velocity, or direct contact-based drug delivery [35-38].

To demonstrate biomedical applications of the rollable platform, we have conducted pulse wave measurement with rollable platform by wrapping superficial femoral artery of swine as rolled state. **Figure. 3.10a** shows the illustrations of experiment setup to detecting the pulse wave of swine. For the experiment, both the swine's left and right superficial femoral artery were opened to detect the pulse wave by using the invasive blood pressure (IBP) sensor and the rollable platform. (**Figure. 3.10b**). The conventional pulse wave measuring device, IBP sensor, was used as reference signal. In general, to detect the pulse wave, the artery of swine should be incised for inserting IBP sensors. Moreover, IBP sensors need to additional equipment such as pressure bag, pressure transducer and system for electrically convert the signals for acquiring data. However, our rollable platform could detect the signals by just wrapping the artery without incising the artery and didn't need any other additional equipment except data acquiring system. To verify the effectiveness of rollable platform in detecting the pulse wave of swine, the signals were compared with the IBP sensor measurement data when the rollable platform was gripped the entire cylindrical artery (rolled state) and when the platform was just passively contacted to the surface of artery without rolling (unrolled state). (**Figure. 3.10c and d**) **Figure. 3.11a and b** show that measurement results of pulse wave according to the different detecting method. The results show that the rollable platform in the rolled

state have significant difference in the pulse wave detecting performance compared to the unrolled state. In the rolled state, the measured signals are almost same when compared to the signal measured by the IBP sensor. Moreover, it also detects the dicrotic notch signals as shown in **Figure. 3.11a**. In contrast, in the unrolled state, the measured signals are weak and unclear. (**Figure. 3.11b**) This is because, in the rolled state, the pulse wave can be measured with the artery gripped well and the platform is fixed to the artery without slip. On the other hand, in the unrolled state, the platform is not in contact constantly with the artery and couldn't grip the artery under the proper pressure making it hard to detect the clear pulse wave. Furthermore, to verify the detecting ability of our devices in various situations, we checked the pulse wave responses of the two situations (epinephrine and potassium chloride (KCl) injection) and compared them with the signals of conventional IBP sensor. (**Figure. 3.11c and d**) It is well known that epinephrine accelerates heart rate and KCl solution counteracts. As the same terms of normal condition, the rollable platform could detect well under the abnormal condition. The findings from in vitro and in vivo study is valuable in that it proves the feasibility of the biomedical device or its instrument design that is cost-effective, scalable, and reproducible, which can be utilized for easy application in clinical studies.

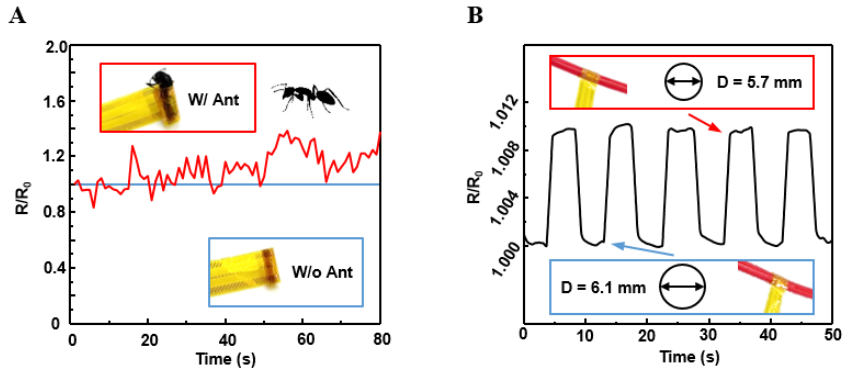


Figure 3.9. (a) Measurements of resistance change of the strain sensor with and without an ant (b) Measurements of resistance change of the strain sensor with variation of the diameter of 6.1 mm to 5.7 mm

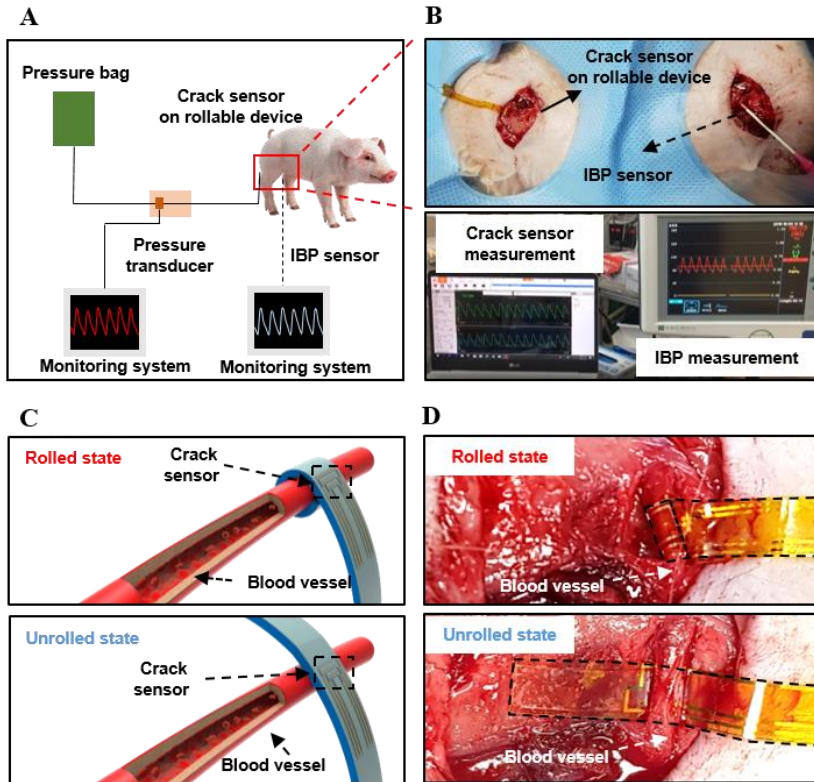


Figure 3.10 (a) Schematic Illustration of two types of systems for the pulse wave detecting. (b) Photographic images of the implanted sensors on swine's blood vessels and monitoring systems. (c) Schematic Illustration images and (d) photographic images of the rollable device, which wraps and unwraps around a blood vessel.

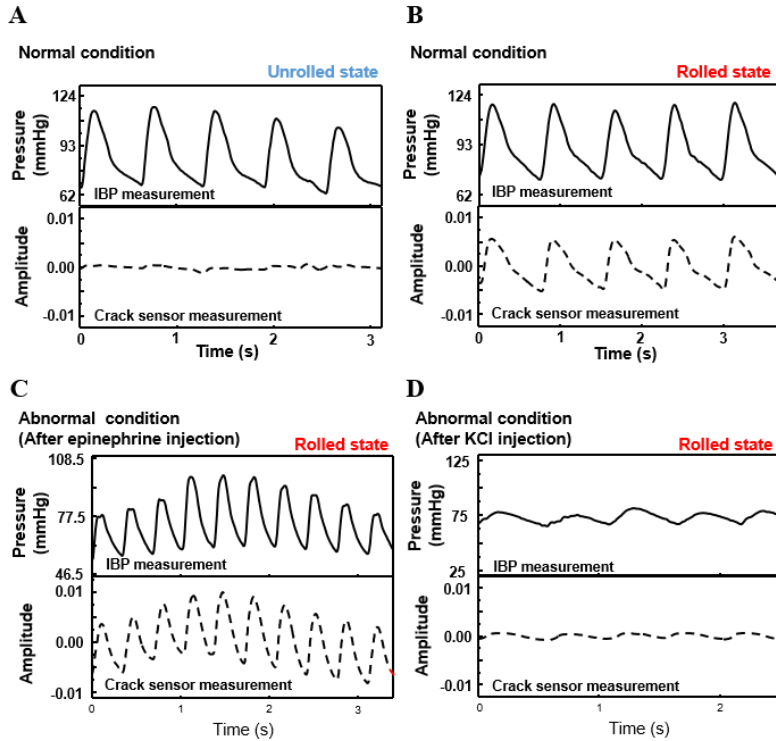


Figure 3.11 Pulse waves of swine's blood vessels using conventional IBP sensor and our device in its (a) unrolled and (b) rolled states at normal condition. Pulse waves of swine's blood vessels at abnormal condition (c) after epinephrine injection and (d) after KCl injection

3.3.6. Cell sheet transfer using rollable platform

We have applied the rollable device to surgery process with minimum invasion by having narrow skin incision and approaching the target tissue in its rolled state and providing treatments to the tissue in its unrolled state such as in drug delivery or cell sheet transplantation. As shown in the time lapse photos of **Figure. 3.12**, which present the virtual passing process of the devices, the platform is rolled up and going through a narrow acrylic tube and unrolled by injecting air when it reaches the target. To demonstrate biomedical applications of the rollable platform, we have conducted cell sheet transfer to a hind limb muscle of a mouse. When it comes to cell sheet transfer, if a fresh cell sheet is attached to a damaged tissue, the transferred cells autonomously would recover the damaged tissue as generally known [39-41]. However, in general, to achieve large area tissue transfer, the large area of a skin layer should be incised [4]. To avoid the serious damage to other tissues by large-scale skin incision, the area to be incised should be minimized. Hence, we have conducted a feasibility test for cell sheet transfer with the rollable device to a mouse on its hind limb muscle with a minimized incision of the skin. The cell sheets that were cultured to use C2C12 myoblasts with fibrin for 1 day are transferred on the rollable platform that has been coated with 2% gelatin solution which serves as an adhesive between the rollable platform and the cell sheet (**Figure. 3.13a**). The cell sheet attached on the rolled platform rolls along with the platform as shown in **Figure. 3.13b**. To confirm the in vitro cell viability against the rolling, we have repeated the rolling and unrolling process for five times and then

checked the viability of the cells. **Figure. 3.13c** shows that the cells remain alive even after getting mechanical stress from the rolling. Then, we have conducted in vivo animal test with a mouse. As shown in **Figure. 3.13d**, the cell sheet is successfully transferred. The constructed cell sheet on the rollable platform goes into the incised area of the mouse skin and penetrated until it reaches the target area. Then, the cell sheet on the rollable platform is transferred to the target area through its contact on the target tissue for 1 min. One day after the treatment, we have observed if the cell sheet has well been transferred to the target area by using fluorescence and histological analysis (**Figure. 3.13e**). The finding from in vitro and in vivo study is valuable in that it proves the feasibility of the biomedical device or its instrument design that is cost-effective, scalable, and reproducible, which can be utilized for easy application in clinical studies. The rollable platform could also be utilized to differentiate cultured stem cells with the proposed rolling and unrolling mechanism while simultaneously measuring their physiological properties which can be done in further studies.

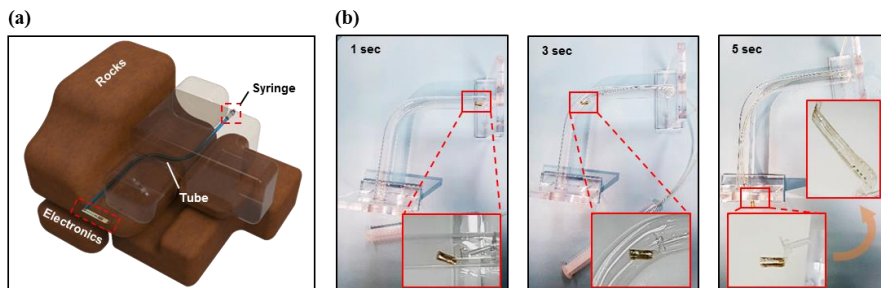


Figure 3.12 The movements of the rollable device through the narrow, curved acrylic tube

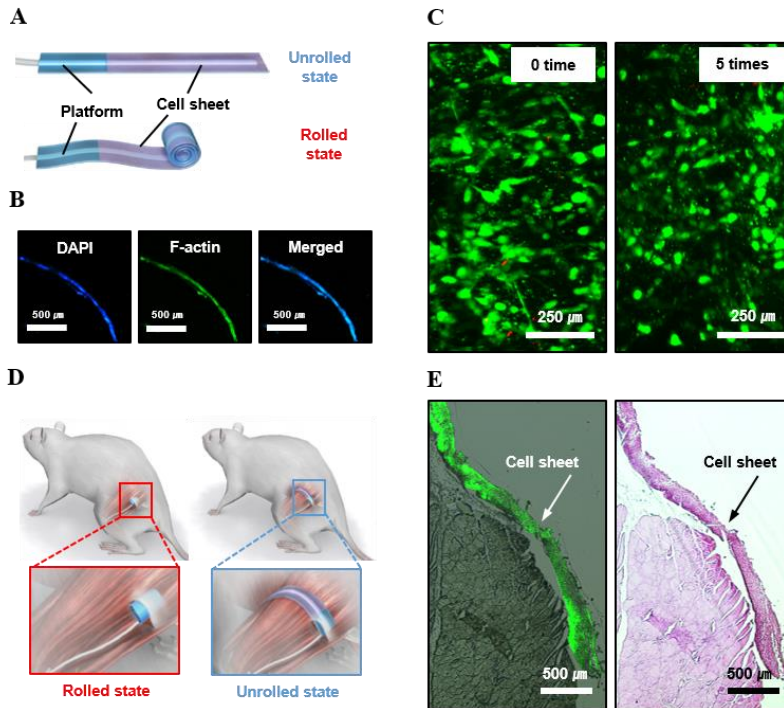


Figure 3.11 (a) Illustration images of the rollable platform with the cell sheet attached, in its unrolled and rolled states. (b) The cross section fluorescence microscope images of stained cell sheet by 4',6-diamidino-2-phenylindole (DAPI), F-actin and merged on the rolled platform. (c) The confocal microscope images of live & dead assay for stained cell sheet on the rollable platform before rolling and after 5 times of rolling. (d) Illustration images of cell sheet transplantation method operated to a mouse. The rollable platform with a cell sheet is inserted into the mouse with minimal damage and spread out after insertion. (e) Fluorescence microscope image of sectioned hind limbs muscle with transplanted cell sheet (left) and its optical microscope image stained by haematoxylin and eosin (H&E) (right)

3.4. Conclusion

We have developed a rollable platform composed of polymeric multilayers of PDMS, PI, and silicone rubber inspired by the behavior of animal's hand. The pre-stretched silicone rubber bonded to the PI film induces the rolling of the platform, and injecting air into the void space between the adjacent PI films unrolls the platform from its rolling state. This rolling mechanism offers the uniform stress distribution on the substrate, which can avoid the failure of the electric connection of the device with the highly concentrated stress at the folded edge. The extent of rolling can be controlled by varying the thickness of the elastomeric film and applied strain to the film. This result has been confirmed by conducting experiments and FEM simulation study. On the rollable platform, we have constructed thin film electronics including heater, strain sensor, temperature sensor, and OLED, which work normally in the rolled and unrolled states. The integrated system could grip micro bio-objects and demonstrated the detection of tiny motions of the objects. Furthermore, we have successfully conducted in vivo animal test of measurement of pulse at swine's superficial femoral artery with the gripping electronics. Finally, we have successfully conducted in vivo animal test of cell sheet transfer to the damaged hind limb tissue of a mouse with the rollable platform. With the advantages of our rollable platform, we believe that it can be applied to broad research fields including biomedical electronic system in the near future.

3.5. References

- [1] S. Vaddiraju, I. Tomazos, D. J. Burgess, F. C. Jain, F. Papadimitrakopoulos, "Emerging synergy between nanotechnology and implantable biosensors: a review". *Biosens. Bioelectron.* **25**, 1553-1565 (2010).
- [2] D.-H. Kim, N. Lu, R. Ma, Y.-S. Kim, R.-H. Kim, S. Wang, J. Wu, S. M. Won, H. Tao, A. Islam, "Epidermal electronics". *Science* **333**, 838-843 (2011).
- [3] T. Someya, T. Sekitani, S. Iba, Y. Kato, H. Kawaguchi, T. Sakurai, "A large-area, flexible pressure sensor matrix with organic field-effect transistors for artificial skin applications". *Proc. Natl. Acad. Sci. U. S. A.* **101**, 9966-9970 (2004).
- [4] J. Viventi, D.-H. Kim, L. Vigeland, E. S. Frechette, J. A. Blanco, Y.-S. Kim, A. E. Avrin, V. R. Tiruvadi, S.-W. Hwang, A. C. Vanleer, "Flexible, foldable, actively multiplexed, high-density electrode array for mapping brain activity in vivo". *Nat. Neurosci.* **14**, 1599 (2011).
- [5] A. P. Alivisatos, A. M. Andrews, E. S. Boyden, M. Chun, G. M. Church, K. Deisseroth, J. P. Donoghue, S. E. Fraser, J. Lippincott-Schwartz, L. L. Looger, "Nanotools for neuroscience and brain activity mapping". *ACS Nano* **7**, 1850-1866 (2013).
- [6] D.-H. Kim, R. Ghaffari, N. Lu, S. Wang, S. P. Lee, H. Keum, R. D'Angelo, L. Klinker, Y. Su, C. Lu, "Electronic sensor and actuator

- webs for large-area complex geometry cardiac mapping and therapy". *Proc. Natl. Acad. Sci. U. S. A.* **109**, 19910-19915 (2012).
- [7] D.-H. Kim, N. Lu, R. Ghaffari, Y.-S. Kim, S. P. Lee, L. Xu, J. Wu, R.-H. Kim, J. Song, Z. Liu, "Materials for multifunctional balloon catheters with capabilities in cardiac electrophysiological mapping and ablation therapy". *Nat. Mater.* **10**, 316 (2011).
- [8] M. Cianchetti, C. Laschi, A. Menciassi, P. Dario, "Biomedical applications of soft robotics". *Nat. Rev. Mater.*, 1 (2018).
- [9] E. T. Roche, M. A. Horvath, I. Wamala, A. Alazmani, S.-E. Song, W. Whyte, Z. Machaidze, C. J. Payne, J. C. Weaver, G. Fishbein, "Soft robotic sleeve supports heart function". *Sci. Transl. Med.* **9**, eaaf3925 (2017).
- [10] A. M. Nasab, A. Sabzehzar, M. Tatari, C. Majidi, W. Shan, "A Soft Gripper with Rigidity Tunable Elastomer Strips as Ligaments". *Soft robotics* **4**, 411-420 (2017).
- [11] K. C. Galloway, K. P. Becker, B. Phillips, J. Kirby, S. Licht, D. Tchernov, R. J. Wood, D. F. Gruber, "Soft robotic grippers for biological sampling on deep reefs". *Soft robotics* **3**, 23-33 (2016).
- [12] L. Al Abeach, S. Nefti-Meziani, T. Theodoridis, S. Davis, "A variable stiffness soft gripper using granular jamming and biologically inspired pneumatic muscles". *Journal of Bionic Engineering* **15**, 236-246 (2018).
- [13] J. Shintake, S. Rosset, B. Schubert, D. Floreano, H. Shea, "Versatile soft grippers with intrinsic electroadhesion based on multifunctional polymer actuators". *Adv. Mater.* **28**, 231-238 (2016).

- [14] P. Polygerinos, N. Correll, S. A. Morin, B. Mosadegh, C. D. Onal, K. Petersen, M. Cianchetti, M. T. Tolley, R. F. Shepherd, "Soft robotics: Review of fluid-driven intrinsically soft devices; manufacturing, sensing, control, and applications in human-robot interaction". *Advanced Engineering Materials* **19**, 1700016 (2017).
- [15] J. A. Faber, A. F. Arrieta, A. R. Studart, "Bioinspired spring origami". *Science* **359**, 1386-1391 (2018).
- [16] K. Saito, S. Nomura, S. Yamamoto, R. Niyama, Y. Okabe, "Investigation of hindwing folding in ladybird beetles by artificial elytron transplantation and microcomputed tomography". *Proc. Natl. Acad. Sci. U. S. A.* **114**, 5624-5628 (2017).
- [17] X. Zhou, S. Zhang, "Manipulate the coiling and uncoiling movements of Lepidoptera proboscis by its conformation optimizing". *arXiv preprint arXiv:1311.1555*, (2013).
- [18] L. Badimon, "Protective Effects of Ticagrelor on Myocardial Injury After Infarction".
- [19] H. K. Kim, M. H. Jeong, K. S. Lim, J. H. Kim, H. C. Lim, M. C. Kim, Y. J. Hong, S. S. Kim, K.-H. Park, K.-S. Chang, "Effects of ticagrelor on neointimal hyperplasia and endothelial function, compared with clopidogrel and prasugrel, in a porcine coronary stent restenosis model". *International journal of cardiology* **240**, 326-331 (2017).
- [20] J. M. Lee, H. K. Kim, K. S. Lim, J.-K. Park, K. H. Choi, J. Park, D. Hwang, T.-M. Rhee, J. H. Yang, E.-S. Shin, "Influence of Local Myocardial Damage on Index of Microcirculatory Resistance and

- Fractional Flow Reserve in Target and Nontarget Vascular Territories in a Porcine Microvascular Injury Model". *JACC: Cardiovascular Interventions* **11**, 717-724 (2018).
- [21] H. W. Krenn, "Feeding mechanisms of adult Lepidoptera: structure, function, and evolution of the mouthparts". *Annu. Rev. Entomol.* **55**, 307-327 (2010).
- [22] H. W. Krenn, "Functional morphology and movements of the proboscis of Lepidoptera (Insecta)". *Zoomorphology* **110**, 105-114 (1990).
- [23] H. Bänziger, "Extension and coiling of the lepidopterous proboscis—a new interpretation of the blood-pressure theory". *Mitt. Schweiz. Entomol. Ges* **43**, 225-239 (1971).
- [24] H. Sung, J. Lee, K. Han, J.-K. Lee, J. Sung, D. Kim, M. Choi, C. Kim, "Controlled positioning of metal nanoparticles in an organic light-emitting device for enhanced quantum efficiency". *Org. Electron.* **15**, 491-499 (2014).
- [25] W. Kim, S. Kwon, S.-M. Lee, J. Y. Kim, Y. Han, E. Kim, K. C. Choi, S. Park, B.-C. Park, "Soft fabric-based flexible organic light-emitting diodes". *Org. Electron.* **14**, 3007-3013 (2013).
- [26] D. Kang, P. V. Pikhitsa, Y. W. Choi, C. Lee, S. S. Shin, L. Piao, B. Park, K.-Y. Suh, T.-i. Kim, M. Choi, "Ultrasensitive mechanical crack-based sensor inspired by the spider sensory system". *Nature* **516**, 222 (2014).
- [27] T. Lee, Y. W. Choi, G. Lee, S. M. Kim, D. Kang, M. Choi, "Crack-based strain sensor with diverse metal films by inserting an inter-

- layer". *RSC Adv.* **7**, 34810-34815 (2017).
- [28] Z. Suo, E. Ma, H. Gleskova, S. Wagner, "Mechanics of rollable and foldable film-on-foil electronics". *Applied Physics Letters* **74**, 1177-1179 (1999).
- [29] C.-C. Lee, Y.-S. Shih, C.-S. Wu, C.-H. Tsai, S.-T. Yeh, Y.-H. Peng, K.-J. Chen, "Development of robust flexible OLED encapsulations using simulated estimations and experimental validations". *Journal of Physics D: Applied Physics* **45**, 275102 (2012).
- [30] J.-H. Kim, A. Nizami, Y. Hwangbo, B. Jang, H.-J. Lee, C.-S. Woo, S. Hyun, T.-S. Kim, "Tensile testing of ultra-thin films on water surface". *Nature communications* **4**, 2520 (2013).
- [31] R. A. Meiriom, "Mechanical Behavior of Nanocrystalline Platinum Thin Films". (2011).
- [32] J. Paek, I. Cho, J. Kim, "Microrobotic tentacles with spiral bending capability based on shape-engineered elastomeric microtubes". *Sci. Rep.* **5**, 10768 (2015).
- [33] R. F. Shepherd, F. Ilievski, W. Choi, S. A. Morin, A. A. Stokes, A. D. Mazzeo, X. Chen, M. Wang, G. M. Whitesides, "Multigait soft robot". *Proc. Natl. Acad. Sci. U. S. A.* **108**, 20400-20403 (2011).
- [34] P. Rothemund, A. Ainla, L. Belding, D. J. Preston, S. Kurihara, Z. Suo, G. M. Whitesides, "A soft, bistable valve for autonomous control of soft actuators". *Sci. Rob.* **3**, eaar7986 (2018).
- [35] R. C. Webb, Y. Ma, S. Krishnan, Y. Li, S. Yoon, X. Guo, X. Feng, Y. Shi, M. Seidel, N. H. Cho, "Epidermal devices for noninvasive, precise, and continuous mapping of macrovascular and

- microvascular blood flow". *Sci. Adv.* **1**, e1500701 (2015).
- [36] K.-H. Shin, C.-R. Moon, T.-H. Lee, C.-H. Lim, Y.-J. Kim, "Flexible wireless pressure sensor module". *Sens. Actuators, A* **123**, 30-35 (2005).
- [37] J. Lee, D.-H. Kim, K. J. Lee, I. H. Seo, S. H. Park, E. H. Jang, Y. Park, Y.-N. Youn, W. Ryu, "Transfer-molded wrappable microneedle meshes for perivascular drug delivery". *J. Controlled Release* **268**, 237-246 (2017).
- [38] J. Reeder, M. Kaltenbrunner, T. Ware, D. Arreaga-Salas, A. Avendano-Bolivar, T. Yokota, Y. Inoue, M. Sekino, W. Voit, T. Sekitani, "Mechanically adaptive organic transistors for implantable electronics". *Adv. Mater.* **26**, 4967-4973 (2014).
- [39] T. Shimizu, M. Yamato, A. Kikuchi, T. Okano, "Cell sheet engineering for myocardial tissue reconstruction". *Biomaterials* **24**, 2309-2316 (2003).
- [40] K. Tadakuma, N. Tanaka, Y. Haraguchi, M. Higashimori, M. Kaneko, T. Shimizu, M. Yamato, T. Okano, "A device for the rapid transfer/transplantation of living cell sheets with the absence of cell damage". *Biomaterials* **34**, 9018-9025 (2013).
- [41] J. Yang, M. Yamato, T. Shimizu, H. Sekine, K. Ohashi, M. Kanzaki, T. Ohki, K. Nishida, T. Okano, "Reconstruction of functional tissues with cell sheet engineering". *Biomaterials* **28**, 5033-5043 (2007).

Chapter 4.

Ultra-Flexible Perovskite Solar Cells by Studying the Mechanical Fracture Behavior

4.1. Introduction

Flexible and lightweight photovoltaics have expected as a candidate for portable and wearable electronic applications such as deformable displays, electronic textiles, and artificial skins.[1-3] Especially, organic-inorganic halide perovskite materials for functional photovoltaics have attracted enormous interest as suitable power source for such applications due to their high power conversion efficiency (PCE), low temperature processing and low cost fabrication.[4-7] In that huge interest, flexible perovskite solar cells have been studied and developed for past several years through various engineering approaches such as introduction of additive materials,[8-10] advance of device structure,[11, 12] substitution of brittle transparent electrode for graphene,[13-15] carbon nanotube,[15-17] silver nanowire[18, 19] and high conductive polymer.[20, 21]

However, current flexible perovskite photovoltaics is still far from practical application for portable devices in respect of bending durability. In many researches, cyclic bending tests of flexible perovskite solar cells had

been only conducted at large bending radii for few thousands of cycles.[22, 23] In most cases, cracks are generated on the perovskite films after such lenient bending tests, which leads to direct performance degradation.[17, 21, 24] Perovskite devices with such inferior deformation durability is not suitable for practical flexible devices because severe deformations as complete crumpling, folding, and rolling could occur in actual operation.[25, 26] Therefore, flexible perovskite photovoltaic that endures much stricter measurement standards is needed for portable power sources. In addition, it is crucial to develop large-area flexible devices with high photovoltaic performance for more practical use.

Herein, we demonstrated high efficiency, ultra-flexible perovskite solar cells (PCE of 17.03 %) which maintain initial performance after 10,000 bending cycles at 0.5 mm bending radius, which surpasses the most superior bending durability reported so far. Surprisingly, the device has endured 10 times of complete crumpling and rolling, which is the first reported flexible perovskite device that survives crumpling and rolling deformation tests. By fabricating crack-free perovskite films on ultra-thin polyethylene terephthalate (PET) substrate ($\sim 2.5 \mu\text{m}$) with the aid of polydimethylsiloxane (PDMS) supports, we are able to achieve these remarkable bending durable results which cannot be realized using typical thickness (30~100 μm) of PET substrates. We additionally compare photovoltaic performance and crack generation of the perovskite films after 1,000 bending cycles with different substrate thicknesses in order to manipulate applied strains on the perovskite surface. From the morphological observations by scanning electron microscopy (SEM) measurement and finite element method (FEM)

simulation, we have identified the relationship between crack formation and the applied strains to perovskite films and have found the mechanical fracture points of the poly-crystalline perovskite films. In addition, we have successfully demonstrated the world's best efficiency of large-area flexible perovskite solar cells that have 1.2 cm² active area without the conducting oxide as a transparent electrode (13.6 %) which is replaced by hybrid transparent electrodes of conducting polymer and metal mesh grid. The large-area device has also showed comparable deformation durability to a small-area one. As we achieve ultra-flexible, large active area perovskite solar cell with high efficiency which endures harsh deformation (small radius bending, crumpling, and rolling), we expect that our device can be further developed as commercially viable portable power sources.

4.2. Experimental Methods

4.2.1. Fabrication of flexible perovskite solar cells

Thin films of polydimethylsiloxane (PDMS) (Dow Corning, Sylgard 184) was bonded on a glass substrate by oxygen plasma treatment (CUTE-1MPR, Femto Science Inc.). The PET substrates were attached on the PDMS/glass substrate during the fabrication process. PEDOT:PSS solution (Clevios PH1000, Heraeus) was spin coated at 3000 rpm for 1 min and annealed at 120 °C for 20 min. Then methanol was dripped on PEDOT:PSS/PET/glass substrate during spin coating at 4000 rpm for 1min. The perovskite layer ($\text{CH}_3\text{NH}_3\text{PbI}_3$) which is light absorbing layer was formed on PEDOT:PSS layer using the Lewis base adduct method.[28] A precursor solution was prepared by dissolving PbI_2 (Alfa Aesar)/MAI(Xian' Chemical)/dimethyl sulfoxide (DMSO, Sigma Aldrich) into dimethyl formamide (DMF, Sigma Aldrich) at specified proportions. A perovskite solution was spincoated at 4000 rpm for 20 s and diethyl ether (Sigma Aldrich) was dripped during procedure, followed by annealing at 70 °C for 1min and at 110 °C for 10min. All spin coating process were performed inside a dry room with a relative humidity of less than 10% and temperature of 25 °C. Then, C_{60} (20 nm)/BCP (10 nm) layer which is the electron transport layer and copper electrode were deposited on the perovskite layer using vacuum thermal evaporator. Furthermore, preparation of flexible substrate with a gold mesh electrode was followed. PDMS was spin coated on an silicon (Si) wafer at 6000 rpm

for 5 min and then annealed at 70 °C for 1 hour. After annealing process, the PET film was attached conformally on PDMS/Si wafer. The gold grid electrode which designed with 200 nm width and 2 μm space was prepared by conventional photolithography method.

4.2.2. FEM simulation method

For the 2-Dimensional finite element analysis of bending experiment, ABAQUS, commercial finite element analysis package, is used. In this analysis, each substance layer of solar panel is discretized by CPS4 element (A 4-node bilinear plane stress quadrilateral element). The element sizes are as follows: PET (0.8 - 1 X 3 μm), PEDOT_PSS (0.13 X 3 μm) and Perovskite (0.5 X 3 μm). For the two rigid spherical indenters and the constantly curved rigid plate are discretized by R2D2 element (A 2-node 2-D linear rigid link element). The analysis is performed by changing the radius of curved rigid plate (0.5 and 1 mm) and the thickness of PET (i.e. 2.5, 30 and 100 μm). The two-dimensional finite element analysis is performed as follows: Two rigid spherical indenters, which are placed on the sides of the solar cells at a certain distance above which consists of perovskite, PEDOT:PSS and PET, move downward to contact the upper surface of the device. After this contact, the two rigid surfaces and the solar panel move downward together to contact the upper surface of the constantly curved rigid plate. These contact and continuous downward motions induce the bending motion of the device. The downward moving motion that induces bending keeps until the lower surface of the device is fully adjusted to the curvature of the curved rigid surface.

4.2.3. Characterization

The J-V characteristics were measured by using a source meter (Keithley 2400, Tektronix) under AM 1.5G illumination condition at an intensity of 100 mW/cm² with an Oriel S013 ATM solar simulator, calibrated by a KG-5 filtered standard silicon reference solar cell (91150-KG5, Newport). Our devices were measured in room temperature (25 °C) glove box. The forward and reverse scan rates were set to 200 ms per 20 mV. EQE spectra was measured with a Newport IQE200 system equipped with a 100 mW Xenon lamp and a lock-in amplifier. The SEM images of plane-view were obtained by using a field-emission scanning electron microscopy (MERLIN, Carl Zeiss) while the cross-sectional images were obtained with the focused-ion-beam (FIB) system (AURIGA, Carl Zeiss). The cyclic bending test was performed at a frequency of 1 Hz by using bending test machine (1Axis, Science Town). The Transmittance spectra of substrates were obtained using a UV-visible spectrophotometer (Cary 5000, Agilent technologies). Sheet resistance of transparent electrode was measured with a four-point probe (CMT-SR1000N, AIT).

4.3. Results and Discussion

4.3.1. Device structure and uniformity issue of perovskite film coating

For achieving ultra-flexible perovskite solar cells deposited on ultra-thin substrate ($\sim 2.5 \mu\text{m}$), it is necessary to coat a high quality perovskite film on an ultra-thin polymer substrate. However, the spin coating process that is usually used to make the solar cells easily fails when using an ultra-thin PET substrate. In order to prevent technical problems due to the wrinkling or folding of ultra-thin flexible substrates, it is required to stabilize the fabrication process of flexible perovskite solar cell. (**Figure. 4.1a**) This could be done by taking advantage of conformal contact of PDMS. We have used PDMS layers between a $2.5 \mu\text{m}$ thick PET substrate and glass rigid substrates as a supporting fixture and obtained a firm substrate that does not wrinkle or fold during the full fabrication procedure. (**Figure. 4.1a**) Since the complete device with the PET film could be easily detached from the PDMS/rigid substrate at the end of fabrication, the use of PDMS enables us to fabricate flexible devices without handling problems. We have prepared perovskite solar cells with p-i-n structure (PEDOT:PSS/MAPbI₃/C₆₀/BCP/Cu) without brittle transparent conducting oxide (TCO) as can be seen in **Figure. 4.1b**. Removal of brittle TCO is to prohibit crack propagation on it in advance. [27] Finally, we have achieved highly efficient flexible perovskite solar cells with homogeneous PEDOT:PSS and MAPbI₃ layers regardless of different thickness of PET substrates ($100 \mu\text{m}$, $30 \mu\text{m}$ and $2.5 \mu\text{m}$ thickness). The

average PCEs of three types of devices have presented almost comparable values as summarized in **Figure. 4.1c** as in the box chart. From these results, we have confirmed the reliability of our fabrication method for flexible devices.

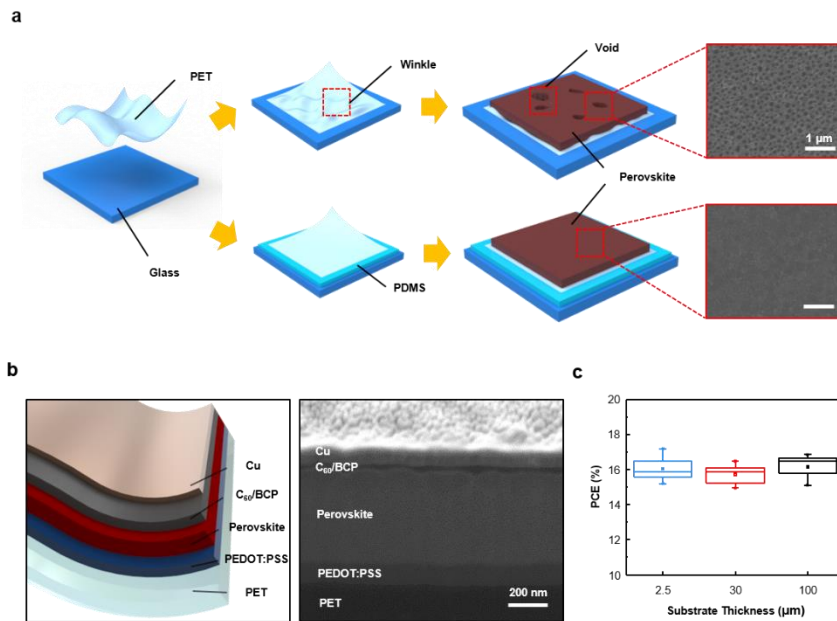


Figure 4.1 (a) Graphical illustration of the difference of the perovskite film quality depending on the existence of PDMS. **(b)** Schematic illustration and cross-sectional SEM images of device structure of the flexible perovskite solar cell. **(c)** Box chart of PCEs of three devices with different substrate thicknesses (2.5 μm , 30 μm , and 100 μm)

4.3.2. Analysis on mechanical fracture behavior

Surprisingly, flexible perovskite photovoltaics which exhibit the equivalent initial efficiencies perform entirely different final efficiencies after 1,000 of bending cycles depending on the substrate thickness. **Figure. 4.2a** shows J - V curves of three devices before and after 1,000 cyclic bending test at bending radius (R) of 0.5 mm. Hereafter, we denote the devices with a PET substrate that is d μm thick as a d -PET device for the sake of simplicity in the following discussion. In the case of a 2.5-PET device, J - V curves have hardly changed after 1,000 cycles of bending, while both 30-PET and 100-PET devices have shown severe performance degradation in the same condition. Severe decrease of performance in thicker substrates implies the possibility of crack generation in the MAPbI_3 film as depicted in **Figure. 4.2b**. To examine the performance degradation and generation of cracks during cyclic bending further, we have performed detailed cyclic bending tests with two bending radii ($R = 1$ mm and 0.5 mm) according to substrate thicknesses and measured the evolution of photovoltaic performance and morphologies (**Figure. 4.3**). In the case of the 2.5-PET device, there has been no change of both performance and surface morphologies after 1,000 cyclic bending at both bending radii as shown in **Figure. 4.3a-c**. On the other hand, the 100-PET device with the thickest substrate showed significant performance degradation and a lot of deep cracks with few-hundred nanometer gaps in both bending radii (**Figure. 4.3g-i**). Such evolution of PCE is mainly contributed to lower the MAPbI_3 film quality due to crack formation. Notably, for the 30-PET device, $\sim 95\%$ of its initial value has been

preserved at 1 mm bending radius, while the same device degrades in PCE to ~65% of its original value at 0.5 mm bending radius as can be seen in **Figure. 4.3d**. Surface morphologies after 1,000 have also displayed distinct characteristics according to different bending radii. In the case of $R = 1$ mm, cracks are formed along grain boundaries whereas deep and long ones are appeared through individual MAPbI₃ grains in the case of $R = 0.5$ mm. (**Figure. 4.3e and f**) From the fact that there are no cracks on the PEDOT:PSS surface deposited on the 30-PET substrate after 1,000 cycles of bending at the 0.5 mm and 1 mm bending radii (**Figure. 4.4**), we deduce that cracks are originated from the perovskite surface. That is to say, such performance drop is highly associated with overall crack densities of the MAPbI₃ films. From these experimental results, we have newly discovered the deformation limit of the poly-crystalline MAPbI₃ thin films as shown in **Figure. 4.5**. Generation of cracks and their density depend on both substrate thickness and bending radius, which is indicative of strain-dependent yield characteristics of the films. To support these results, we also performed FEM simulations as can be seen in **Figure. 4.6**, in which the thicker the substrate and the smaller bending radius are, the more strain is applied to the device.

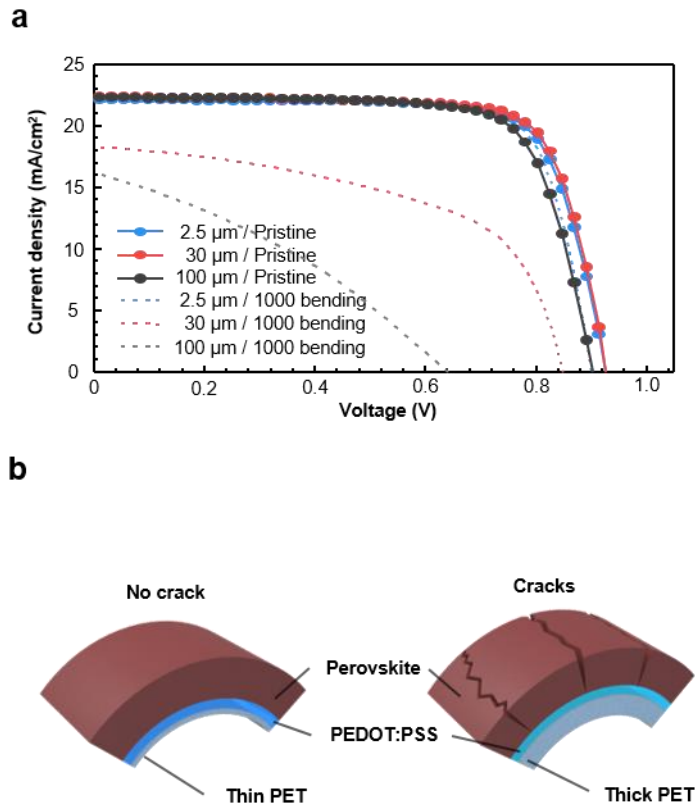


Figure 4.2 (a) J-V curves of the perovskite solar cells before and after cyclic bending tests ($R = 0.5$ mm, 1,000 cycles) with different substrate thicknesses. (b) Schematic illustrations of the substrate thickness in the perovskite film upon sustainable bending.

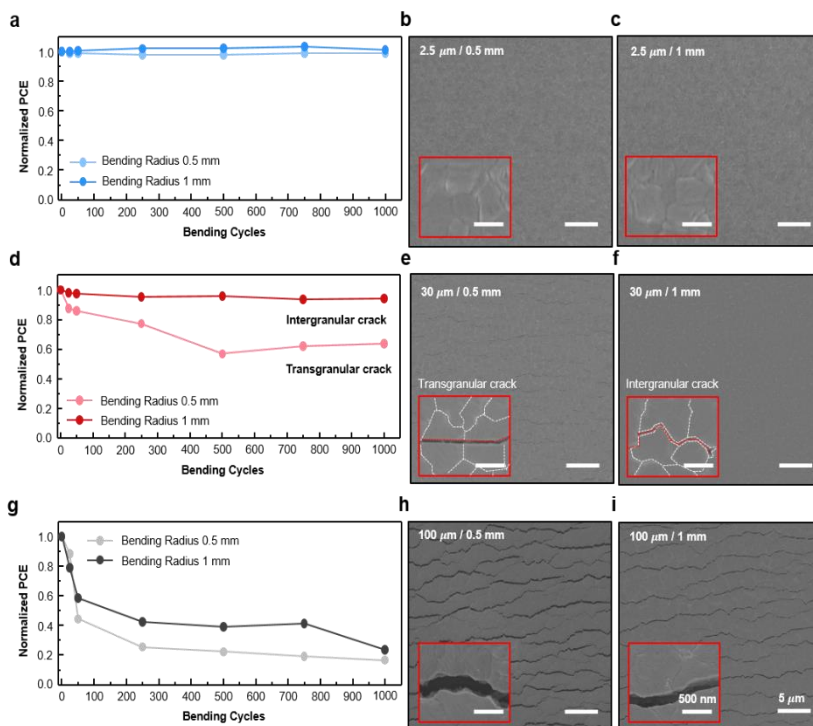


Figure 4.3 Normalized PCEs as a function of bending cycles for the substrates with the thickness of (a) 2.5 μm, (d) 30 μm and (g) 100 μm at 0.5 mm and 1 mm bending radii. SEM Images of the perovskite film after bending cyclic tests for the substrates with the thickness of (b, c) 2.5 μm, (e, f) 30 μm and (h,i) 100 μm at 0.5 mm and 1mm bending radii

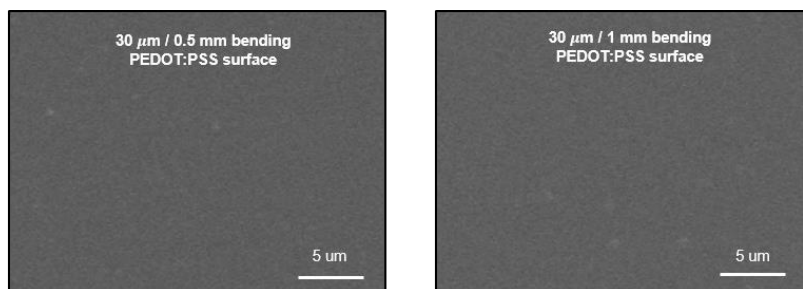


Figure 4.4 SEM Images of PEDOT:PSS surface after cyclic bending test for 30 μm substrate thickness at different bending radius ($R = 1$ and 0.5 mm)

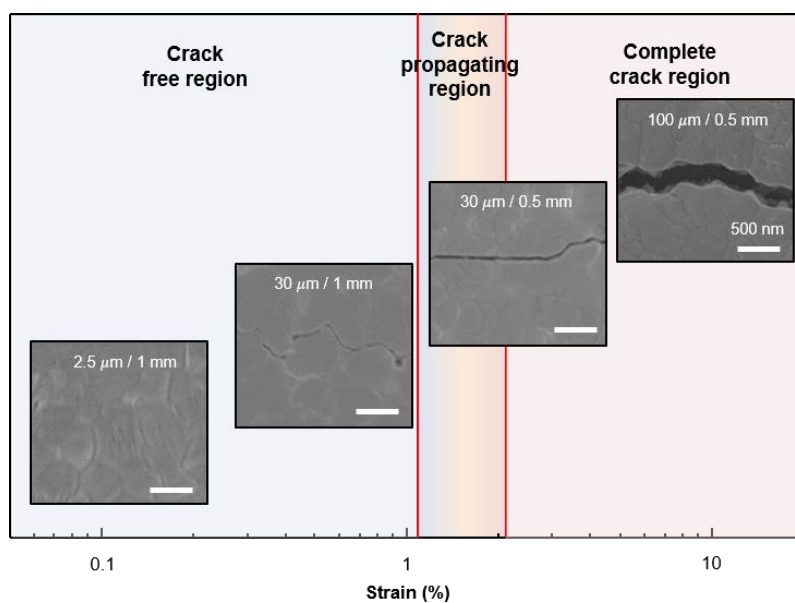


Figure 4.5 Relationship of crack formation and applied strain on perovskite film based on FEM results and SEM images

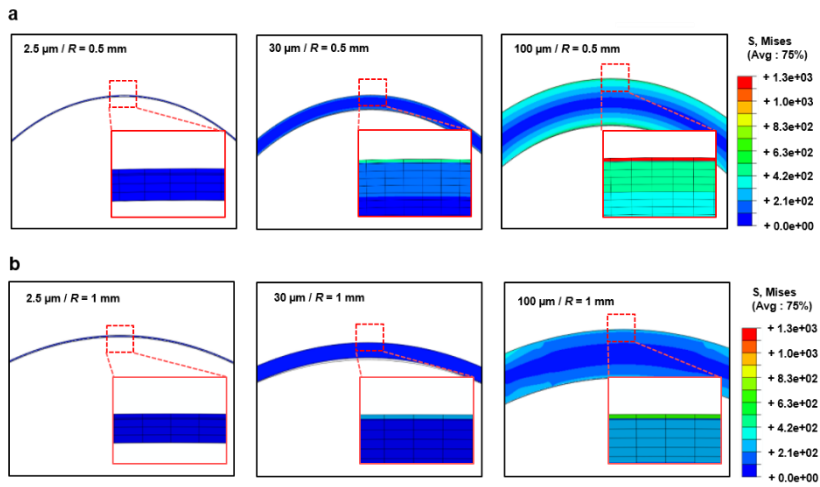


Figure 4.6 FEM simulation results of applied stress on perovskite film with different substrate thickness at fixed bending radius of (a) 0.5mm and (b) 1 mm

4.3.3. Device characteristics

Based on our experimental results and analysis, we have figured out that adopting an ultra-thin substrate is demanded for excellent device flexibility. Additional experiments are performed to see if the perovskite film could tolerate even harsher bending condition. Since the 2.5-PET device presents the best bending durability among all cases (**Figure. 4.2a**) with no crack generation on the perovskite films, we have optimized the device performance and confirmed the endurance of the flexible devices in intensive deformation conditions (10,000 cycle bending test, complete rolling, and crumpling) which are essential requirements for portable device application. By employing the 2.5 μm thick PET substrate, we have achieved 17.03% PCE with short-circuit current density (J_{SC}) of 22.45 mA/cm^2 , open-circuit voltage (V_{OC}) of 0.96, a fill factor (FF) of 0.79 and negligible hysteresis for the best performing devices as shown in **Figure. 4.7a**. By using the PDMS-assisted fabrication method as shown in **Figure. 4.1c** to produce 45 devices, we have verified the reproducibility of the 2.5-PET based perovskite solar cells as depicted in **Figure. 4.8**. The average values of photovoltaic parameters for the 2.5-PET devices are summarized in **Table 4.1** which provides another evidence of their reproducibility. We have also measured the stabilized current density and external quantum efficiency (EQE) as shown in **Figure. 4.9**, which are in good agreement with results of J-V curve measurement. To examine the durability of the flexible perovskite devices in harsh conditions, we have carried out cyclic bending tests at various bending radii ($R = 2, 1$ and 0.5 mm) for 10,000 cycles in **Figure. 4.7b**. It is noteworthy

that the 2.5-PET device do not exhibit performance degradation at all after 10,000 cycles of bending for all the bending radii (**Figure. 4.7b**). Inset images show the detailed bending tests according to various bending radii. This is the first report which demonstrates the durability of flexible perovskite solar cells even after 10,000 bending cycles. As can be seen in Fig. 3b, the perovskite devices survive at bending radius of 0.5 mm, which proves the durability against complete rolling or crumpling configuration. Accordingly, we have performed a rolling test in which we tightly rolled the perovskite photovoltaic devices repeatedly around an ultra-thin rod with a 0.5 mm radius (as depicted in inset images of **Figure. 4.7c**). The rolling condition causes even more intensive deformation than bending for the perovskite solar cells, because large strain or stress is applied not only on a specific small area but on the entire surface of the perovskite films. It has been observed that the 2.5-PET device has well endured such a severe deformation condition as can be seen in **Figure. 4.7c**. As the most intensive deformation test, we have crumpled the flexible devices by putting them in small tablets (inner diameter: 7.5 mm). Also, in this case, the 2.5-PET device have exhibited no performance degradation after crumpling. (**Figure. 4.7d**) We have conducted both rolling and crumpling tests for 10 times consecutively to attain reliability for each deformation test as depicted in **Figure. 4.10**, and the 2.5-PET devices retain their PCEs about 90% after 10 times of the deformation tests.

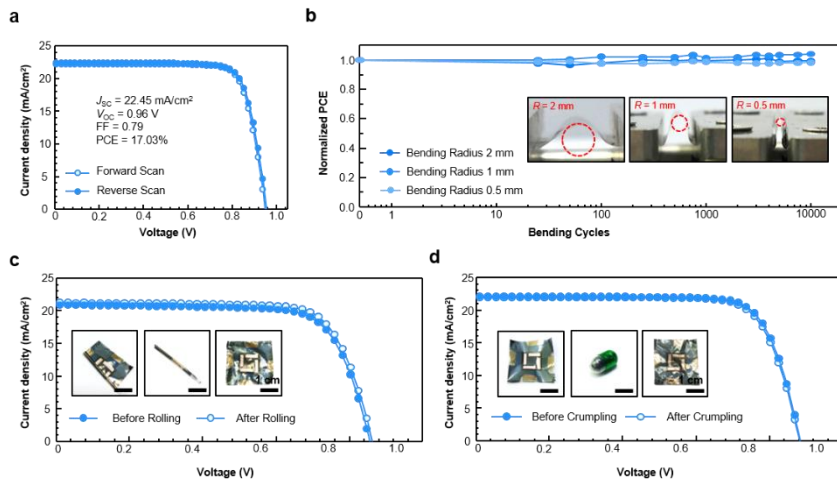


Figure 4.7 (a) Reverse and forward bias J-V curves of the perovskite solar cell used a 2.5 μm thick substrate. (b) Normalized PCEs as a function of bending cycles depending on bending radius ($R = 2$, 1, and 0.5 mm) at the 2.5 μm thick substrate. The inset photograph shows the device bent at various bending radii. The J-V curves of the devices before and after (c) rolling and (d) crumpling tests. The inset photograph shows the rolling and crumpling process

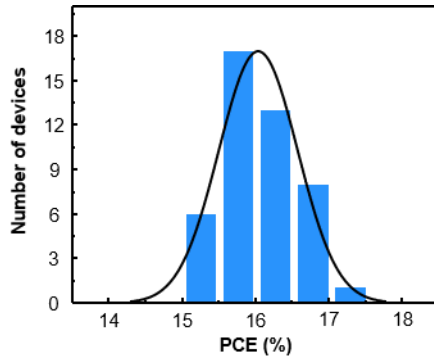


Figure 4.8 Histograms of PCE of 45 devices using 2.5 μm substrate

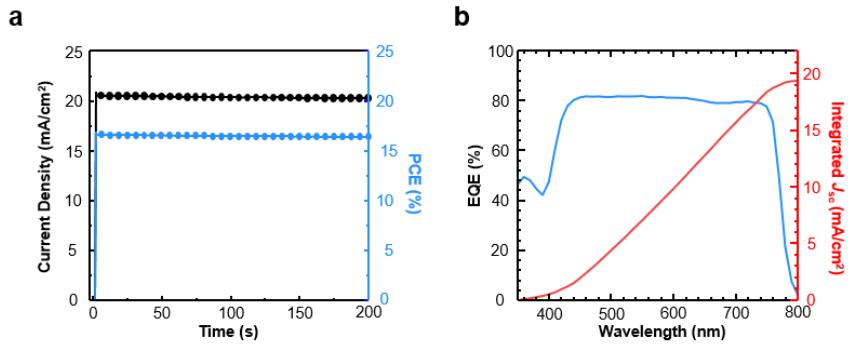


Figure 4.9 (a) Steady-state photocurrent density (black) and power conversion efficiency (blue) measured at the maximum power voltage of 0.81 V for 200 sec. (b) EQE spectra (blue) and the integrated JSC (red) of perovskite solar cell

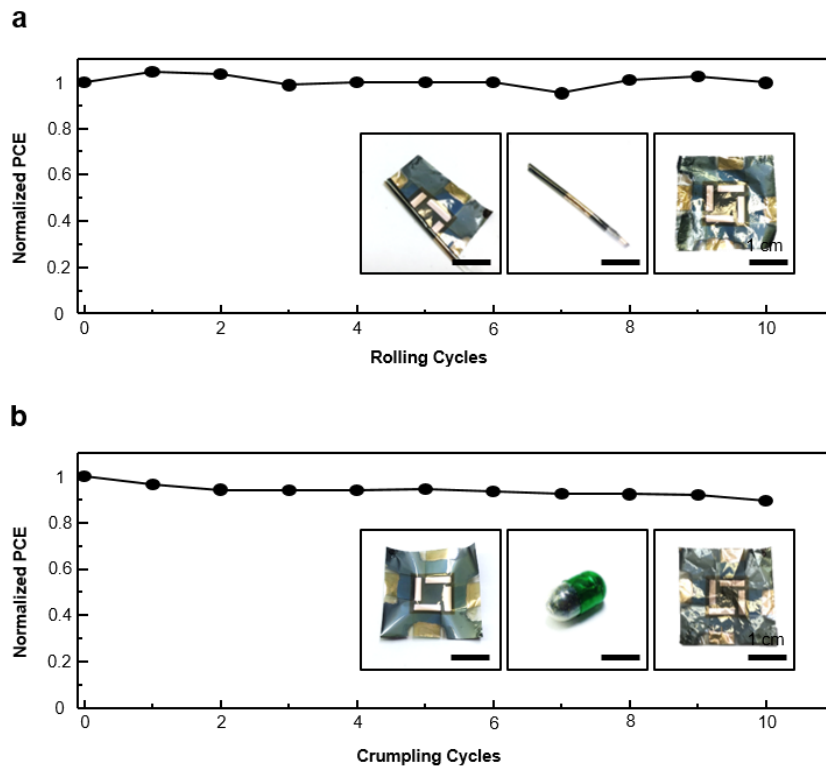


Figure 4.10 Normalized PCEs of perovskite devices as a function of (a) rolling and (b) crumpling cycles at 2.5 μm thickness substrate

		V_{oc} (V)	J_{sc} (mA/cm ²)	FF	PCE (%)
Small area (0.0756 cm ²)	Average	0.95±0.02	21.23±0.66	79.47±1.93	16.04±0.53
	Best	0.96	22.45	79.39	17.03
Large area (1.2 cm ²)	Average	0.90±0.03	20.16±1.00	67.68±3.97	12.21±0.92
	Best	0.87	20.76	75.45	13.62

Table 4.1 Photovoltaic parameters of flexible perovskite solar cells corresponding to the active area.

4.3.4. Large area device characteristics

In spite of the result that the 2.5-PET device has endured 10,000 cyclic bending, rolling and crumpling, there is still a limitation of actual application due to their small active area ($\sim 0.1 \text{ cm}^2$ for each device). It is challenging to fabricate large-area flexible perovskite solar cells with both high mechanical durability and performance due to lower electrical conductivity of bending durable electrodes than brittle conducting oxide. To overcome trade-offs between bending durability and conductivity, we introduce a gold metal mesh grid underneath the conducting polymer and have successfully fabricated perovskite solar cells (**Figure. 4.11a**) with these hybrid transparent electrodes which have high lateral conductivity (**Table 4.2**). The metal mesh grid leads to slight loss of transmittance by reflecting the incident light, which, however, does not have any noticeable effect on device performance (**Figure. 4.11b**). As a result, performance of the device with the gold mesh has dramatically increased compared to the case without it (**Figure. 4.11c**). Finally, we achieve up to 13.62 % efficiency which is, to the best of our knowledge, the highest efficiency among the transparent conducting oxide free flexible perovskite solar cells with an active area over 1 cm^2 (**Figure. 4.11c**). The reproducibility of the large-area flexible perovskite solar cells is verified by histograms of 20 devices shown in **Figure. 4.12** and all photovoltaic parameters are summarized in **Table 4.1**. We have performed the cyclic bending tests for both the PEDOT:PSS/metal mesh grid/PET sample and the MAPbI₃/PEDOT:PSS/metal mesh grid/PET, to verify that the introduction of the metal mesh grid affects the flexibility of

the device. By observing the morphology of the hybrid electrodes consisting of metal mesh grid and PEDOT:PSS, we have confirmed that the hybrid electrode is not destroyed at all after bending as shown in **Figure. 4.11d**. Also, the perovskite surface has no cracks after 1,000 cycles of bending. (**Figure. 4.11d**) Finally, we conclude that the large-area device has superior bending durability and the metal mesh based hybrid electrode has not significantly affected photovoltaic performance after bending. As the consequence of no morphological change, no performance degradation has been observed after 1,000 cycles of bending at $R = 1$ and 0.5 mm (**Figure. 4.11e**). Moreover, we have further conducted the intensive deformation test (rolling and crumpling) for the large-area devices as we have done for small area devices. The large-area devices have maintained their PCEs after 10 cycles of rolling as can be seen in **Figure. 4.13**. In the case of the crumpling tests for the large-area devices, they undergo about 20% of performance degradation after 10 times of crumpling as shown in **Figure. 4.13**. These results of the crumpling tests are indicative of sufficient feasibility for portable and flexible power sources.

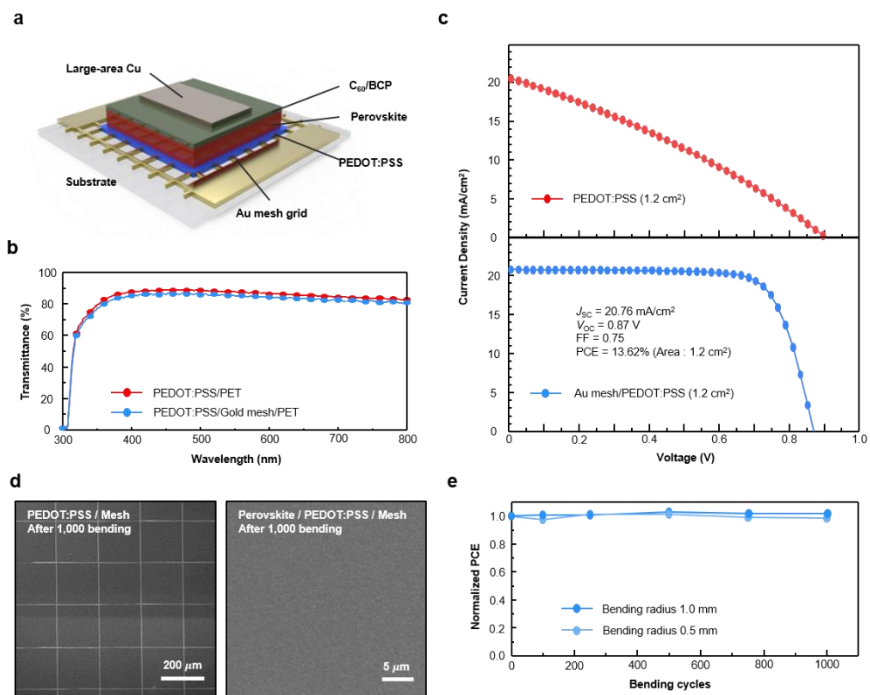


Figure 4.11 (a) Schematic illustration of the structure of large area flexible perovskite solar cell using a gold mesh grid. (b) The transmittance of ITO/glass, PEDOT:PSS/PET and PEDOT:PSS/PET substrates. (c) J-V curves of the large area device (1.2 cm²) with and without the gold mesh grid. (d) Normalized PCEs of large area devices as a function of bending cycles depending on bending radius ($R = 1$, and 0.5 mm) at the 2.5 μm thick substrate. (e) SEM images of hybrid electrode (gold mesh and PEDOT:PSS) and perovskite film after bending tests

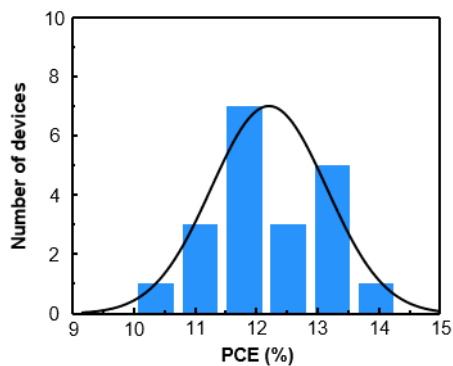


Figure 4.12 Histograms of PCE of 20 devices of large area (1.2 cm²) flexible perovskite solar cells

	Average (Ω/\square)	Standard deviation
PEDOT:PSS	234.3	4.64
Gold Mesh/PEDOT:PSS	18.0	1.08

Table 4.2 Sheet resistances of PEDOT:PSS/PET and PEDOT:PSS/gold mesh/PET substrate.

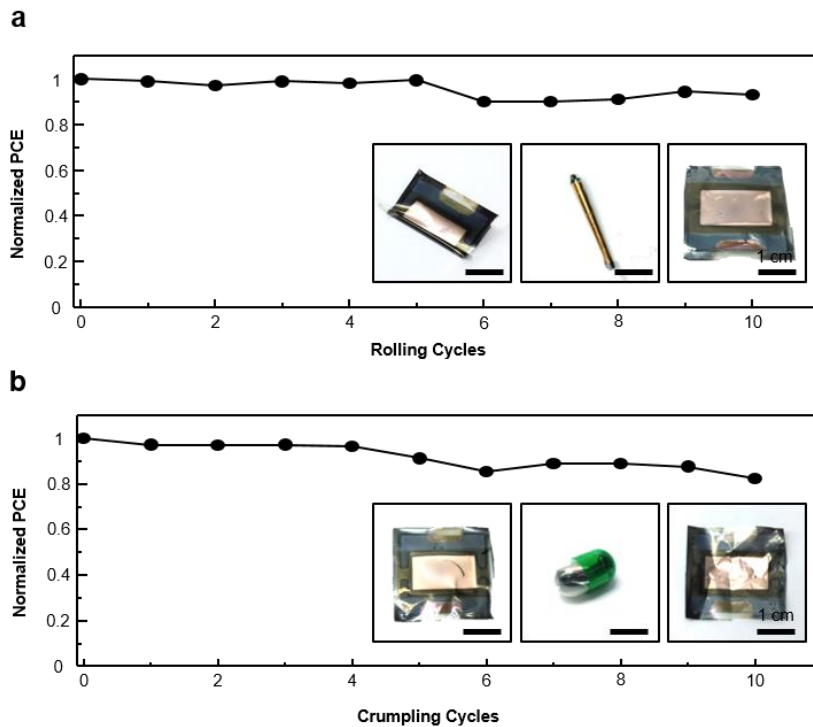


Figure 4.13 Normalized PCEs of large area perovskite devices as a function of (a) rolling and (b) crumpling cycles at 2.5 μm thickness substrate.

4.4. Conclusion

We achieved ultra-flexible perovskite photovoltaic devices whose performance maintained after 10,000 cycles of bending at 0.5 mm bending radius or intense deformation such as crumpling or rolling with ultra-thin flexible substrate. Investigation on crack generation of perovskite thin films according to different substrate thicknesses provides a great help in improving the bending or deformation durability of the flexible perovskite solar cells. We showed that the flexible photovoltaic devices with a thinner substrate exhibit better bending durability. Furthermore, by applying a hybrid transparent electrode composed of conducting polymer (PEDOT:PSS) and gold mesh grid, we have successfully expanded the active area (1.2 cm^2) which presents the efficiency of 13.6%, which is the highest among the transparent conducting oxide free flexible perovskite solar cells over 1 cm^2 , with the subsequent deformation durability compared to a small-area device. We believe that the successful fabrication of the high mechanical durable perovskite solar cells enduring crumpling and rolling will contribute to developing the flexible perovskite solar cells for practical portable power sources.

4.5. References

- [1] M. Kaltenbrunner, M. S. White, E. D. Głowacki, T. Sekitani, T. Someya, N. S. Sariciftci, S. Bauer, "Ultrathin and lightweight organic solar cells with high flexibility". *Nature communications* **3**, 770 (2012).
- [2] A. J. Baca, K. J. Yu, J. Xiao, S. Wang, J. Yoon, J. H. Ryu, D. Stevenson, R. G. Nuzzo, A. A. Rockett, Y. Huang, "Compact monocrystalline silicon solar modules with high voltage outputs and mechanically flexible designs". *Energy & Environmental Science* **3**, 208-211 (2010).
- [3] B. J. Kim, D. H. Kim, Y.-Y. Lee, H.-W. Shin, G. S. Han, J. S. Hong, K. Mahmood, T. K. Ahn, Y.-C. Joo, K. S. Hong, "Highly efficient and bending durable perovskite solar cells: toward a wearable power source". *Energy & Environmental Science* **8**, 916-921 (2015).
- [4] D. Liu, T. L. Kelly, "Perovskite solar cells with a planar heterojunction structure prepared using room-temperature solution processing techniques". *Nature photonics* **8**, 133 (2014).
- [5] F. Di Giacomo, A. Fakharuddin, R. Jose, T. M. Brown, "Progress, challenges and perspectives in flexible perovskite solar cells". *Energy & Environmental Science* **9**, 3007-3035 (2016).
- [6] S. S. Shin, W. S. Yang, J. H. Noh, J. H. Suk, N. J. Jeon, J. H. Park, J. S. Kim, W. M. Seong, S. I. Seok, "High-performance flexible perovskite solar cells exploiting Zn₂SnO₄ prepared in solution

- below 100 C". *Nature communications* **6**, 7410 (2015).
- [7] C. Bi, B. Chen, H. Wei, S. DeLuca, J. Huang, "Efficient Flexible Solar Cell based on Composition-Tailored Hybrid Perovskite". *Advanced Materials* **29**, (2017).
- [8] Z. Huang, X. Hu, C. Liu, L. Tan, Y. Chen, "Nucleation and Crystallization Control via Polyurethane to Enhance the Bendability of Perovskite Solar Cells with Excellent Device Performance". *Advanced Functional Materials* **27**, (2017).
- [9] D. Yang, R. Yang, X. Ren, X. Zhu, Z. Yang, C. Li, S. F. Liu, "Hysteresis-Suppressed High-Efficiency Flexible Perovskite Solar Cells Using Solid-State Ionic-Liquids for Effective Electron Transport". *Advanced Materials* **28**, 5206-5213 (2016).
- [10] S. Song, R. Hill, K. Choi, K. Wojciechowski, S. Barlow, J. Leisen, H. J. Snaith, S. R. Marder, T. Park, "Surface modified fullerene electron transport layers for stable and reproducible flexible perovskite solar cells". *Nano Energy* **49**, 324-332 (2018).
- [11] H. I. Kim, M. J. Kim, K. Choi, C. Lim, Y. H. Kim, S. K. Kwon, T. Park, "Improving the Performance and Stability of Inverted Planar Flexible Perovskite Solar Cells Employing a Novel NDI-Based Polymer as the Electron Transport Layer". *Advanced Energy Materials* **8**, 1702872 (2018).
- [12] X. Hu, Z. Huang, X. Zhou, P. Li, Y. Wang, Z. Huang, M. Su, W. Ren, F. Li, M. Li, "Wearable Large-Scale Perovskite Solar-Power Source via Nanocellular Scaffold". *Advanced Materials* **29**, (2017).
- [13] J. Yoon, H. Sung, G. Lee, W. Cho, N. Ahn, H. S. Jung, M. Choi,

- "Superflexible, high-efficiency perovskite solar cells utilizing graphene electrodes: towards future foldable power sources". *Energy & Environmental Science* **10**, 337-345 (2017).
- [14] J. H. Heo, D. H. Shin, D. H. Song, D. H. Kim, S. J. Lee, S. H. Im, "Super-flexible bis (trifluoromethanesulfonyl)-amide doped graphene transparent conductive electrodes for photo-stable perovskite solar cells". *Journal of Materials Chemistry A* **6**, 8251-8258 (2018).
- [15] Q. Luo, H. Ma, Q. Hou, Y. Li, J. Ren, X. Dai, Z. Yao, Y. Zhou, L. Xiang, H. Du, "All-Carbon-Electrode-Based Endurable Flexible Perovskite Solar Cells". *Advanced Functional Materials*, (2018).
- [16] I. Jeon, T. Chiba, C. Delacou, Y. Guo, A. Kaskela, O. Reynaud, E. I. Kauppinen, S. Maruyama, Y. Matsuo, "Single-walled carbon nanotube film as electrode in indium-free planar heterojunction perovskite solar cells: investigation of electron-blocking layers and dopants". *Nano letters* **15**, 6665-6671 (2015).
- [17] Q. Luo, H. Ma, F. Hao, Q. Hou, J. Ren, L. Wu, Z. Yao, Y. Zhou, N. Wang, K. Jiang, "Carbon Nanotube Based Inverted Flexible Perovskite Solar Cells with All-Inorganic Charge Contacts". *Advanced Functional Materials* **27**, (2017).
- [18] Y. Jin, Y. Sun, K. Wang, Y. Chen, Z. Liang, Y. Xu, F. Xiao, "Long-term stable silver nanowire transparent composite as bottom electrode for perovskite solar cells". *Nano Research* **11**, 1998-2011 (2018).
- [19] E. Lee, J. Ahn, H. C. Kwon, S. Ma, K. Kim, S. Yun, J. Moon, "All-

- Solution-Processed Silver Nanowire Window Electrode-Based Flexible Perovskite Solar Cells Enabled with Amorphous Metal Oxide Protection". *Advanced Energy Materials* **8**, 1702182 (2018).
- [20] M. Kaltenbrunner, G. Adam, E. D. Głowacki, M. Drack, R. Schwödiauer, L. Leonat, D. H. Apaydin, H. Groiss, M. C. Scharber, M. S. White, "Flexible high power-per-weight perovskite solar cells with chromium oxide–metal contacts for improved stability in air". *Nature materials* **14**, 1032 (2015).
- [21] M. Park, H. J. Kim, I. Jeong, J. Lee, H. Lee, H. J. Son, D. E. Kim, M. J. Ko, "Mechanically recoverable and highly efficient perovskite solar cells: investigation of intrinsic flexibility of organic–inorganic perovskite". *Advanced Energy Materials* **5**, (2015).
- [22] J. Feng, X. Zhu, Z. Yang, X. Zhang, J. Niu, Z. Wang, S. Zuo, S. Priya, S. Liu, D. Yang, "Record Efficiency Stable Flexible Perovskite Solar Cell Using Effective Additive Assistant Strategy". *Advanced Materials* **30**, 1801418 (2018).
- [23] K. Chu, B. G. Song, H. I. Yang, D. M. Kim, C. S. Lee, M. Park, C. M. Chung, "Smart Passivation Materials with a Liquid Metal Microcapsule as Self-Healing Conductors for Sustainable and Flexible Perovskite Solar Cells". *Advanced Functional Materials*, 1800110 (2018).
- [24] K. Poorkazem, D. Liu, T. L. Kelly, "Fatigue resistance of a flexible, efficient, and metal oxide-free perovskite solar cell". *Journal of Materials Chemistry A* **3**, 9241-9248 (2015).
- [25] T. Yokota, P. Zalar, M. Kaltenbrunner, H. Jinno, N. Matsuhisa, H.

- Kitanosako, Y. Tachibana, W. Yukita, M. Koizumi, T. Someya, "Ultraflexible organic photonic skin". *Science advances* **2**, e1501856 (2016).
- [26] S. Kee, N. Kim, B. Park, B. S. Kim, S. Hong, J. H. Lee, S. Jeong, A. Kim, S. Y. Jang, K. Lee, "Highly Deformable and See-Through Polymer Light-Emitting Diodes with All-Conducting-Polymer Electrodes". *Advanced Materials* **30**, 1703437 (2018).
- [27] J.-I. Park, J. H. Heo, S.-H. Park, K. I. Hong, H. G. Jeong, S. H. Im, H.-K. Kim, "Highly flexible InSnO electrodes on thin colourless polyimide substrate for high-performance flexible CH₃NH₃PbI₃ perovskite solar cells". *Journal of Power Sources* **341**, 340-347 (2017).
- [28] N. Ahn, D.-Y. Son, I.-H. Jang, S. M. Kang, M. Choi, N.-G. Park, "Highly reproducible perovskite solar cells with average efficiency of 18.3% and best efficiency of 19.7% fabricated via Lewis base adduct of lead (II) iodide". *Journal of the American Chemical Society* **137**, 8696-8699 (2015).

Acknowledgement

This work was supported by the Global Frontier R&D Program on Center for Multiscale Energy System funded by the National Research Foundation under the Ministry of Science, ICT, and Future Planning, Korea.

The research data of Chapter 2 are the result on the collaboration with Taemin Lee and Yong Whan Choi. In addition, the research data of Chapter 2 have been published in Journal of Materials and Chemistry C (J. Mater. And Chem. C., 2017, 5, pp 10920-10925). The research data of Chapter 3 are the result on the collaboration with Taemin Lee, Yong Whan Choi. In addition, the research results of this chapter will be published in the academic journals. The research data of Chapter 4 are the result on the collaboration with Min-cheol Kim. In addition, the research results of this chapter will be published in the academic journals.

I would like to thank my supervisor Prof. Mansoo Choi, co-advisor Prof. Daeshik Kang and Prof. Sang Moon Kim for their warm encouragement and helpful advices. I am also grateful to Dr. Peter V. Pikhitsa and Dr. Sei Jin Park for their considerable guidance and encouragement. I would like to especially thank Namyong Ahn, Min-cheol Kim for their stimulating discussions and passionate contributions throughout this work. I also appreciate all of my laboratory members for their kind support, assistance and many helps.

이종 박막의 기계적 설계를 통한 유연 전자 소자 제작 연구

서울대학교 대학원 기계항공공학부

이 건 희

요약

지난 수년간 유연 전자장치는 광범위한 영역에서의 잠재적 사용 가능성으로 인해 활발히 연구가 이루어져 왔다. 유연 전자 장치는 기계적 변형이 쉽게 발생하는 상황에서도 그 기능을 유지해야 하기 때문에, 주로 변형에 내구성을 가지는 방향으로 연구가 집중되어왔다. 그러나, 변형을 극복해야하는 대상에서 나아가 이를 활용 한다면 새로운 기능을 구현하는 유연 전자 소자 개발이 가능하다. 본 학위 논문에서는 이종 구조층의 기계적 설계를 통해, 변형에 의해 다양하게 나타나는 유연 소자의 반응 특성을 이용하여 뛰어난 내구성을 가지는 유연 소자 개발과 더불어 새로운 기능을 구현하는 유연 전자 시스템을 제작하고 그 특성을 평가하였다.

먼저 탄성계수 크기 차이가 큰 서로 다른 두 접합된 층에 변형을 주었을 때, 생성되는 균열을 이용하여 센서 및 스위치 소자를 제작하였다. 균열을 이용한 센서는 주로 전도성 금속 박막과 고분자 탄성 폴리머 기판의 이중층으로 구성되며, 인장력에 따라 달라지는 미세한 균열의 변화를 전기 저항 신호로 측정함으로써 동작한다. 균열 기반 센서 시스템은 구성하고 있는 층의 물질에 따라 생성되는 균열의 모양과 깊이 등이 변화하며 그 감도와 특성 또한 변화하게 된다. 이에, PUA보다 탄성 계수가 더 낮은 실리콘 고무 기판의 도입을 통해 인장에 따라 형성되는 균열의 깊이 및 응답 특성을 변형 시킬 수 있었다. 실리콘 고무를 이용한 소자는 PUA를 사용한 소자보다 더 깊은 균열을 형성하였고 이를 이용해 인장에 의해 작동되는 스위치 소자를 제작할 수 있었다. 스위치 시스템에 활용되는 균열의 폭은 균열의 깊이도 인장 정도에 따라 함께 깊어지기 때문에 기존 균열기반센서가 보이고 있는 선형 관계 대신 초기하급수 관계를 보였다. 이러한 초기하급수적인 균열의 확대 양상은 약 2%의 변형률이 장치에 가해졌을 때 10^{12} 옴 이상의 무한한 금속 박막 저항을 나타낼 수 있게 하였다. 특별히, 1.6%의 변형률이 장치에 가해졌을 때, 그 저항이 10^5 배 증가하여 6×10^6 을 초과하는 민감도를 보였으며 이 장치가 센서와 더불어 스위치로 작동할 수 있음을 확인하였다. 전도성 금속

박막과 고분자 탄성 폴리머 기판의 이중층으로 이루어진 스위치를 신체에 부착 및 이들의 조합을 통해 손가락 움직임으로 동작하는 7 세그먼트 디스플레이와 AND, OR, NAND 및 NOR 게이트와 같은 논리 회로를 구현할 수 있었다.

다음으로, 늘어나는 정도 차이가 큰 서로 다른 두 층의 접합을 통해 잔류 응력을 형성하였고 이를 이용하여 말려지는 플랫폼 및 전자 소자를 제작하였다. 나비 대롱을 모사한 말려지는 플랫폼은 인장에 대해 잘 늘어나는 층과 잘 늘어나지 않는 층의 조합에 의해 형성되며, 필요에 따라 펴고 말리는 두 가지 동작이 모두 가능하다. 말려지는 플랫폼은 기존의 입는 형태의 전자 소자들과 달리 다양한 전자 소자들을 작은 부피에 집약할 수 있어 좁은 영역의 통과가 가능하며 혈관과 같이 얇고 둥글며 굴곡 있는 표면에 완전히 밀착하여 접촉을 가능하게 해준다. 본 연구에서는 구조 해석을 기반으로 말려지는 플랫폼에 히터, 인장 센서, 온도 센서 및 유기 발광 다이오드(OLED)와 같은 박막 전자 소자들을 제작하였으며, 모든 전자 소자들이 플랫폼이 말려있는 상태 및 펴져 있는 상태에서 파괴없이 잘 작동할 수 있게 구현하였다. 나아가 이를 이용하여, 작은 생명체를 잡고 작은 움직임을 측정하거나, 돼지 혈관에 부착하여 돼지 상태에 따른 맥파를 실시간으로 측정할 수 있을 뿐 아니라, 세포 시트를 쥐의 손상된

허벅지 근육에 성공적으로 전사하였다.

마지막으로, 소자를 구성하는 기판의 두께 변화를 통해 기판 위에 형성된 페로브스카이트 물질에 작용하는 응력을 조절하였고 이에 대한 물질의 내구성을 확인하였다. 페로브스카이트 태양전지는 기계적 유연성과 높은 효율로 인해 유연한 태양 전지로의 발전 가능성이 높은 소자이다. 그럼에도 불구하고, 실제로 휴대 가능한 전원 공급원으로 사용하기 위해서는 더 높은 유연성과 효율이 동시에 요구된다. 본 연구에서는 0.5 mm의 굽힘 반경에서 10,000회의 굽힘 및 말림과 구김과 같은 가혹한 변형 조건에도 그 성능을 유지하는 최고 17.03%의 효율을 가지는 매우 유연한 태양전지를 제작하였다. 이러한 뛰어난 성능은 매우 얇은 PET 기판에 고품질의 균열 없는 페로브스카이트 박막을 성공적으로 형성할 수 있었기 때문에 가능했다. 소자를 구성하는 기판의 두께는 전체 소자의 기계적 내구성에 가장 큰 영향을 주는 요소임을 굽힘 성능 시험을 통한 다결정 페로브스카이트 박막의 표면 변화를 통해 확인하였다. 그 결과 다결정 페로브스카이트 박막에 가해지는 인장과 균열 형성 사이의 관계를 확인할 수 있었고 다결정 페로브스카이트 박막의 파괴 지점을 확인하였다. 더불어, 금속 그물 구조와 전도성 고분자로 이루어진 투명전극을 사용함으로써 1.2 cm²의 면적에서도 최고 13.6%의 높은 효율과 유연성을 가지는 대면적

페로브스카이트 태양전지 또한 개발하였다.

주요어: 변형, 이중 박막의 설계, 균열, 말려지는 플랫폼, 유연 전자
소자, 유연 페로브스카이트 태양전지

학번: 2013-22494

List of Publications

- [1] K. Jung+, H.-J. Song+, **G. Lee**, Y. Ko, K. Ahn, H. Choi, J. Y. Kim, K. Ha, J. Song, J.-K. Lee, C. Lee, and M. Choi*, “Plasmonic organic solar cells employing nanobump assembly via aerosol-derived nanoparticles”, *ACS Nano*, (2014)
- [2] S. Jang+, J. S. Kang+, J.-K. Lee, S. M. Kim, Y. Son, A. Lim, H. Cho, J. Kim, J. Jeong, **G. Lee**, Y.-E. Sung and M. Choi* “Enhanced Light Harvesting in Mesoscopic Solar Cells by Multilevel Multiscale Photoelectrodes with Superpositioned Optical Properties”, *Advanced Functional Materials*, (2016)
- [3] S. M. Kim+, C. Ahn+, Y.-H. Cho, S. Kim, W. Hwang, S. Jang, S. S, **G. Lee**, Y.-E. Sung* and M. Choi*, “High-performance Fuel Cell with Stretched Catalyst-Coated Membrane: One-step Formation of Cracked Electrode”, *Scientific Reports*, (2016)
- [4] T. Lee+, Y. W. Choi+, **G. Lee**, P. V. Pikhitsa, D. Kang, S. M. Kim and M. Choi*, “Transparent ITO mechanical crack-based pressure and strain sensor”, *Journal of Materials Chemistry C*, (2016)
- [5] J. Yoon+, H. Sung+, **G. Lee**, W. Cho, N. Ahn, H. S. Jung* and M. Choi*, “Super Flexible, High-efficiency Perovskite Solar Cells Employing Graphene Electrodes: Toward Future Foldable Power Sources”, *Energy & Environmental Science*, (2017)

- [6] Y. W. Choi, D. Kang, P. V. Pikhitsa, T. Lee, S. M. Kim, **G. Lee**, D. Tahk and M. Choi*, “Ultra-sensitive Pressure sensor based on guided straight mechanical cracks”, *Scientific Reports*, (2017)
- [7] S. C. Hong+, **G. Lee**+, K. Ha+, J. Yoon, N. Ahn, W. Cho, M. Park and M. Choi*, “Precise morphology control and continuous fabrication of perovskite solar cells using droplet-controllable electrospray coating system”, *ACS Applied materials & Interfaces*, (2017)
- [8] T. Lee+, **G. Lee**+, Y. W. Choi+, P. V. Pikhitsa, S. M. Kim, D. Kang* and M. Choi*, “Crack-based strain sensor with diverse metal film by inserting inter-layer”, *RSC Advances*, (2017)
- [9] **G. Lee**+, Y. W. Choi+, T. Lee+, P. V. Pikhitsa, D. Kang, S. Park, S. M. Kim* and M. Choi*, “Metal–elastomer bilayered switches by utilizing the superexponential behavior of crack widening”, *Journal of Materials Chemistry C*, (2017) (**Back cover**)
- [10] T. Kim+, T. Lee+, **G. Lee**+, Y. W. Choi+, S. M. Kim*, D. Kang* and M. Choi*, “Polyimide Encapsulation of Spider-Inspired Crack-Based Sensors for Durability Improvement”, *Applied Science*, (2018)
- [11] H.-J. Song+, J. Han+, **G. Lee**, J. Sohn, Y. Kwon, M. Choi* and C. Lee*, “Enhanced light out-coupling in OLED employing thermal-assisted, self-aggregated silver nano particles”, *Organic Electronics*, (2018)
- [12] B. J. Kim+, M.-C. Kim+, D. G. Lee, **G. Lee**, G. J. Bang, M. Choi*, and H. S. Jung*, “Interface design of hybrid electron extraction layer for relieving hysteresis and retarding charge recombination in perovskite solar cells”, *Advanced Materials Interfaces*, (2018)